# DISCRETE OPTICAL SOLITONS

A Thesis Submitted to the Department of Electronics & Electrical Engineering for the Degree of Doctor of Philosophy.

*December, 1998.*


**UNIVERSITY**
***of***
**GLASGOW**



ProQuest LLC.
789 East Eisenhower Parkway
P.O. Box 1346
Ann Arbor, MI 48106 – 1346

# *Contents*

***Contents*** ..... ***i***

***Acknowledgements*** ..... ***iii***

***Abstract*** ..... ***iv***

***List of Publications*** ..... ***v***

***List of Tables and Figures*** ..... ***vii***

**1. *Introduction*** ..... **1**

1.1 Optical Communication Systems ..... 1

1.2 Theoretical Background on Non-linear Optics ..... 4

1.3 Third Order Non-resonant Non-linear Optical Processes ..... 6

*1.3.1 Two-photon Absorption* ..... 6

*1.3.2 Three-photon Absorption* ..... 7

*1.3.3 Self and Cross- Phase Modulation* ..... 7

*1.3.4 Self-Focusing* ..... 8

*1.3.5 Four-Wave Mixing* ..... 8

1.4 The Family of Solitons ..... 9

*1.4.1 Spatial Solitons* ..... 9

*1.4.2 Temporal Solitons* ..... 11

*1.4.2 Vectorial Solitons* ..... 11

*1.4.3 Light Bullets* ..... 11

*1.4.4 Discrete Solitons* ..... 12

1.5 The Material of Choice: AlGaAs at the Half Band Gap ..... 12

1.6 Waveguide Structures for Non-linear Optics Experiments ..... 14

1.7 Numerical Methods for Waveguide Design ..... 20

*1.7.1 Two-dimensional Waveguide Analysis: The Effective Index Approximation* ..... 20

*1.7.2 BPM_CAD* ..... 21

*1.7.3 F-Wave* ..... 24

1.8 Fabrication of Waveguides and Waveguide Arrays ..... 25
1.9 The Laser Source: Beamlock-Tsunami-Opal System by Spectra Physics .... 27
1.10 Description of the Experimental Set-up ..... 29
1.11 Summary of Chapter 1 ..... 30

2. ***Solitons in Arrays of Waveguides*** ..... **31**
2.1 Non-linear Multi-Core Directional Couplers in AlGaAs ..... 33
2.2 Implications for All Optical Switching ..... 36
2.3 Design and Fabrication of the Waveguide Arrays ..... 38
2.4 Initial Sample Fabrication ..... 41
*2.4.1 Theoretical Modelling* ..... 42
*2.4.2 Experimental Results* ..... 42
2.5 Second Set of Samples : Observation of Discrete Spatial Solitons ..... 45
2.6 Dynamics of Discrete Solitons in Optical Waveguide Arrays ..... 50
2.7 Non-linearly Induced Escape from Defect States in Waveguide Arrays..... 56
2.8 Conclusions ..... 62

***3. Intermixing as a way of Tailoring the Non-linear Optical Coefficients*** **64**
3.1 Comparison between Bulk AlGaAs and MQW Heterostructure ..... 65
3.2 Design of the MQW Waveguide Structure ..... 67
3.3 Fabrication of the Waveguides ..... 69
3.4 Experimental Results ..... 73
*3.4.1 Determination of the TPA Coefficient* ..... 74
*3.4.2 Three-photon Absorption* ..... 79
*3.4.3 Non-linear Refractive Index and Ratio XPM/SPM* ..... 84
3.5 Conclusions ..... 88

***4. Summary*** ..... **90**
***5. References*** ..... **91**

# *Acknowledgments*

This work could not be possible without the help and support of numerous people.

I would like to express my deepest appreciation to my supervisor, Dr. Stewart Aitchison, for giving me the opportunity to conduct this research, and, most of all, for teaching me how to enjoy it (well, most of the time). I am also indebted to Ulf Peschel, a great friend and scientist, for reminding me that behind every natural phenomenon there is - fortunately ? - an equation, and to Hagai Eisenberg and Prof. Yaron Silberberg of Weizmann Institute of Science (Rehovot) for the exciting and productive time we spent together. I would like to thank the Head of Department, Prof. S. Beaumont, the staff and the colleagues in the Optoelectronic Group of the University of Glasgow for giving me access to some of the best facilities in the world and for the advice I received when I needed more. In particular, I would like to express my gratitude to P. Cusumano, D. Hutchings, C. Hamilton, P. Millar, C. Smith, M. Street, D. Ortega, S. Mc Dougall, A. Boyd, A. Saher, T. Perscht (from the University of Jena) and Y. Barad (from the Weizmann Institute of Science) for the help I received at different stages of this work.

My deepest appreciation goes to the technical staff of both the University of Glasgow and of the Weizmann Institute of Science for making the impossible possible and for performing a couple of miracles. T. Hanson, H. Hunter and A. White also deserve a special "thank you" for the wonderful year I spent at NE technology LTD, Edinburgh, before moving to Glasgow.

I am especially indebted to my friends, Arno, David, Daniele, Dwir, Domenico, Elena, Federico, Francesco, Hanna, Giovanni, Hagai, Yaniv, Ingolf, Marc, Paolo, Pasquale, Patty, Shimshon, Stefano, Tami, and Zoltan, to make my time in Glasgow and Rehovot worth a story to tell to my grandchildren.

Last, but certainly not least, I would like to thank my father, Adelio, my mother, Elena, my brother and sister, Alessandro and Michela for their understanding, support and sacrifice. Encouragement and support from Susan, who has brought so much joy into my life, is deeply appreciated.

# *Abstract*

Discreteness is a basic property of nature itself. For example energy transport through polarons, excitons or defects depends critically on the internal molecular structure. Also complex macroscopic systems as waveguide arrays or discrete electrical lattices can be understood by an effective discretisation. This allows for the identification of basic principles and effects of discreteness, which are much more general than the model from which they are derived.
One of the most interesting features of all these systems is the existence of robust solitary states, or discrete solitons: in this thesis we report the first experimental observation of discrete spatial optical solitons in arrays of waveguides. Light was coupled in the central waveguide. At low power, the propagating light widened its distribution as it coupled to more distant waveguides. When sufficient power was injected, light was localised close to the input waveguides and its distribution was successfully described by the discrete non-linear Schrödinger equation.

By using a non-linear waveguide array we also demonstrate the distinct dynamical properties of discrete solitons, which are not found in the corresponding continuous systems. We observed non-linearly induced locking of initially moving solitons as well as the acceleration of resting solitons. These abrupt changes of the propagation angle with respect to the waveguide direction are a result of the lack of momentum conservation in discrete systems.

Our work on optical arrays was concluded by the experimental investigation of the linear and non-linear optical response of a non-uniform waveguide array. By reducing the width of a single waveguide we decreased its effective index and induce waveguiding along the defect. Due to the positive non-linearity the index difference was reduced for increasing power levels with the result that the field escaped.

Finally, with the aim of fabricating regions with different non-linearities in a same chip, we performed a comparison between the relevant non-resonant non-linear optical properties of an AlGaAs multiple quantum well heterostructure before and after intermixing. In particular, we experimentally investigated the wavelength dependence of the non-linear refractive index, two- and three-photon absorption and the ratio between self-phase modulation and cross phase modulation.

# *List of Publications*

## Journal Publications

**H. S. Eisenberg, Y. Silberberg, R. Morandotti, A. R. Boyd and J. S. Aitchison,** "Discrete spatial optical solitons in waveguide arrays", Phys. Rev. Lett., **81**, 3383 (1998)

**R. Morandotti, H. Eisenberg, U.Peschel, Y. Silberberg and J. S. Aitchison,** "Dynamics of discrete optical solitons", submitted to Phys. Rev. Lett.

**U. Peschel, R. Morandotti , J. S. Aitchison, H. S. Eisenberg, Y. Silberberg,** "Non-linearly induced escape from defect states in waveguide arrays", submitted to Applied Physics Letters

## Conference Publications

**R. Morandotti, J. S. Aitchison, H. Einsenberg, Y. Barad and Y. Silberberg,** "Variation of Third Order Non-linearities in Multiple Quantum Well Heterostructures with Bandgap tuning using Intermixing", *in CLEO* **Vol. 6,** OSA Technical Digest Series, p.202 (1998)

**J. S. Aitchison, R. Morandotti, H. Einsenberg, Y. Barad and Y. Silberberg,** "Non-linear Waveguide Arrays and Discrete Spatial Solitons", *Invited Paper in IQEC,* **Vol. 7,** OSA Technical Digest Series, p.19 (1998)

**J. S. Aitchison, R. Morandotti, H. Einsenberg, Y. Barad and Y. Silberberg,** "Self-localisation in Nonlinear Waveguide Arrays", *Invited Paper for Novel Solitons and Non-linear Periodic Structure Workshop, NLGW*, **Victoria BC, Canada (1998)**

**R. Morandotti, J. S. Aitchison, H. Einsenberg and Y. Silberberg,** "Non-linear Switching in Non-Uniform Waveguide Arrays", *CLEO Europe*, **Glasgow, UK (1998)**

**H. Einsenberg, Y. Silberberg, R. Morandotti and J. S. Aitchison,** "Observation of Discrete Spatial Solitons", Invited Paper *IQEC Europe*, **Glasgow, UK (1998)**

**R. Morandotti, U. Peschel, J. S. Aitchison, H. Eisenberg and Y. Silberberg,** "Dynamics of Discrete Solitons in Optical Waveguide Arrays", submitted to IQEC, **Baltimore, USA (1999)**

**R. Morandotti, U. Peschel, J. S. Aitchison, H. Eisenberg and Y. Silberberg,** "Dynamical Properties of Discrete Solitons in Optical Waveguide Arrays", IEE Meeting on Optical Solitons, **London, UK (1999)**

**U. Peschel, R. Morandotti, J. S. Aitchison, H. Eisenberg and Y. Silberberg,** "Strongly non-linear effects in non-uniform waveguide arrays", IEE Meeting on Optical Solitons, **London, UK (1999)**

# *Index of Tables and Figures*


***Tab. 2.1*** Theoretical and experimental switching power levels ..... 44

***Tab. 3.1*** The different linear and non-linear loss regimes ..... 82

***Fig. 1.1*** Schematic of a fibre communication system ..... 2

***Fig. 1.2*** Band diagram of an indirect (left) and a direct (right) band gap semiconductor ..... 13

***Fig. 1.3*** Studing the propagation of light using a ray-tracing model..... 15

***Fig. 1.4*** Only certain modes can propagate in a waveguide structure ..... 16

***Fig. 1.5*** Lay-out of a strip loaded waveguide ..... 20

***Fig. 1.6*** Effective index method ..... 21

***Fig. 1.7*** Comparison between a 2D (top) and a 3D (bottom) BPM. The simulated structure (middle) is a non-uniform array. Only the central waveguide, 2.5 μm wide, was excited. The surrounding waveguides are 4μm wide ..... 23

***Fig. 1.8*** Dry-etching using S1805 resist as a mask. For etch depth around 1μm, the resist layer is not thick enough and the waveguide is damaged (right). The problem, not present when using a thicker mask (S1818) can be solved by post-baking the sample for 30 minutes at 120 C° (left) ..... 27

***Fig. 1.9*** Typical set-up for non-linear optics experiments ..... 30

***Fig. 2.1*** The Two Core Coupler. The schematic (BOTTOM) and the evolution of the intensity along the waveguide (TOP) ..... 33

***Fig. 2.2*** a) Discrete diffraction in a non-linear waveguide array and b) formation of a discrete soliton. These simulations assume a peak power equal to 0.05 and 1 KW, respectively ..... 35

*Fig. 2.3* TOP: a) Lack of interaction for 2 co-propagating discrete solitons in a weakly coupled array (a) as opposed to the significant mutual interactions in a strongly coupled array. The solitons are out of phase and in phase ( b) and c), respectively). BOTTOM: a trapped soliton in a weakly coupled array (d) and a moving soliton in a strongly coupled array (e) ..... 37

*Fig. 2.4* Schematic representation of the section of a Two Core Coupler ... 38

*Fig. 2.5* Schematic view of a N-core coupled array ..... 39

*Fig. 2.6* Typical AlGaAs waveguide structure ..... 40

*Fig. 2.7* Optical microscope view of a 1x9 coupler mask ..... 41

*Fig. 2.8* Power dependent switching characteristic for a strongly (left) and a weakly (right) coupled array, for low (dotted line) and high (solid line) power. The input polarisation was TE ..... 43

*Fig. 2.9* The simulations undertaken using coupled mode theory show an excellent agreement with the experimental data (see Fig. 2.8) ..... 43

*Fig. 2.10* Micrograph image of a waveguide array ..... 45

*Fig. 2.11* Generation of a discrete spatial soliton in a 41 waveguide array. At low power (TOP), discrete diffraction is present. When the energy is increased, the beam starts to narrow (MIDDLE) and finally a discrete soliton is formed (BOTTOM) ..... 46

*Fig. 2.12* Excellent agreement between experimental and theoretical data (represented by the straight lines) at low and high power (top and bottom of the graph, respectively). The samples were 3.0 (left) and 1.9 coupling lengths (right) long ..... 47

*Fig. 2.13* Can we excite 3 or 5 waveguides at the input of the array (the pictures below are SEM micrographs)? ..... 49

*Fig. 2.14* Non-linear localisation in an array excited by a 3 star junction. The separation between each waveguide was 5 μm and the polarisation was TE ..... 50

*Fig. 2.15* **Peierls-Nabarro-Potential**: Hamiltonian versus guided power for solitons centred on and in between two waveguides, inset: field

shapes of the two types of solitons for a power of 1500 W, dashed line: maximum incoupled peak power available in the experiment . 51

***Fig. 2.16*** Differences between a discrete and a continuum system. In the first, a small phase tilt can be corrected by a suitable non-linearity (trapping of a moving soliton, A). This is not allowed for a soliton in a slab waveguide (B). In a discrete system is also possible to achieve a large steering by injecting a beam in between two waveguides, which will acquire an excess of kinetic energy due to the difference in the Hamiltonians between a stable and an unstable soliton (C). This behaviour is also not allowed in a slab waveguide ..... 52

***Fig. 2.17*** *Left*: Power dependent soliton steering by an externally induced velocity. Output field distribution as a function of applied power (initial tilt of the beam: ca 0.4 degree, experimental result -top-, and simulation -bottom-)
*Right:* Soliton steering by internally induced velocity: Output field distribution as a function of the input beam position, experimental result (top) and simulation (bottom). The solid line represents a beam centred on a waveguide, while the dashed line shows a beam centred between two waveguides ..... 54

***Fig. 2.18*** Micrograph of a non-uniform waveguide array ..... 57

***Fig. 2.19*** Experimental results - field profiles at the output facet for TE polarisation for an array with a defect at guide 0, a) low power, b) high power (1000W incoupled power) ..... 59

***Fig. 2.20*** Numerical simulations, a) amplitude distribution of the guided mode, b) low power field distribution at the output facet of an array without a defect, c) low (thin line) and high power (1000 W, bold line) field profiles for an array with a defect at guide 0 ..... 61

***Fig. 3.1*** MQW Intermixing as a way to fabricate regions with different non-linearities. In principle, intermixing suppress the non-linear effects, and no switching is observed in the input Three Core

Coupler (part a) of the figure). In a normal wafer (part b)) switching occurs at the input for high energy, hence is not possible to excite 3 waveguides contemporaneously. ..... 64

***Fig. 3.2*** Schematic diagram of an intermixing process using IFVD techniques ..... 66

***Fig. 3.3*** Effect of variations in the width of the well on the fundamental band edge for a MQW heterostructure. Numerical simulation for the case of one monolayer (continuous line) and two monolayers (dotted line) are reported ..... 68

***Fig. 3.4*** SEM picture of an AlGaAs/AlGaAs MQW waveguide. Selective etching reveals a degree of non-uniformity in the layer compositions ..... 68

***Fig. 3.5*** Morphology for two sample intermixed at 925 C° (left) and at 960 C° (right). We observe how, in the latter case, the quality is strongly deteriorated due to the many defects present over the surface ..... 69

***Fig. 3.6*** Photoluminescence transitions of intermixed samples, for 3 different annealing temperatures, are compared. We have, from right to left, the following spectra: as grown, intermixed at 925°C, intermixed at 940 °C and intermixed at 960 °C ..... 70

***Fig. 3.7*** Transmission spectrum as recorded in a MQW sample ..... 71

***Fig. 3.8*** The MQW waveguide structure ..... 73

***Fig. 3.9*** Typical anisotropy of $n_2$ and TPA coefficients of GaAs: for linear and circular polarised light. The origin of the polarisation vector is at the centre of the figure. The axes correspond to the crystallographic-axis directions ..... 74

***Fig. 3.10*** Typical plot of the inverse transmission as a function of the input intensity..... 75

***Fig. 3.11*** Effect of Two photon absorption, dispersion and self phase modulation on the transmission of a pulse with a sech-like shape

in AlGaAs at the half band gap. Typical values of the inverse transmission as a function of the input power are shown in a CW regime (empty squares), and for pulses 200 fs and 100 fs long (solid and empty circles, respectively) ..... 76

*Fig. 3.12* The spectra of two-photon-absorption coefficients of GaAs, demonstrating both anisotropy and linear-circular dichroism ..... 77

*Fig 3.13* Experimental values for $\alpha_2$ as a function of wavelength in a disordered sample: TE, solid square. TM, empty circle. Scalar model, continuos line. ..... 78

*Fig. 3.14* Plot of the inverse transmission squared as a function of the input intensity squared ..... 80

*Fig. 3.15* Effect of Three photon absorption, dispersion and self phase modulation on the transmission of a pulse with a sech-like shape in AlGaAs at the half band gap. Typical values of the inverse transmission as a function of the input power are shown in a CW regime (empty squares), and for pulses 100 fs and 200 fs long (solid and empty circles, respectively) ..... 81

*Fig. 3.16* Experimental values for $\alpha_3$ as a function of wavelength. The data (disordered, TE, solid circle; disordered, TM, solid square; undisordered, TE, empty circle, undisordered, TM, empty square) are compared with the calculated dispersion of $\alpha_3$. The model predicts a scarce influence of intermixing on the value of 3PA, represented by a continuum line. ..... 83

*Fig. 3.17* The measured dispersion of $n_2$. Disordered, TE, black empty squares. Disordered, TM, black solid circles. Undisordered, TE, red empty squares. Undisordered, TM, red solid circles ..... 84

*Fig. 3.18* a) SPM (continuum line) and XPM (dotted line) for a TM pump polarisation. b) SPM (continuum line) and XPM (dotted line) for a TE pump polarisation ..... 86

***Fig. 3.19*** The experimental dispersion of the ratio *XPM (TE pump)/ SPM (TE)* (black solid circles) and of the ratio *XPM (TM pump)/ SPM (TM)* (black empty squares) are shown for a disordered sample. We performed the same measures at 1.53 μm and at 1.58 μm in a sample "as grown" (red solid circles and red empty squares, respectively)..... 87

# Chapter 1

# *Introduction*

## 1.1 Optical Communication Systems

A massive effort has recently been directed towards increasing the potential of communication systems, or, in simpler terms, the ability to transfer information from one point to another. Generally, this is achieved by superimposing or modulating the information on to an electromagnetic wave, which will act as a carrier for the information. The carrier can either be in the radio, or optical frequency range. As the information carrying capacity is related to the bandwidth, or frequency extent, of the modulated carrier, optical waves offer an increase in the potential usable bandwidth by a factor of around $10^4$ over high frequencies microwave transmission.

A real interest in optical communication arose only in the early 1960s with the invention of the laser. Now this device provides a powerful, coherent light source together with the possibility of modulation at high frequencies. Unfortunately light transmission in the atmosphere is restricted to line of sight and is severely affected by disturbances such as rain, snow, fog, dust and atmospheric turbulence. This limitation was overcome in 1966 by the proposal of optical communication via dielectric waveguides, or optical fibres fabricated from glass[1,2]. In the space of only ten years, very low loss fibres were produced and suitable low loss fibre splicing techniques perfected. In parallel with the development of the optical fibre, a great deal of interest was also focused on the other optical components which would

[1] K. C. Kao and G. A. Hockham, Proc. IEE, **113,** 1151 (1966)

[2] A. Werts, L' Onde Electrique, **46**, 967 (1966)

constitute an optical communication system. A particular effort was devoted to the fabrication of semiconductor optical sources (i.e. injection lasers and light emitting diodes) and detectors (i.e. photo-diodes) compatible in sizes with optical fibres.

Developments in fibre technology have continued rapidly over recent years, with the major achievement of low losses and low chromatic dispersion at the same operating wavelength, increasing the maximum bandwidth achievable with conventional single-mode fibres. High performance, reliable optical fibre communication systems are now widely deployed both within telecommunication networks and many other more localised communication application areas.

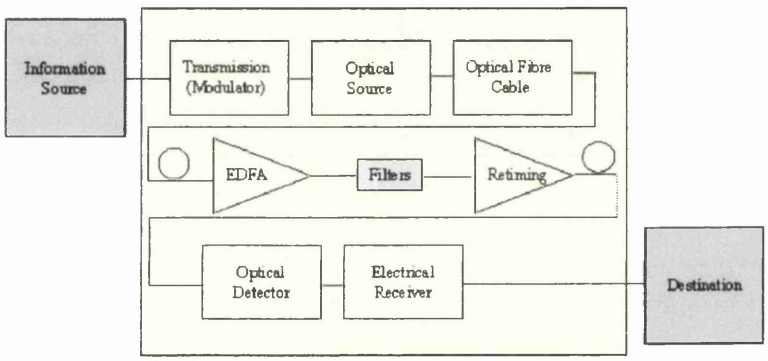


***Fig. 1.1*** Schematic of a fibre communication system

An optical fibre system is similar to any other type of communication system. As shown by the block schematic in Fig. 1.1, it consists of a transmitter, or modulator linked to the information source, the transmission medium, and a receiver, or demodulator at the receiving point. In an optical communication system the information source provides an electrical signal to a transmitter comprising an electrical stage which drives an optical source to modulate the light-wave carrier. The optical source which provides the electrical-optical conversion is generally a semiconductor laser. The transmission medium consists of an optical fibre cable

and the receiver consists of an optical detector, e.g. a photo-diode, which drives a further electrical stage and hence, provides demodulation of the optical carrier.

Communication using an optical carrier wave guided along a glass fibre has a number of extremely attractive features, for example: enormous potential bandwidth, low transmission loss, system reliability and ease of maintenance and, finally, potential low cost. However, a number of disadvantages are always present at the introduction of a new technology, and optical fibre systems are not an exception. The main drawback is that electronic repeaters are necessary to regenerate periodically the original pulse and require an independent electrical power feed.

At present the repeaters are spaced by approximately 20-80 km, which implies a severe reduction in data transfer speed together with a significant increase in the cost of a fibre communication system. To overcome these two problems, it would be desirable to transmit data over long haul distances, with data routing and processing occurring in an all-optical format.

One way to solve the first issue is to use soliton based optical systems. Temporal solitons[3] can be employed to transmit distortion free, highly packed data over long distances, with the further advantage that they can be amplified optically. However, in order to achieve ultra-fast data routing and processing, switching should occur all optically. Spatial optical solitons have been proposed as the information bit in the next generation of communication systems, mainly because they have particle-like features which make reciprocal interactions possible[4,5]. Although it is true that soliton transmission in optical communication systems has been recently carried out[6], many problems still have to be addressed before a large scale adoption is

[3] L. F. Mollenauer, B. M. Nyman, M. J. Neubelt , G. Raybon , S. G. Evangelides, Elec. Lett., **27**, 178 (1991)

[4] A. U. Snyder and A. P. Sheppard, Optics Letters, **18**, 482 (1993)

[5] A. B. Aceves, C. De Angelis, S. Trillo, S. Wabnitz, **19**, 332 (1994)

[6] See, for example, J. M. Jacob, E. A. Golovchenko, A. N. Pilipetskii, G. M. Carter, C. R. Menyuk, IEEE Photonics Technology Letters, **9**, 130 (1997)

possible. These problems are mainly due to timing uncertainties associated with the Gordon-Haus effect and self-frequency shifting[7]. A way around these unexpected limitations came in the form of all-optical clock recovery and sliding-frequency filters[8].

## 1.2 Theoretical Background on Non-linear Optics

Whenever we want to analyse a soliton based optical system, we need to introduce the concept of non-linear optics. With this term, we generally describe those phenomena for which the electric field intensity is high enough to generate a non-linear response in the induced polarisation.

In the presence of strong intensity fields ($10^6$ V/m to $10^{12}$ V/m), and for an instantaneous response, the expression for the induced polarisation in a dielectric medium is no longer the simple linear relation we are familiar with but takes a general form given by:

$$P_i = \varepsilon_0\left[\chi^{(1)}_{ij}E_j + \chi^{(2)}_{ijk}E_jE_k + \chi^{(3)}_{ijkl}E_jE_kE_l + \ldots\right] \qquad 1.1$$

where $E_j$ is the electric field, $\varepsilon_0$ =8.85 $10^{-12}$ F/m is the permittivity in vacuum and $\chi^{(i)}$ is the $i^{th}$ order susceptibility[9]. A sum is performed over the repeated indices. The second term of the polarisation ($\chi^{(2)}_{ijk}E_jE$) represents a second order non-linearity, and gives rise to such effects as second harmonic generation, optical rectification and optical parametric oscillation. This term involves two optical

[7] J. P. Gordon, in XV International Conference on Quantum Electronics, Digest of Technical Papers, 98 (1987)

[8] Y. Kodama and S. Wabnitz, Optics Letters, **18**, 1311 (1993)

[9] P. N. Butcher and D. Cotter, *" The Elements of Nonlinear Optics and Electronic Properties of Semiconductors "*, Cambridge Studies In Modern Optics, Cambridge, UK (1990)

frequencies and requires phase-matching[9,10]. It will not be considered further in this work. The third term is non-zero in all materials and is responsible for a class of effects, which include Self-Phase Modulation and Self-Focusing. These phenomena are responsible, together with dispersion (and diffraction, respectively) for the generation of temporal (and spatial) solitons.

In order to understand the mechanism of action of third-order non-linearities we ignore $\chi^{(2)}$ and all terms above $\chi^{(3)}$. In this case, the real part of $\chi^{(3)}$accounts for an intensity dependent index change as:

$$n = n_0 + n_2 I . \qquad 1.2$$

Here $n_0$ is the linear refractive index, $I$ is the light intensity and $n_2$ is the non-linear refractive index, which is defined, in terms of its tensor components, as:

$$n_{2_{ijkl}} = \frac{3}{4}\frac{\mathrm{Re}\,\chi^{(3)}_{ijkl}}{n_0^2 \varepsilon_0 c} . \qquad 1.3$$

Where $\chi^{(3)}_{diag} = \chi^{(3)}_{xxxx} = \chi^{(3)}_{yyyy} = \chi^{(3)}_{zzzz}$ for an *isotropic* material. This non-linear refractive index is termed the optical Kerr coefficient and is around $1.5\text{x}10^{-13}$ $\text{cm}^2\text{W}^{-1}$ in AlGaAs at the half band gap[11]. This coefficient is the refractive term, its imaginary part gives rise to an absorption, which is defined as:

$$\alpha = \alpha_0 + \alpha_2 I , \qquad 1.4$$

where

[10] R. K. Chang and N. Bloembergen, Phys. Rev., **144**, 775 (1962)

[11] J. S Aitchison, D. C. Hutchings, J. U. Kang, G. I. Stegeman and A. Villeneuve, IEEE J. Quant.Electron., **33**, 341 (1997)

$$\alpha_{2_{ijkl}} = \frac{3}{2}\frac{\omega \mathrm{Im}\chi^{(3)}_{ijkl}}{n_0^2 \varepsilon_0 c^2}. \qquad 1.5$$

In this equation, $\alpha_0$ is the linear absorption, $\alpha_2$ is the non-linear absorption coefficient and again $I$ is the local intensity[12]. Non-resonant non-linearities are dominant at photon energies far from the band gap absorption edge (e. g. at the half band gap), which means that the change in the optical properties of the material is caused directly by the optical field. If we excite AlGaAs with a wavelength close to the fundamental band gap, a more significant absorption of light will occur, resulting in the establishment of real excited population, which through the Kramers-Kronig relation leads to a change in the refractive index of the material[13]. Such effects produce large optical non-linearities but have a slow temporal response governed by the relaxation time of the electrons from the excited states (typically of the order of a few nanoseconds). While devices based on resonantly enhanced non-linearities are very much wavelength sensitive and can suffer from saturation effects, non-resonant processes are almost instantaneous and wavelength insensitive. Therefore, they are optimal for ultra-fast switching applications.

## 1.3 Third-order Non-resonant Non-linear Optical Processes

In this section some of the third-order **non-resonant** non-linear optical processes dealt with during this work will be briefly described[14].

*1.3.1* **Two-photon Absorption.** Two-photon absorption (TPA or 2PA) is a process in which an electron in the valence band makes a transition to the conduction band by absorbing two photons simultaneously. Because the probability of this

[12] D. C. Hutchings and B. S. Wherrett, Optical Materials, **3**, 53 (1994)

[13] M. Sheik Bahae, D. C. Hutchings, D. J. Hagan, E. W Van Stryland, IEEE J. Quant. Electron., **27**, 1296 (1991)

[14] For a detailed discussion see G. P. Agrawal "*Nonlinear Fiber Optics*" , Academic Press, New York, USA (1995)

process occurring is very small compared to that of single photon processes, it can be observed only in the high intensity case[11]. Electrons do not have sufficient energy to make a transition to the conduction band by absorbing two photons with energies below half the band gap. However, because of defects in a real material, the two-photon equivalent of band tailing called the Urbach tail occurs[15,16] and two-photon absorption can also be present below half the band gap.

*1.3.2* **Three-photon Absorption**. Three-photon Absorption (3PA) is a fifth-order process, where electrons are promoted to the conduction band by absorbing three photons simultaneously. Very high intensities are required for this process to occur, but most all-optical waveguide switching devices shorter than 1 cm require switching intensities over 1 GW/cm$^2$. The resulting losses can pose a significant problem for all-optical switching devices below half band, becoming prohibitive near one-third of the band gap.[17]

*1.3.3* **Self- and Cross- Phase Modulation**: Self-Phase Modulation (SPM) is the term used to describe the power dependent spectral broadening of an optical pulse propagating in a non-linear material. The non-linear refractive index of a material can be calculated by measuring the Self-Phase Modulation induced broadening of a pulse.

The non-linear phase change $\Delta\Phi$ is related to $n_2$ by the equation:

$$\Delta\Phi = \frac{2\pi}{\lambda} L_{eff} n_2 I, \qquad 1.6$$

[15] F. Urbach, Phys. Rev., **92**, 1324 (1953) and:

[16] H. Haug and S. W. Koch, *"Quantum Theory of the Optical and Electronic Properties of Semiconductors"*, World Scientific, Singapore (1990)

[17] J. U. Kang, A. Villeneuve, M. Sheik Bahae, G. I Stegeman, K. Al hemyari, J. S.Aitchison, C. N Ironside, Appl. Phys. Lett., **65**, 147 (1994)

where $L_{eff} = \frac{1-\exp(-\alpha_0 z)}{\alpha_0}$ is the effective interaction length (accounting for the linear losses, $\alpha_0$),[18] $I$ is the intensity of the light pulse and $\lambda$ is the wavelength of the light in vacuum. It can be seen from Eq. 1.6 that the non-linear refraction coefficient $n_2$ can be estimated from the phase modulation experienced by a high peak power pulse after propagation through the non-linear medium. Physically similar to SPM, Cross-Phase Modulation (XPM) indicates the spectral broadening induced by a strong optical pulse (pump) on a weak co-propagating wave of opposite polarisation (probe). The relative value of Cross-Phase Modulation (XPM) to Self-Phase Modulation (SPM) plays a very important role in many applications of non-linear optics, such as polarisation switching, de-multiplexing and soliton steering, and also in the generation of novel solitonic effects[19].

*1.3.4* **Self-Focusing**: occurs in a high intensity beam where the intensity of light falls gradually away from the center to the edges. Hence, if this distribution propagates through a third-order non-linear material with a positive $n_2$, the local refractive index of the material will be greater where the intensity is higher. In this case, the non-linear medium acts as a positive lens and a light pulse will tend to focus as it propagates through the material. Damage to the non-linear medium can occur provided that the intensity of the light pulse is high enough and the medium is long enough for the light to reach a focal point within the material.

*1.3.5* **Four-Wave Mixing**. Three optical waves oscillating at frequencies $\omega_1$, $\omega_2$, and $\omega_3$ and linearly polarized along the same axis, combine non-linearly and give rise

[18] C. J. Hamilton, *"Novel Structure and fabrication Techniques for the Observation of Solitons in AlGaAs"*, Ph.D. Thesis, University of Glasgow, Glasgow, UK (1995)

[19] J. U. Kang, G. I. Stegeman, J. S. Aitchison and N. N. Akhmediev, Phys. Rev. Lett., **76**, 3699 (1996)

to a new frequency $\omega_4$ when substituted in the third-order polarization term of equation 1.1

$$P_i = \varepsilon_0 \chi^{(3)}_{ijkl} E_j E_k E_l . \qquad 1.7$$

The new frequency is a sum of the initial values $\pm\omega_1, \pm\omega_2$ and $\pm\omega_3$. Significant four-wave mixing requires matching of the frequencies as well as of the wave vectors (Phase Matching), in a similar manner to Second Harmonic Generation. Whilst four-wave mixing can be sometimes an undesirable effect in performing non-linear measurements[20], it can also lead to useful application such as signal gain[21] and polarisation switching in AlGaAs waveguides.

## 1.4 The Family of Solitons

After having briefly overviewed the most significant phenomena related to the third-order non-linearities, we shall say that soliton is the general term used to describe a localised intensity distribution, in time or space, which stays unperturbed, as it propagates. However, such stable propagation is not just enough to qualify a pulse as a soliton. A peculiar property of solitons is their particle-like behavior. Solitons also interact with other solitons while still retaining their identities. In this paragraph the main types of optical solitons, relevant to this research, will be described.

*1.4.1* **Spatial Solitons.** Spatial Solitons are self-guided, or self-trapped beams that propagate without changing their spatial distribution. They are stable when diffraction is limited to one spatial dimension and, for example, they have been

[20] A. Villeneuve, J. U. Kang, J. S. Aitchison and G. I. Stageman, Appl. Phys. Lett., **67**, 760 (1995)

[21] J. S. Aitchison, J. U. Kang, G. I. Stageman, App. Phys. Lett., **67**, 2456 (1995)

observed in AlGaAs semiconductor slab waveguides[22]. The propagation of a spatial soliton is described by the non-linear Schrödinger equation of the form:

$$\frac{\partial E}{\partial z} = \frac{i}{2k}\frac{d^2E}{dx^2} + ik_0 n_2 |E|^2 E . \qquad 1.8$$

In the expression above, $E$ is the normalised electric field strength whilst $k_0$ and $k$ are the wave vectors in free space and in the material respectively. The first term on the right hand side of the equation describes the diffraction of the light in the transversal direction. The second term is related to the self-focusing effects of the non-linear material when the non-linear refractive coefficient is positive, otherwise to self-defocusing of the pulse.

Bright spatial solitons can only be generated in material with a positive non-linearity where the effects of diffraction are balanced by self-focusing. The fundamental bright soliton envelope can be described by the following expression:

$$E(x,z) = E_0 \,\mathrm{sech}\left(\frac{x}{a_0}\right)\exp\left(\frac{iz}{2ka_0^2}\right) \qquad 1.9$$

where $a_0$ is a measure of beam width and $E_0$ is defined as:

$$E_0 = \frac{1}{ka_0}\sqrt{\frac{n_0}{n_2}} \qquad 1.10$$

This will lead to a total power associated to the beam equal to:[23]

[22] J. S. Aitchison, K. Al-Hemyari, C. N. Ironside, R. S. Grant, and W. Sibbett, Electron. Lett., **28**, 1879 (1990)

[23] J. S. Aitchison, A. M. Weiner, Y. Silberberg, D. E. Leaird, M. K. Oliver, J. L. Jackel, D. E. Leaird, M. K. Oliver, E. M. Vogel and P. W. E. Smith, Opt. Lett., **15**, 471 (1990)

$$P_t = \frac{2n_0 w}{n_2 a_0 k^2} \qquad 1.11$$

where $w$ is the transverse mode size. Higher order solutions exist at intensity levels of $N^2 P_t$ where $N$ is an integer.

*1.4.2* **Temporal Solitons.** Mathematically similar to spatial solitons, temporal solitons are pulses of light which do not disperse as they propagate. They occur in non-linear media as a result of the balancing effect between anomalous group velocity dispersion, (in which the group velocity increases with increasing frequency), and the phase modulation due to a positive non-linear refractive index, or otherwise from the balance of a normal dispersion and a negative $n_2$. They are also described by the non-linear Schrödinger equation. Detailed mathematical treatment of spatial and temporal solitons can be found in several text-books and papers [24,25].

*1.4.3* **Vectorial Solitons.** In our previous discussion, we assumed that a spatial soliton has to be considered as a scalar field, which is an acceptable approximation if the field is launched into one of the polarization eigenmodes of the planar waveguide (i.e. TE or TM). More complicated propagation properties are expected when a field is launched simultaneously in the two modes. The propagation of such polarised, or spatial vector solitons, has been discussed in a number of theoretical studies[26], and experimental work has been started recently[27,19].

*1.4.4* **Light Bullets.** Another question that has attracted much theoretical attention recently is the non-linear propagation of pulses under the simultaneous action

---

[24] R. W. Boyd, "*Nonlinear Optics*", Academic Press, (1992)

[25] H. A. Haus and W. S. Wong, "Solitons in optical communications", Rev. of Mod. Phys., **68**, 423 (1996)

[26] D. N. Christodoulides and R. I. Joseph, Opt. Lett., **13**, 53 (1988)

[27] J. U. Kang, G. I. Stegeman, A. Villeneuve, J. S. Aitchison, J.. Europ. Opt. Soc. A, **5**, 583 (1996)

of dispersion and diffraction. In the case of a focusing non-linearity, two different situations can be considered, depending on the sign of the dispersion coefficient. When the dispersion is positive ('normal') the pulse broadens in time, lowering in peak intensity, hence the spatial soliton finally broadens also in space. However, when the dispersion is anomalous, the pulse narrows in time and space, leading to a process analogous to catastrophic self-focusing. With a suitable material system (exhibiting anomalous dispersion and a positive $n_2$) it should be possible to demonstrate such pulse collapse and investigate its application to pulse compression. One of the more interesting questions in this context is the possible coexistence of a spatial-temporal soliton, or "light bullet" [28,29].

*1.4.5* **Discrete Solitons.** We will conclude the discussion on soliton phenomena introducing the concept of discrete solitons. Arrays of passive or active coupled optical waveguides may be employed for several device applications[30]. In particular, it is possible to generate, propagate and control stable localised wave packets in non-linear waveguide arrays. These spatially localised non-linear modes of the array originate from the balance between non-linearity and linear transverse coupling. In analogy to spatial solitons, they are described by a non-linear discrete Schrödinger equation (NLDSE). In sec. 2.2, a few possible solutions for this expression will be discussed.

## 1.5 The Material of Choice: AlGaAs at the Half Band Gap

All the experiments described in this work were performed in AlGaAs, a very attractive optical material for several reasons:

---

[28] D. E. Edmundson, R.. H. Enns, Opt. Lett., **18**, 1609 (1993)

[29] P. M. Goorjian and Y. Silberberg, Opt. Soc. Am. B, **14**, 3253 (1997)

[30] P. Millar, J. S. Aitchison, J. U. Kang, G. I. Stegeman, G. T. Kennedy, W. Sibbett and A. Villeneuve, J. Opt. Soc. Am. B, **14**, 3224 (1998)

1) The direct band gap of III-V semiconductors leads to a very high efficiency in generating light from band to band electron-hole transitions, much superior to IV group crystals. In fact, though Si has a very mature technology and very low processing cost, it presents a main drawback as efficient electro-optical conversion is concerned. To understand this point, we represent a simplified band diagram of a group IV semiconductor in Fig 1.2. Because photons have negligible momentum, or $k$, a transition from the valence band maximum to the conduction band minimum can only be accomplished through the mediation of phonons. Generally, the transition shown requires a photon and one or more phonons, and is a strong function of temperature. A direct transition from the valence band maximum into the conduction band is in principle possible for Si, but requires photons in the ultraviolet regime. The same limitation is present in carrier recombination, as one or more phonon interactions are required for transitions of an electron from the conduction band minimum to the valence band maximum. Electron and holes will recombine predominantly through non-radiative channels, making the design of an efficient light source simply based on bulk Si impracticable.

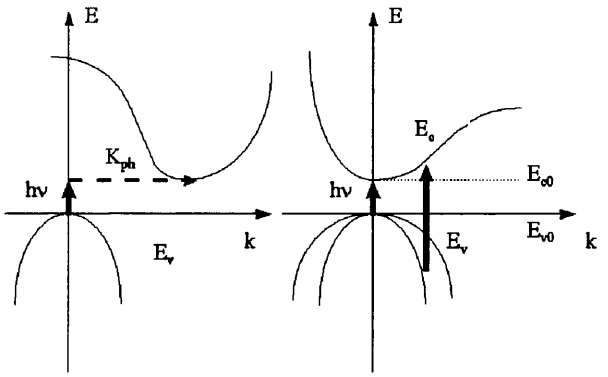


*Fig 1.2* Band diagram of an indirect (left) and a direct (right) band gap semiconductor.

2) The good lattice match for all aluminum compositions of AlGaAs, to GaAs allows an easy design of several wave-guiding configurations. This peculiar property is due to the fact that III-V compounds, and in particular GaAs and AlAs, form crystals with a zinc-blend arrangement. Because of the small lattice

parameter distance between GaAs and AlAs, given by the expression:

$$a_{AlGaAs} = a_{GaAs} + 0.00078x \quad (\text{nm}, 0 \leq x \leq 1), \tag{1.12}$$

the ternary solutions are the closest in the III-V systems to being ideal and are among the easiest to prepare by epitaxial growth. We can observe that the constant *a* varies linearly (Vegard's law) as in many of the III-V ternary alloys[31].

3) Precise control over both the band gap and the refractive index can be achieved by tuning the mole fraction of the Al content in the $Al_x Ga_{1-x} As$ alloy. The band gap energy of AlAs is wider, 2.1 eV, compared to 1.43 eV of GaAs, and all the intermediate values can be achieved by modifying the value of x. The material is highly stable to thermal and hydrostatic perturbations[31], however, for Al concentration bigger than 45% the band gap of the semiconductor becomes indirect.

## 1.6 Waveguide Structures for Non-linear Optics Experiments

All the experiments described in this work were performed in waveguide structures designed to allow guiding of optical waves by making use of multiple total internal reflections from two surfaces. The basic structure guides light between two parallel planes, and it is called a slab waveguide. By confining the wave in a further dimension (adding more surfaces), the light is guided in two dimensions. The new structure is called a channel waveguide. When we design the waveguide for our experiment, we generally require to know the number of modes, the dimension and material that permit only a single mode and the electromagnetic field distribution of the propagating modes.

There is a first, important difference between light propagating in an optical waveguide and in free space. When light is not confined, $k$, the propagation vector,

[31] S. Adachi, J. Appl. Phys., **58**, R1 (1985)

can vary continuously with the frequency $\omega$, but only a certain number of discrete values are allowed for a monochromatic beam propagating in a waveguide.

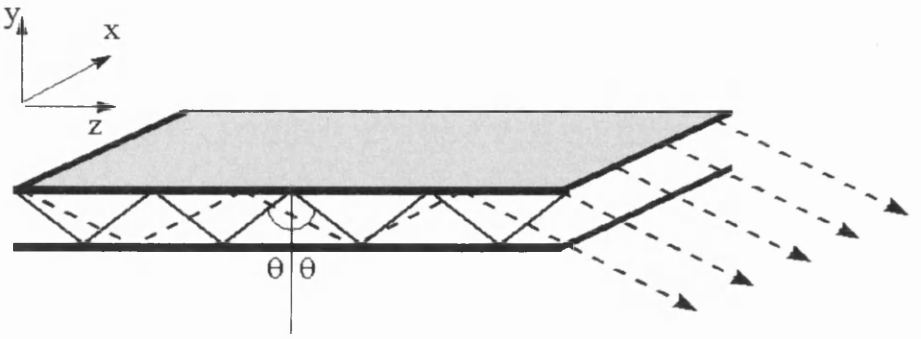


***Fig 1.3*** Studing the propagation of light using a ray-tracing model.

This discrete set of values of $k$ defines the guided modes, which are likewise discrete.

The phenomenon can be understood using a ray-optic model. Even if this approach does not say anything about electrical or magnetic fields, it is enough for designing basic devices.

The simplest structure we can design is constituted by two perfect reflecting mirrors (R=1) for all incident angles (actually, this is a microwave waveguide). This situation is exemplified in Fig 1.3. Every time a wave interacts with one of the mirrors, the incidence angle equals the reflection angle. Nevertheless, only certain values of $\theta$ are allowed regardless of how we illuminate the edge of the sample. This is due to the fact that the wave that undergoes two consecutive reflections must be in phase with the part that had not been reflected, otherwise destructive interference would cause the wave to vanish.

If we consider Fig 1.4, we have:

$$\Delta L = \overline{P_1 P_2} - \overline{P_2 O} \qquad 1.13$$

That is,

$$\Delta L = 2t\cos\theta \tag{1.14}$$

As the number of wavelengths in this interval is $\frac{\Delta L}{\lambda}$, the total phase shift is $\frac{2\pi\Delta L}{\lambda}$ for a wavelength $\lambda$. Keeping in mind that each reflection results in a phase shift of $\pi$, the condition that the waves are in phase after $P_2$ becomes

$$\frac{4\pi\cos\theta}{\lambda}t - 2\pi = 2m\pi \tag{1.15}$$

where $m$ is an integer. We have now the following condition on $\theta$:

$$\theta_{m'} = \cos^{-1}\left(\frac{\lambda m'}{2t}\right) \tag{1.16}$$

where $m' = m+1$, $m'$ =**1,2,3**... The $\theta_{m'}$ are the discrete allowed values of reflection angle, and each of these corresponds to an allowed waveguide mode.

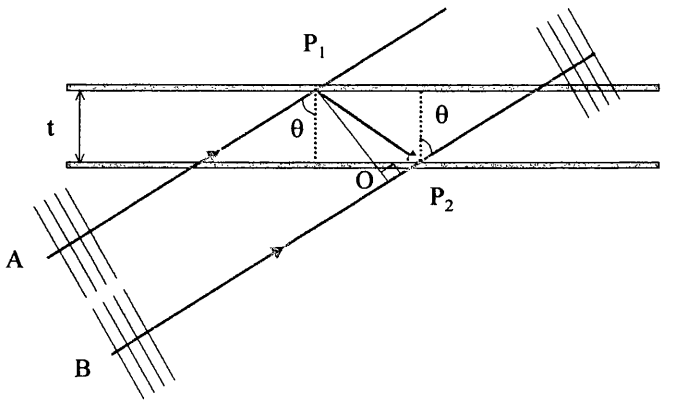


*Fig. 1.4* Only certain modes can propagate in a waveguide structure.

We arrive at a very important result: propagation in a waveguide takes place in the form of discrete modes, each with its own reflection and propagation conditions. We will indicate $m'$ as the $m^{th}$ -order mode. Because the argument of the $\cos^{-1}$ in equation 1.16 must be less than a unit, we have a limit on the maximum permitted value of $m'$:

$$m' \leq \frac{2t}{\lambda} \qquad 1.17$$

The number of allowed modes is hence a function of the relative wavelength. In particular, at the limit $l > 2t$, no modes will be allowed because $2t/l < 1$ but $m' > 1$[32]. This condition is called cutoff and simply implies that the waveguide will not transmit any light. However, if we consider the case of a dielectric waveguide, the phase shift that the wave undergoes after each reflection is dependent on the incident angle, which affects the calculation. The phase matching condition, applying to the dielectric waveguide, assumes the more general form:

$$\frac{4\pi t}{\lambda}\cos\theta - \Phi_u - \Phi_l = 2m\pi \qquad 1.18$$

Total reflection is required for propagation of a mode. In the case in which upper and lower cladding have the same refractive index, the waveguide structure is called "symmetric". As $\Phi_u = \Phi_l$, equation 1.18 can be simplified and becomes:

$$\frac{4\pi t}{\lambda}\cos\theta - 4\tan^{-1}\sqrt{\frac{\sin^2\theta - \sin^2\theta_c}{\cos^2\theta}} = 2m\pi \qquad 1.19$$

where $\theta_c = \sin^{-1}\left(\frac{n_{cladding}}{n_{core}}\right)$ is the critical angle (or total reflection angle).

[32] H. P. Zappe, *"Introduction to semiconductor integrated optics"*, Artech House, London, UK (1995)

A few geometrical considerations allow us to find the expression for the eigenvalue equation for both TE and TM polarization, which are, respectively:

$$\tan\left(\frac{\pi t}{\lambda}\cos\theta - \frac{m\pi}{2}\right) = \frac{\sqrt{\sin^2\theta - \left(\frac{n_g}{n_s}\right)^2}}{\cos\theta} \qquad 1.20$$

$$\tan\left(\frac{\pi t}{\lambda}\cos\theta - \frac{m\pi}{2}\right) = \frac{\sqrt{\left(\frac{n_g}{n_s}\right)^2 \sin^2\theta - 1}}{\left(\frac{n_s}{n_g}\right)\cos\theta} \qquad 1.21$$

In the expression above, $\lambda_0$ is the wavelength in the material, defined as $\frac{\lambda_0}{n_g}$.

Once $m$ is known, equations 1.20 and 1.21 can be solved numerically to yield the correspondent value of $\theta$ and hence the effective index and propagation constants. From eq 1.19 $m_{max}$ can be deduced as:

$$m_{\max} = \text{int}\left[\frac{2t\cos\theta_c}{\lambda}\right] = \text{int}\left[\frac{2t}{\lambda}\sqrt{1 - \frac{n_s^2}{n_g^2}}\right] \qquad 1.22$$

The total number of allowed modes is then given by $m_{max+1}$, which includes the mode $m = 0$. As a consequence, the lowest mode is always allowed, which implies that there is no cutoff in a symmetric waveguide. This is an important fact, considering that rib waveguides fabricated during this work can be efficiently described in terms of a symmetric slab structure by way of the effective index method (Sec. 1.7.1), and always support the fundamental mode. However, in order to simplify the data analysis in non-linear experiments, waveguides must be designed to allow the single $0^{th}$ order mode only. Imposing $m = 0$ in eq. 1.21, we easily

obtain a condition on thickness or refractive index difference between the waveguide and the cladding.

$$t < \frac{1}{2}\lambda\left(1-\frac{n_s^2}{n_g^2}\right)^{-\frac{1}{2}} \qquad 1.23$$

Here $t$ is the maximum thickness for which the guide is still mono-mode; for larger $t$, higher modes will be allowed. We can also write the expression 1.23 in the form:

$$\Delta n \equiv n_g - n_s < n_g\left(1-\sqrt{1-\frac{\lambda^2}{4t^2}}\right) \qquad 1.24$$

to obtain the maximum index step allowing a single mode to propagate.

As expected, thinner waveguides will support a smaller number of modes. If we need to increase the thickness of the waveguide to achieve optimum coupling with the input beam, and still propagate only one mode, it is necessary to design a wafer with a smaller difference between refractive index of cladding and core.

The asymmetric waveguide, where the upper and lower cladding are different, can be solved in precisely the same manner, including two different terms for phase shifts about reflection. The same geometric considerations we made before lead to the eigenvalue equation for TE modes:

$$\tan\left(\frac{2\pi t}{\lambda}\cos\theta-\frac{m\pi}{2}\right)=\frac{\cos\theta\left[\sqrt{\sin^2\theta-\left(\frac{n_c}{n_g}\right)^2}+\sqrt{\sin^2\theta-\left(\frac{n_s}{n_g}\right)^2}\right]}{\cos^2\theta-\sqrt{\left(\sin^2\theta-\left(\frac{n_c}{n_g}\right)^2\right)\left(\sin^2\theta-\left(\frac{n_s}{n_g}\right)^2\right)}} \qquad 1.25$$

and

$$\tan\left(\frac{\pi t}{\lambda}\cos\theta-\frac{m\pi}{2}\right)=\frac{\cos\theta\left[\frac{n_g}{n_c}\sqrt{\left(\frac{n_g}{n_c}\right)^2\sin^2\theta-1}+\frac{n_g}{n_s}\sqrt{\left(\frac{n_g}{n_s}\right)^2\sin^2\theta-1}\right]}{\cos^2\theta-\frac{n_g^2}{n_c n_s}\sqrt{\left(\left(\frac{n_g}{n_c}\right)^2\sin^2\theta-1\right)\left(\left(\frac{n_g}{n_s}\right)^2\sin^2\theta-1\right)}} \qquad 1.26$$

for TM modes. If the conditions $N_{\text{mode}} > n_c$ and $N_{\text{mode}} > n_s$ are both satisfied, internal reflections take place in both lower and upper cladding-core interface. The mode is properly confined and can propagate without leaking in the cladding, e.g. without radiative components. This is the desired condition for our waveguide structures.




***Fig. 1.5*** Lay-out of a strip loaded waveguide.

## 1.7 Numerical Methods for Waveguide Design

*1.7.1* **Two-dimensional Waveguide Analysis: The Effective Index Approximation.** Now that we have considered what is happening in a slab structure, we can move on and analyse how the light is propagating in a strip

loaded waveguide, the building block for all the structures described in this work (Fig. 1.5). The equations used in the case of a slab waveguide are now to be adapted to the two-dimensional case and, in general, solutions can only be determined numerically. However, a simple approximate technique, called the "effective index method", allows us to reduce the analysis required for designing a channel waveguide to coupled one-dimensional problems, still obtaining adequate values for the optical parameters.

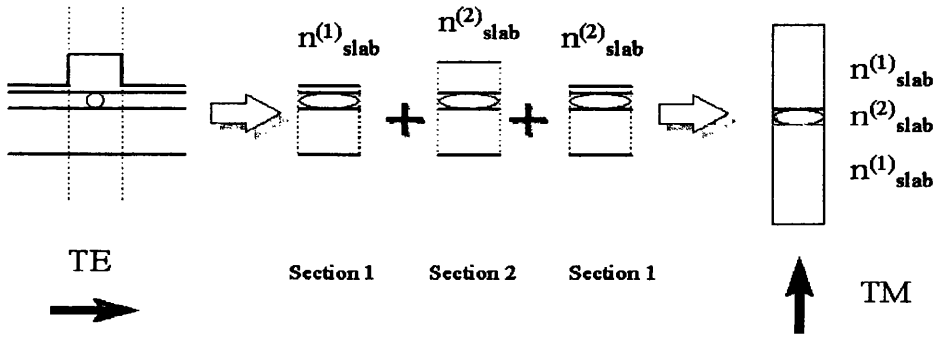


*Fig. 1.6* Effective index method.

If we consider Fig. 1.6, we can think of the channel waveguide as a combination of two slab waveguides in orthogonal directions. From a cut in the y direction we can determine the index for the slab mode in sections 1 and 2, which then become the cladding and core index for a symmetric one-dimensional problem. Equations 1.24 and 1.25 can then be then used to determinate the two-dimensional effective index, $n^{(2)}_{slab}$. The effective index method is a simple and fast approach to predict the optical behavior of weakly guided strip-loaded two-dimensional waveguide, however, it is inaccurate for large index steps and waveguides which are not monomode. In the following section we will describe two packages which have been employed to simulate accurately mode shape and optical parameters.

*1.7.2* **BPM_CAD.** BPM_CAD was written by Optiwave Corporation LTD in order to simulate the propagation of light through any wave guiding medium

using a "step by step" method. As we previously discussed, a waveguide traps light and guides it in a specific direction. An optical waveguide can be thought of as a spatial distribution, or layout, of the refractive index. By considering monochromatic light the time dependence can be neglected and the propagation of the electromagnetic field $E(x,y,z)$ can be described in terms of the Helmholtz equation[33]. We must distinguish between two-dimensional (2D) and three-dimensional (3D) propagation, the dimension referring to the propagation space. The first model is usually employed to describe the electromagnetic behavior of a slab waveguide whilst the latter can be used to find the exact solution in a strip loaded or a rib waveguide. To reduce the computational time, the following approximations are applied to the Helmotz equation.

*Paraxial Fresnel approximation:*

$$\frac{\partial}{\partial z}E(x,y,z)=\frac{i}{2kn_{ref}}PE(x,y,z) \qquad 1.27$$

This approximation is valid for small angles of light propagation, e.g. some tenths of degree, and was accurate enough to model our devices. The paraxial propagator, $P$, has different forms in 2D and 3D propagation. It can be formulated as scalar or semi-vectorial with a reference to polarisation corrections due to dielectric interfaces.

*Paraxial scalar propagator in 2D:*

$$PE=\frac{\partial^2}{\partial x^2}E+k^2\left(n^2-n_{ref}^2\right) \qquad 1.28$$

*Paraxial semivectorial propagator in 2D:*

$$PE=\frac{\partial^2}{\partial x^2}E+k^2\left(n^2-n_{ref}^2\right)+\frac{\partial}{\partial x}\left[\frac{1}{n^2}\frac{\partial}{\partial x}\left(n^2E\right)\right] \qquad 1.29$$

[33] See, for example, D. Yevick, Opt. and Quant. Elec., **26**, S185 (1994)

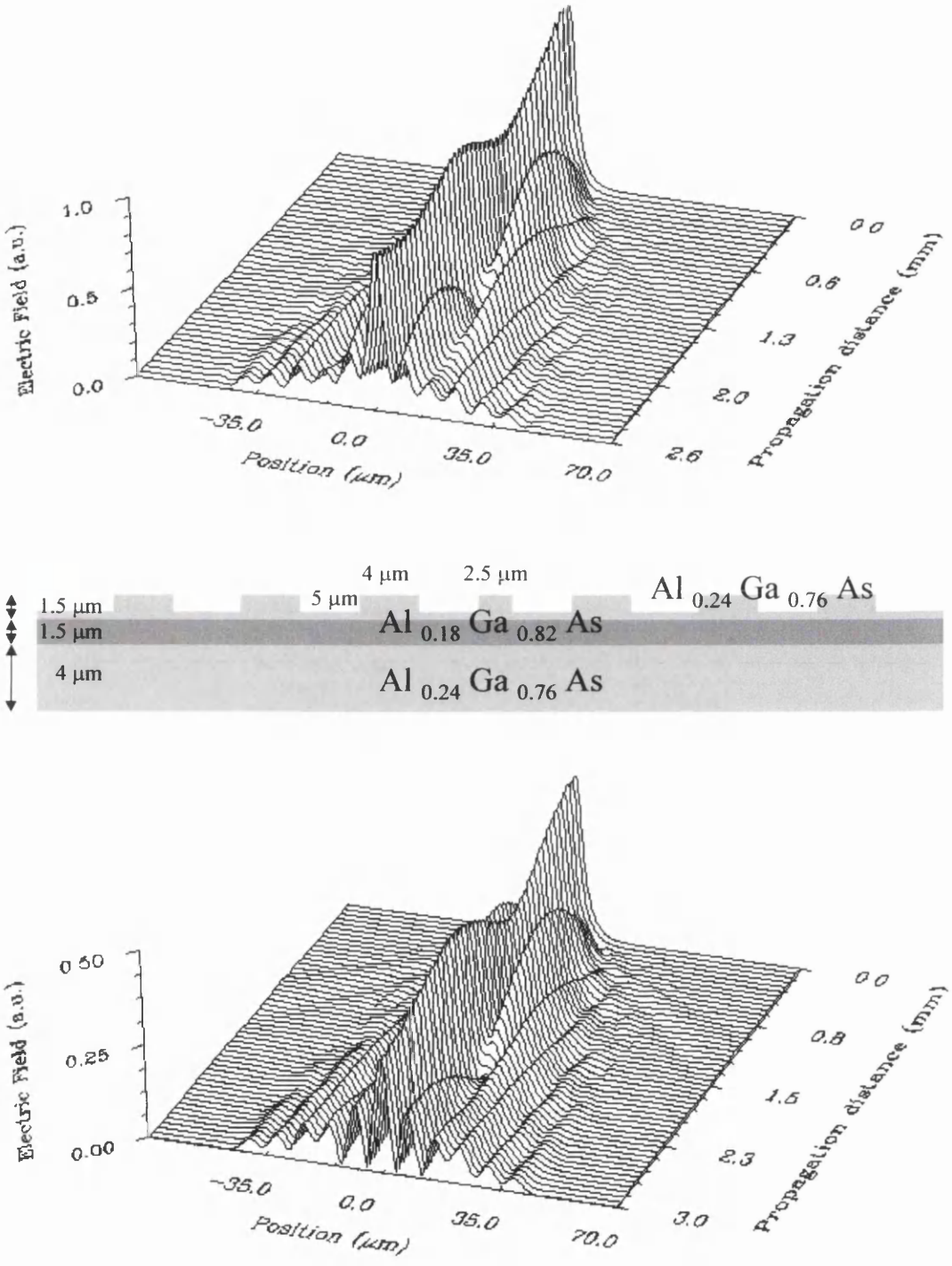


*Fig. 1.7* Comparison between a 2D (top) and a 3D (bottom) BPM. The simulated structure (middle) is a non-uniform array. Only the central waveguide, 2.5 μm wide, was excited. The surrounding waveguides are 4μm wide.

For wide angles of propagation (some degrees), the model has been improved by adding corrections based on Pade' approximants. This method also describes structures with larger refractive indices contrast accurately (variations in the values of the refractive index of 0.1 and above)[34]. Typical examples are silica waveguides or semiconductor-oxide devices.

In 3D propagation we use equations with additional terms corresponding to y-derivatives. The paraxial and wide-angle approximations refer to a constant called the reference refractive index $n_{ref}$.

The equations above are solved with a beam propagation method (BPM) which performs a step-by-step numerical solution along the propagation direction. The field and index are discretised also in the transverse direction based on a numerical mesh. An effective index approach together with a scalar 2D-BPM as proved to be much faster than semi-vectorial 3D-BPM, still producing accurate results. In Fig. 1.7 the simulation of a non-uniform array of waveguides performed with the 3D-solver is compared with the solution obtained using the effective index method in conjunction with the bi-dimensional model. The two different methods show very good agreement.

1.7.3 **F-Wave.** The BPM codes described above "propagate" the initial distribution of the electromagnetic field, which was calculated by using F-Wave. This program, a "mode-solver" written by M. Taylor from University of Glasgow, is based on a finite difference implementation of the vector electromagnetic wave equation. The technique employed requires that the modelled region is covered with a mesh of points at which the fields and indices are sampled, and the mesh is refined during the solution using adaptive mesh technique. The program accurately predicts the optical behavior of the modelled structure, furthermore the discretised values of the field profile can be used to calculate the effective

[34] Hadley, G. R. , Opt. Lett., **17**, 1426, (1992)

area of the mode in the waveguide. Such a quantity is necessary in order to estimate the intensity of the electrical field in the waveguide.

For a scalar field and a scalar spatially homogeneous non-linearity ($n_2$ is constant for all the layers), the Effective Area $A_{eff}^{(3)}$ for the third-order process is defined as:

$$A_{eff}^{(3)} = \frac{\left[\int_{-\infty}^{+\infty}\int_{-\infty}^{+\infty} |E(x,y)|^2 \, dxdy\right]^2}{\left[\int_{-\infty}^{+\infty}\int_{-\infty}^{+\infty} |E(x,y)|^4 \, dxdy\right]} \qquad 1.30$$

where $E(x, y)$ is the field profile of the waveguide. Similarly, the effective area $A_{eff}^{(5)}$ for a fifth-order process (which must be used, for example, to estimate the 3PA coefficient, see Sec. 1.3.2) can be written as:

$$A_{eff}^{(3)} = \frac{\left[\int_{-\infty}^{+\infty}\int_{-\infty}^{+\infty} |E(x,y)|^2 \, dxdy\right]^3}{\left[\int_{-\infty}^{+\infty}\int_{-\infty}^{+\infty} |E(x,y)|^6 \, dxdy\right]} \qquad 1.31$$

Once the field profile generated by F-wave is known, it can be converted in an ASCII file and integrated to obtain the values 1.30 and 1.31. In the following paragraph we will describe the photo-lithographic steps involved in transforming a modelled waveguide into a real and working devices.

## 1.8 Fabrication of Waveguides and Waveguide Arrays

The rib waveguides (and the waveguide arrays) were fabricated in a class 100 cabinet inside a class 10000 clean room to ensure clean patterning of the samples. A chip of

appropriate dimensions was initially cut using a scribe and cleave technique and pre-cleaned before patterning. This is a crucial stage as dirt and grease particles present on the surface of the samples can cause poor resist adhesion and a non-uniform coating layer, drastically affecting the quality of the pattern produced. The cleaning procedure involved the use of an ultrasonic bath to agitate the sample for about five minutes while it was immersed in a sequence of four solvents: *opticlear, acetone, methanol and R.O. water.* To assure that no residual water was present on the surface, the sample was blown dry using filtered $N_2$ and placed on a hot plate at ~45°C for, at least, 10 minutes, or baked in an oven at 130 C° for 5 mins. This step assured a good adhesion of the photoresist (Shipley S1818), dispensed on the surface through a syringe filter and then spun at a rotation speed of 4000 rpm for 30 s to achieve a uniform resist coating thickness of 1.8 μm. In principle, a coating thickness of 0.5 μm could alternatively be achieved by using Shipley S1805 resist with the aim of a better resolution of the pattern. However, this alternative technique presented important drawbacks. The thinner resist layers were more sensitive to the quality of the process and also responsible for a poorer quality of the waveguide side-walls for deep etching in AlGaAs (1 μm or more). Subsequently, the sample was soft-baked at 90°C for 30 minutes to remove most of the solvent in the resist coating and hence making the resist photosensitive. Exposure of positive resist to UV light, which renders the resist soluble to developer solution, was used to transfer the waveguide pattern via a standard chrome mask onto the AlGaAs samples.
This chrome mask, which was designed using an Autocad package (Wavemaker) and produced by E-beam writing, was carefully positioned above and in contact with the coated AlGaAs sample using a mask aligner. The standard procedure requires UV exposure of the S1818 resist through the mask for 12 seconds, and immersion of the sample in a 1:1 solution of AZ developer and R.O. water followed by gently agitating the processed chip in the solution for about 75 s.

However, regardless of the fact that great care was devoted to the alignment process, resist tended to accumulate on the corners of the specimen reducing the contact between mask plate and substrate. We found that a better reproduction of

the pattern could be achieved by decreasing the exposition time up to 5.5 secs and increasing the developing time up to 2.5 mins, still assuring an excellent quality of the waveguides.

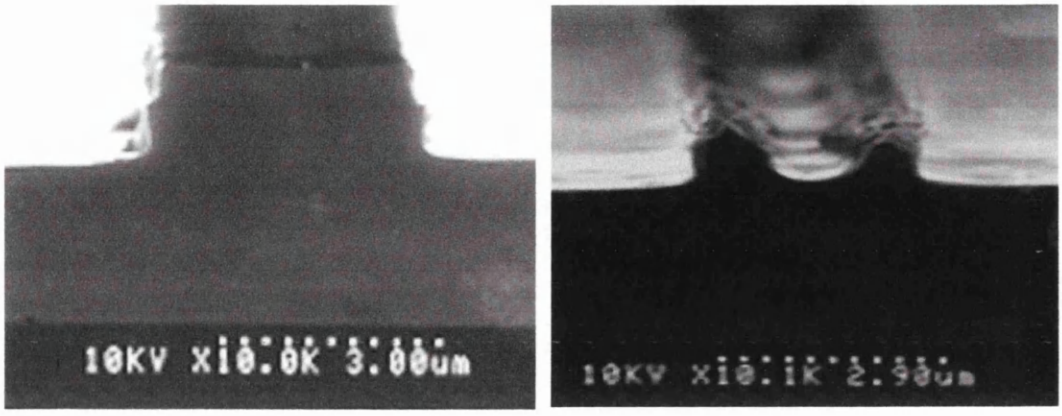


*Fig. 1.8* Dry-etching using S1805 resist as a mask. For etch depth around 1μm, the resist layer is not thick enough and the waveguide is damaged (right). The problem, not present when using a thicker mask (S1818) can be solved by post-baking the sample for 30 minutes at 120 C° (left).

Once the step above was completed, the sample was rinsed again in R.O. water and dried on a hot plate, and finally post-baked at 130 C° for 30 mins, in order to harden the resist.

In the last step of the process, the patterned sample was etched using a SiCl4 reactive ion etching , with the aid of an interferometer to monitor the etch depth of the guides. A profilometer (Decktec) and SEM microscopy has being used to verify the accuracy of the process.

## 1.9 The Laser Source: Beamlock-Tsunami-Opal System by Spectra Physics

In one of the most recent and interesting experimental efforts directed toward the investigation of spatial solitons in AlGaAs waveguide[35], the author considers how

[35] J. U. Kang, "Spatial solitons in AlGaAs waveguides", *Ph.D. Thesis*, Orlando, USA (1996)

*"The most important thing in my work was having the right material. Without an appropriate material in which to observe and study spatial solitons, a spatial soliton is only the solution of NLS that exists on paper. Fortunately, the AlGaAs below the half band gap existed, and it provided an excellent laboratory to study and demonstrate a few useful aspects of spatial soliton".* On my account, as excellent growing and fabrication facilities are present in University of Glasgow, I probably tended to under-estimate my luck in favour of some form of astonishment in front of a stable, ultrashort, powerful laser source at 1.55 μm, to the point to be tempted and rewrite the sentence above as: *"The most important thing in my work was having the right laser source. Without an appropriate source of light, the AlGaAs below half the band would have been just a nice, shiny piece of semiconductor".* However, after making sure that a non-linear optics experiment is a combination of a few favorable circumstances, we can describe in more detail the optical system employed to perform the experiments described in this work.

The laser source was a SPECTRA PHYSICS OPO (Optical Parametric Oscillator) consisting of three lasers, Beam lock- Tsunami- Opal, aligned in sequence.
Beam Lock is a high power, stable and beam-pointing green source delivering more than 10 W @ 500 nm to a titanium-doped sapphire laser (Tsunami). Due to a very large fluorescence bandwidth extending over 400 nm and to a high stability phase-looked loop cavity, it is possible to generate 100-200 fsec mode-locked pulses with a repetition rate of 80 MHz, up to an average power of 1.5 W @ 790 nm. Such pulses are delivered to Opal in order to generate ultra-short pulses in the 1.4 μm - 1.6 μm spectral region. Optical Parametric Oscillators (OPOs) use a non-linear optical crystal (LBO) in an oscillator cavity to generate new frequencies (signal and idler) from an input coherent source. Parametric oscillation is a non-linear three-wave process and requires materials with a large second order susceptibility ($\chi^{(2)}$). In an OPO, energy conservation dictates that:

$$\frac{1}{\lambda_{pump}} = \frac{1}{\lambda_{signal}} + \frac{1}{\lambda_{idler}} \qquad 1.32$$

and momentum conservation requires

$$\vec{k}_{pump} = \vec{k}_{signal} + \vec{k}_{idler} \qquad 1.33$$

Where $\vec{k} = \frac{2\pi}{\lambda}$. By using birefringent non-linear crystals, the latter condition is satisfied through phase matching, which governs the absolute signal, the idler output and defines the operational frequency. In a singularly resonant OPO, only one of the generated wavelengths (determinate by the optical coatings of the cavity mirrors) is resonated in the cavity. Unlike a laser, an OPO has an instantaneous gain response to the intensity of the pump laser. Output is generated only when the pulse generated by the titanium-sapphire laser is present in the non-linear crystal. For CW mode-locked systems, this necessitates a synchronous pumping condition in which the mode-locked pump cavity is precisely matched to the cavity length of the OPO. Sub-picosecond output pulses require that the cavity match must be better than 5 μm. Hence it is necessary to use an actively length-stabilised OPO cavity.

## 1.10 Description of the Experimental Set-up.

The apparatus used to perform the non-linear experiments described in this thesis is shown in Fig. 1.8. The light source consisted of a synchronously pumped optical parametric oscillator (Spectra Physics Tsunami-Opal System), described in paragraph 1.9.

Initial coupling of the laser light into the strip loaded guides was achieved by using an end-fire rig as shown below and a camera and TV monitor to check visually if light was guided. The beam was focused into the guides using a X40 objective and the output was also collected using a X40 objective, and focused onto a camera, spectrum analyser and power meter. A telescope was built up to optimise the position of the output focal point, and a narrow slit was also employed to clean the light propagating in the slab during the coupling operations.

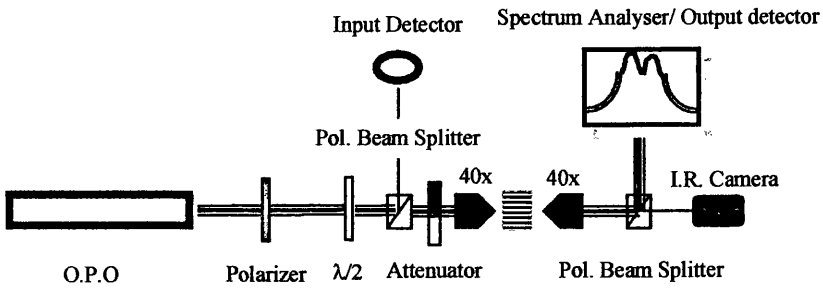


*Fig. 1.9* Typical set-up for non-linear optics experiments.

A half wave plate and a polariser on a kinematic mount were placed in front of the laser (with an electrical field oscillating parallel to the optical bench plane) to ensure light going into the sample was properly polarised. A neutral density filter with variable attenuation was also placed in front of the end fire rig in order to control the amount of light coupled into the sample and also in front of the I.R. camera to prevent the saturation of the device. Finally, the beam splitters and the input and output photo detectors were accurately calibrated to account for polarisation and environmental noise introduced by other light sources in the lab.
All experiments were conducted at the Weizmann Institute of Science, Rehovot, Israel.

## 1.11 Summary of Chapter 1

In this chapter we have discussed the possibility of designing and realising ultrafast telecommunications systems using optical solitons as the elementary unit of information. In particular, differently from standard light beams, mutual interactions and optical steering are possible for spatial solitons in slab waveguides. General non-linear optics as well as specific examples such as Self-Phase Modulation and non-linear absorption have been discussed, as they are fundamental to understand the behaviour of real non-linear devices. We also described the numerical and experimental techniques necessary to fabricate the non-linear waveguide arrays in which we generated and propagated, for the first time, a discrete spatial soliton.

# Chapter 2

# *Solitons in Arrays of Waveguide*

In Section 1.3, we showed that light beams can trap themselves by creating their own waveguide through the non-linear optical Kerr effect. Spatial solitons originate from a balance between the material non-linearity and diffraction, which must be confined in one transverse dimension to avoid catastrophic self-focusing. Experimental demonstrations in planar waveguides, where one dimension is confined by the waveguide, have been recently reported[36]. These optical solitons are a solution of the fundamental (1-D) non-linear Schrödinger equation (see also Sec. 1.4.1):

$$\frac{dE}{dz} = \frac{i}{2k}\frac{d^2E}{dx^2} + ik_0 n_2 |E|^2 E, \qquad 2.1$$

where the normalisation condition $|E|^2 = I\left[\frac{\mathrm{W}}{\mathrm{m}^2}\right]$ was assumed. This equation represents a member of a wider class of partial differential equations with solitary solutions. A phenomenon similar to spatial solitons has been predicted in an infinite array of identical, weakly coupled waveguides[37,38]. In such an array, when low intensity light is injected into one or a few waveguides, it will couple to more and more waveguides as it propagates, thereby broadening its spatial distribution. This widening distribution is analogous to diffraction in continuos media. A strong intensity changes the refractive index of the input waveguide through the optical Kerr effect and decouples it from the rest of the array. It has been shown that particular light distributions propagate while keeping a fixed spatial profile localised in a limited number of waveguides, in an analogous way to spatial solitons. These are

---

[36] J. S. Aitchison, Y. Silberberg, A. M. Weiner, D. E. Leaird, M. K. Oliver, J. L. Jackel, E. M. Vogel and P. W. E. Smith, J. Opt. Soc. Am. B, **8**, 1290 (1990)

[37] D. N. Christodoulides and R. I. Joseph, Opt. Lett., **13**, 794 (1988)

[38] A. B. Aceves, C. de Angelis, T. Peschel, R. Muschall, F. Lederer, S. Trillo, and S. Wabnitz, Phys. Rev. E, **53**, 1172 (1996)

named discrete spatial solitons. Investigating the behaviour of discrete solitons in arrays of waveguides is of particular interest due to the fact that their mathematical description and localised solutions appear in several other fields. For example, this equation describes localised modes in molecular systems[39], polarons in one-dimensional ionic crystals[40], localised modes in electrical lattices[41] and a coupled array of mechanical pendulums[42].

These localised modes are an example of the more general phenomenon of discrete breathers[43] to which discrete solitons belong. A discrete breather exhibits time periodicity and (at least) exponential localisation in space, without being confined to certain lattice dimensions. The advantage of investigating a non-linear optical array instead of molecular systems is mainly due to the fact that those phenomena associated to soliton formation, motion, steering and localisation appear on an accessible spatial scale. Besides this fundamental interest the practical importance of waveguide arrays should also be mentioned. They are regarded as promising candidates for all optical signal switching, routing and steering applications. They exhibit the flexibility and multiport capability of continuous systems but still maintain the well defined field shape of single mode waveguides, allowing for further processing of the optical signals.

In this chapter we will discuss our experimental results regarding the generation of discrete solitons in AlGaAs waveguide arrays, and their novel non-linear steering properties. We will also show that it is possible to tailor the effective index profile of the individual guides and obtain a non-linearly induced escape from a defect state.

---

[39] A. S. Davydov and N. I. Kislukha, Phys. Status Solidi, B **59**, 465 (1995)

[40] T. Holstein, Ann. Phys., **8**, 325 (1959)

[41] P. Marquie, J. M. Bilbault, and M. Remoissenet, Phys. Rev. , E **51**, 6127 (1995)

[42] P. Denardo, B. Galvin, A. Greenfield, A. Larranza, S. Putterman and W. Wright, Phys. Rev. Lett., **68**, 1730 (1992)

[43] S. Flach and C. R. Willis, Phys. Rep. **295**, 182 (1998)

## 2.1 Non-linear Multi-Core Directional Couplers in AlGaAs

Non-linear directional couplers have been extensively researched since the first theoretical investigation by Jensen[44]. They operate on the principle that an exchange of optical power can occur between adjacent guides of an array when the guides are placed in close proximity to one another, such as when the evanescent field mode tails of the guides overlap. In addition, the guides must also be phase-matched, or have the same propagation constant. The power transfer of light between the guides is then a periodic function of the device length. This is shown schematically in Fig. 2.1.

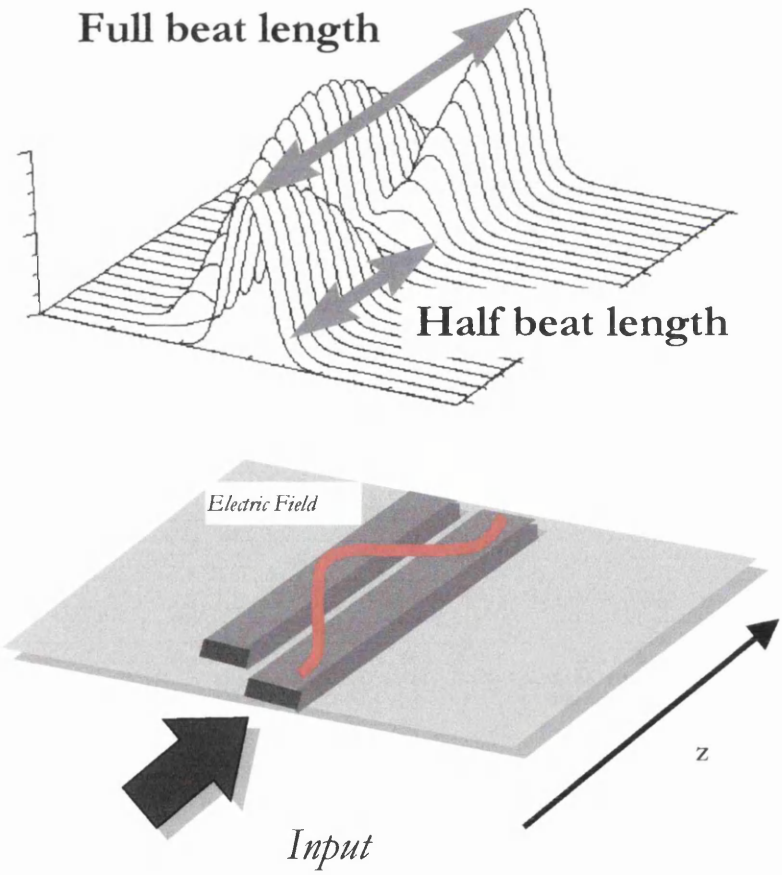


***Fig 2.1*** The Two-core Coupler. The schematic (BOTTOM) and the evolution of the intensity along the waveguide (TOP).

[44] S. M. Jensen, IEEE J. Quant. Electron., **18**, 1580 (1982)

The propagation of light within a linear directional coupler is generally described by coupled mode theory. The evolution of the electric fields along m-coupled waveguides can be expressed as:

$$\begin{cases} i\dfrac{dE_1}{dz} + \beta E_1 + CE_1 + \gamma|E_1|^2 E_1 = 0 \\ \vdots \\ i\dfrac{dE_n}{dz} + \beta E_n + C(E_{n+1} + E_{n-1}) + \gamma|E_n|^2 E_n = 0 \\ \vdots \\ i\dfrac{dE_m}{dz} + \beta E_m + CE_m + \gamma|E_m|^2 E_m = 0 \end{cases} \qquad 2.2$$

where $E_n$ (n=1,...,m) is the amplitude of the electric field in the n$^{th}$ waveguide (defined as in Eq. 1.8), $\beta$ is the propagation constant of the mode in the guides, $C$ is the linear coupling coefficient, $\gamma = \omega_0 n_2 / cA_{eff}$, $n_2$ is the non-linear coefficient and $A_{eff}$ is the common effective area of the mode. At low powers, the non-linear terms of Eqs. 2.2 can be ignored. The infinite set of ordinary differential equations is then integrable[45]. The solutions for the electrical field in the n$^{th}$ waveguide, when only one waveguide is excited, is a set of Bessel functions. If we set the initial conditions $E_0(z=0) = A_0$ and $E_{n\neq 0}(z=0) = 0$, the solution for the electrical field in the n$^{th}$ waveguide is given by:

$$E_n(z) = A_0(i)^n \exp(i\beta z) J_n(2Cz) \qquad 2.3$$

where $J_n$ is a Bessel function of order n. This distribution is displayed in fig. 2.2 a). As the light propagates along the waveguides, the energy spreads into two main lobes with several secondary peaks between them. The solution under any other initial conditions will be a linear superposition of Eq. 2.3.

When the intensity varies slowly over adjacent waveguides, the discrete set of ordinary differential equations (Eqs. 2.2) can be reduced to the non-linear Schrödinger equation which describes spatial solitons[46]. It has been shown numerically[37,47] that, a starting field distribution such as

---

[45] See, for example, M.C. Gabriel and N. A. Whitaker, Jr., J. Light. Wave Tech., **7**, 1343 (1989)

[46] V. E. Zakharov and A. B. Shabat, Sov. Phys. JEPT, **34**, 62 (1972)

[37] D. N. Christodoulides and R. I. Joseph, Opt. Lett., **13**, 794 (1988)

$E_n(z) = A_0 \exp[i(2C + \beta)]\text{sech}\left[\frac{X_n}{X_0}\right]$ where $X_n$ is the location of the $n^{th}$ waveguide and $X_0$ is the characteristic width, will result in a localised propagating distribution for sufficiently high power levels. This localisation is known as a discrete spatial soliton.

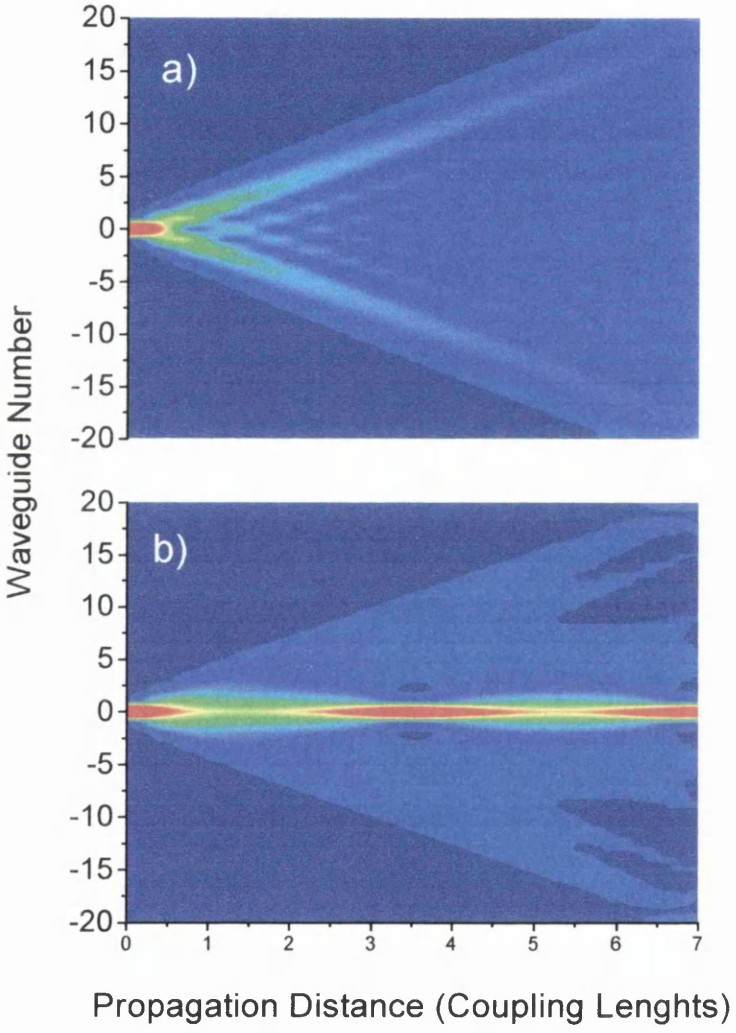


***Fig. 2.2*** a) Discrete diffraction in a non-linear waveguide array and b) formation of a discrete soliton. These simulations assume a peak power equal to 0.05 and 1 KW, respectively.

[47] A. C. Scott and L. Mac Neil, Phys. Lett. A, **98**, 87 (1983)

## 2.2 Implications for All Optical Switching

Numerical simulations show that these localised field distributions share a few basic properties with solitons and differ in a few other respects[48]. By introducing the new fields $Q_n = \sqrt{\gamma/2C}E_n \exp(-i(\beta+2C)Z)$ Eq. 2.1 can be transformed into the standard Discrete Non-linear Schrödinger Equation (DNLSE):

$$\begin{cases} i\dfrac{dQ_1}{d\xi} + (Q_2 - 2Q_1) + 2|Q_1|^2 Q_1 = 0 \\ \vdots \\ i\dfrac{dQ_n}{d\xi} + (Q_{n+1} + Q_{n-1} - 2Q_n) + 2|Q_n|^2 Q_n = 0 \\ \vdots \\ i\dfrac{dQ_m}{d\xi} + (Q_{m-1} - 2Q_m) + 2|Q_m|^2 Q_m = 0 \end{cases} \qquad 2.4$$

where $\xi = CZ$ is the normalised propagation distance.

In general, the DNLSE appears as a natural discretisation of the non-linear Schrödinger equation (NLSE). However, whilst the latter is integrable, the behaviour of the DNLSE must be described in terms of approximate analytical solutions or by way of numerical methods.

Several theoretical works have shown that it is possible to identify three different operation regimes for a Non-linear Waveguide Array (NWA)[48]. The first regime, also known as the long wavelength limit (valid for weak confinement) can be well described by the usual continuum approximation which leads to the NLSE. Mathematically, such an approach consists of introducing the function $q(x,\xi)$ with $q(x=n,\xi) = Q_n(\xi)$ and by expanding the linear term in a Taylor series around $x=n$. The solution of the discrete problem has the same form and properties as the well known solutions of the completely integrable NLSE[46] (see Fig. 2.3, b) and c)). The second regime (intermediate) is depicted by an extended continuum approximation. This approach consists of using a trial function which is a one soliton solution of the

---

[38] See again, for example, A. B. Aceves, C. de Angelis, T. Peschel, R. Muschall, F. Lederer, S. Trillo, and S. Wabnitz, Phys. Rev. E, **53**, 1172 (1996)

[46] V. E. Zakharov and A. B. Shabat, Sov. Phys. JEPT, **34**, 62 (1972)

continuous NLSE for a beam centred at the position $x_0$, and a phase difference k between adjacent fields. It is assumed that the beam amplitude and width are independent, and a variation of the beam width μ upon propagation is also allowed. Finally, the behaviour of the discrete self trapped (DST) modes in the third regime of strong confinement, may be captured by a truncated three mode description of the array. On a practical point of view, this is reflected in the absence of interactions of two strongly trapped solitons, where the DST solitons remain stable even when they are closely packed into the array (see Fig. 2.3, a)). Totally different is the behaviour of two or more weakly confined beams co-propagating along a NWA, which show the particle-like properties typical of solitons (Fig. 2.3, b) and c)).

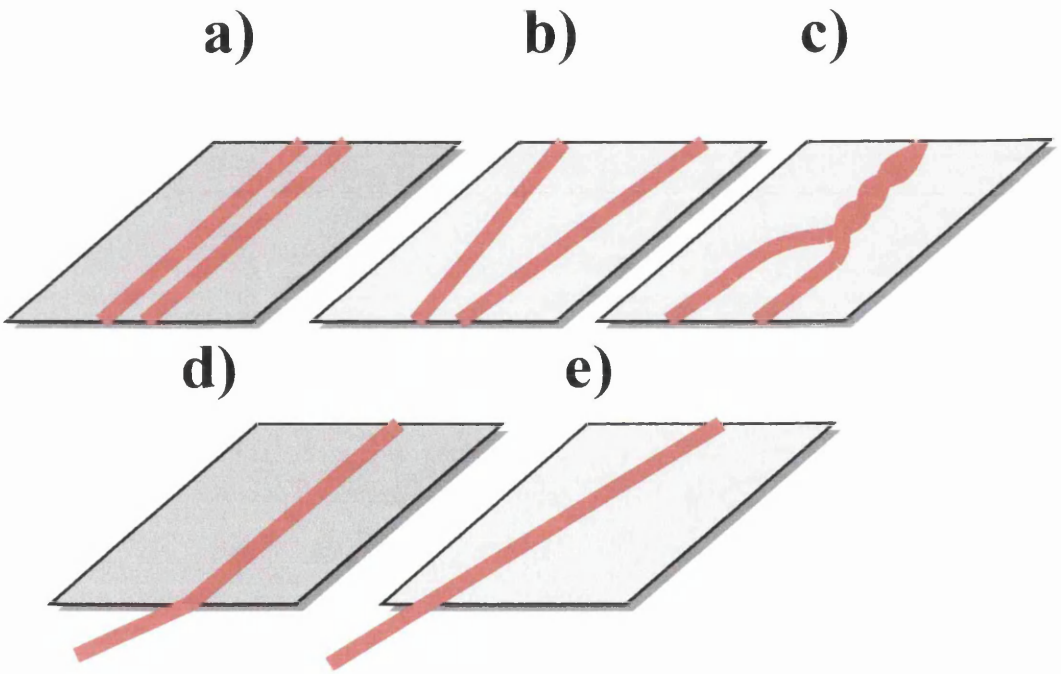


***Fig. 2.3*** TOP: a) Lack of interaction for 2 co-propagating discrete solitons in a weakly coupled array (a) as opposed to the significant mutual interactions in a strongly coupled array. The solitons are out of phase and in phase ( b) and c), respectively). BOTTOM: a trapped soliton in a weakly coupled array (d) and a moving soliton in a strongly coupled array (e).

As a further consequence, beam steering can be achieved by imposing a linear phase variation across the transverse profile, which simply corresponds to tilting the input beam, in the case of weakly confined DST modes (see Fig. 2.3, e)). On the other

hand, the localisation effect in a strongly confined, high power, self-trapped beam can counterbalance, and even cancel the tendency of a tilted beam to travel obliquely across the array (see Fig. 2.3, d)). It has also been shown that the location of the centre of the soliton, whether centred on a waveguide, or in between two waveguides, has an effect on the stability of the solution to small tilts of the phase. Briefly, a solution centred in between waveguides is easier to steer than a soliton centred on a guide.

Clearly the possibility of controlling the location of the array output is very attractive from the point of view of all-optical switching applications.

## 2.3 Design and Fabrication of the Waveguide Arrays

In this section the design and fabrication of samples used in this project will be reviewed. A number of parameters are particularly important, in particular the strength between the guides, $C$, depends on the coupled waveguide structure and can be approximated by:[48]

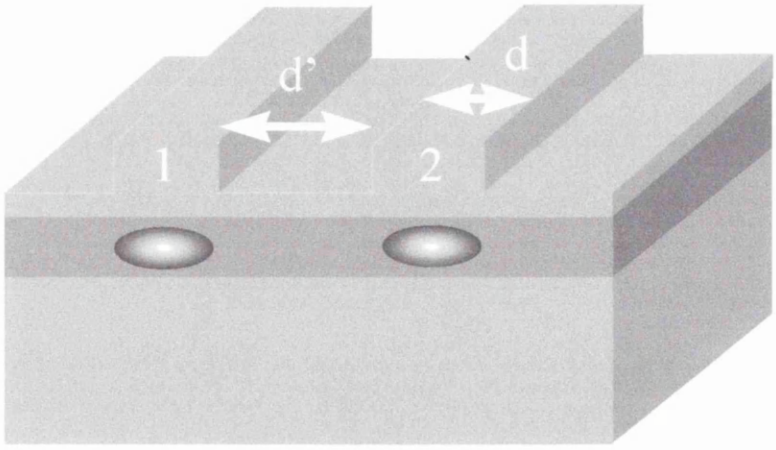


***Fig. 2.4*** Schematic representation of the section of a Two Core Coupler.

[48] P. Millar, "*Non-linear Propagation Effects in Periodic Microstructures*", Ph.D. Thesis, University of Glasgow, Glasgow (1997). The method described here uses an effective index approach.

$$C_{12} = \frac{2k_0^2\left(n_2^2 - n_1^2\right)\alpha_x \cos^2\left(k_{2x}\frac{d}{2}\right)}{\beta d_{eff}\left(\alpha_x^2 + k_{2x}^2\right)} \exp\left(-\alpha_x d'\right) \qquad 2.5$$

where $n_1$ and $n_2$ are the effective refractive indices of the etched slab region and the unetched region under the guides respectively, $d'$ is the edge to edge separation of the two waveguides, $k_0$ is the wave number given by $2\pi/\lambda$ and $d_{eff}$ is the effective waveguide width, which is defined as:

$$d_{eff} = d + 2\left(\frac{1}{\alpha_x}\right) \qquad 2.6$$

In formula 2.5 $\alpha_x$, $k_{2x}$ represent the transverse propagation constants of light travelling within the regions 1 and 2 respectively, and are given by the following equations:

$$\alpha_x = k_0\sqrt{n_{eff}^2 - n_1^2} \qquad 2.7$$

$$k_{2x} = k_0\sqrt{n_2^2 - n_{eff}^2} \qquad 2.8$$

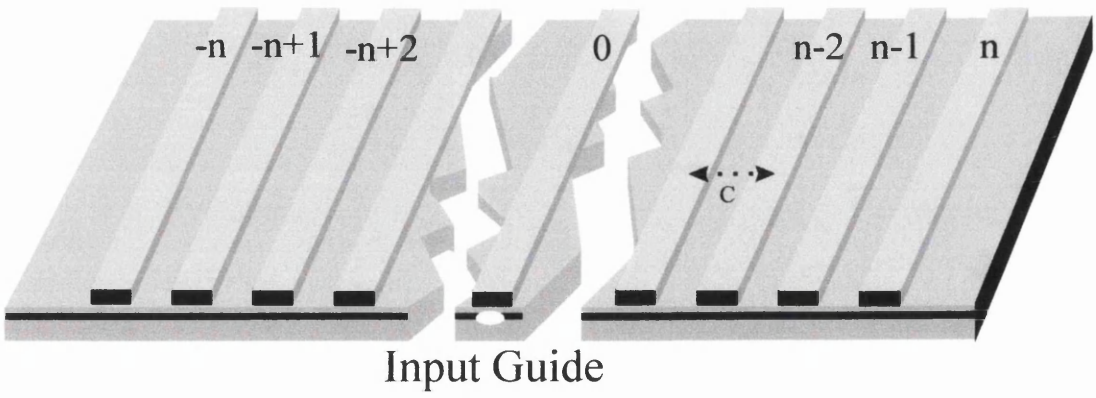


***Fig. 2.5*** Schematic view of a N-core coupled array.

where $n_{eff}$ is the effective index of an individual waveguide.

The coupling length, $L_c$, is defined as the length over which power is transferred from the input guide to the adjacent guide. This is depicted in Fig. 2.1. Fig. 2.5 shows a schematic of a 1x(2N+1) coupler array, where the $C$ coefficients are the linear coupling coefficients between the guides (supposed, for simplicity, to be constant). A two-guide coupler of length $L_c$ is known as a half beat length device. A full beat length device has a length $2L_c$ and corresponds to all the power exiting from the input guide.

The coupling length is related to the coupling strength by the following equation:

$$L_c = \frac{\pi}{2C_{12}} \qquad 2.9$$

Theoretically, it has been found that the coupling length of a 1xN array , where $N$ is the number of guides, is related to the half beat length of a 1x2 array, $L_C$, by the following relation[49]:

$$L_N = \sqrt{(N-1)}L_C \qquad 2.10$$

where $L_N$ is the half-beat coupling length of the N-core array (if we assume to inject the field in the outermost waveguide). Eq. 2.10 shows that the half-beat coupling length of the array, increases as the number of guides within the array increases.

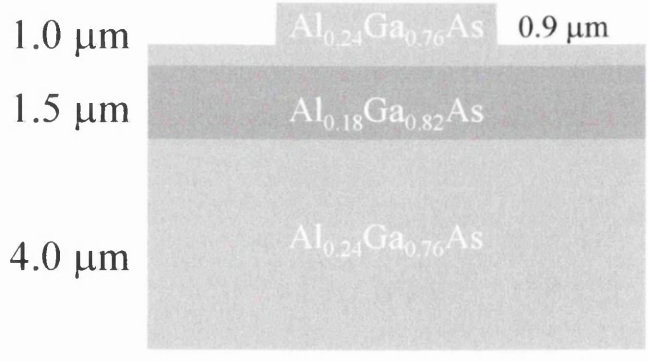


*Fig. 2.6.* Typical AlGaAs waveguide structure.

[49] Y. Chen, A. W. Snyder and D. L. Mitchell, Electron. Lett., **26**, 77 (1990)

The theory above was used to carry out an initial estimation of the coupling length of the array. The optical properties of the ridge waveguide structures were calculated using the effective index method in first instance and subsequently a more refined analysis of the fields profiles was performed using F-Wave (see section 1.7.3). Hence, the global behaviour of the array at low power was simulated using a commercial BPM (developed by Optiwave, see section 1.7.2) and compared with the non-linear results discussed in Sections 2.5 and 2.6.

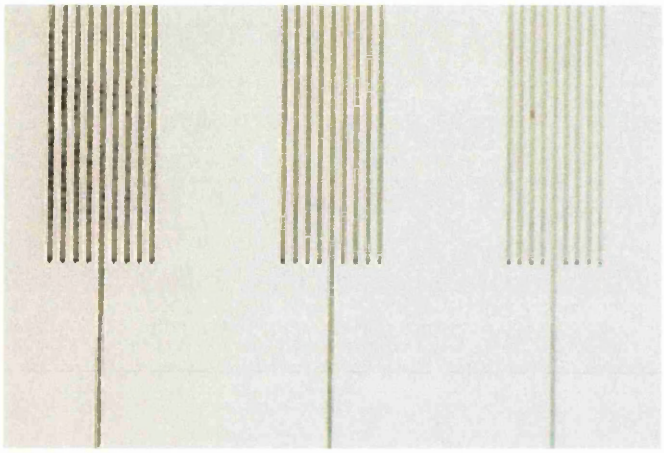

*Fig. 2.7.* Optical microscope view of a 1x9 coupler mask.

## 2.4 Initial Sample Fabrication

Ridge waveguides were fabricated on a 3 layer AlGaAs wafer, the structure of which is shown in Fig. 2.6. Strip loaded waveguides, 4 μm wide, were etched 0.8-0.9 μm into the upper cladding, using a combination of standard photo-lithography and reactive ion etching with SiCl4. The sample consisted of 7 groups of 9 core coupler arrays, with an increasing distance between the waveguides and hence, a decreasing coupling strength. In Fig. 2.7 a detail of the mask is represented.

The experimental set-up described in Fig. 1.8 was also used to test the waveguide arrays samples. An Analogue to Digital Converter (SPIRICON) was connected to the I. R. camera in order to accurately determinate the power distribution in the devices.

*2.4.1* **Theoretical Modelling.** The theoretical modelling of the arrays investigated in the preliminary results was performed in collaboration with Ulf Peschel and Thomas Pertsch from Jena University. The following steps were carried out.

1) Effective index calculations of the structure were exploited to verify that the numbers match the values we found using F-Wave.

2) Vectorial FEM (Finite Element Method) calculations were performed to model our structure. The calculations gave the fields for the TE and TM modes of the waveguide and the effective areas as well. The super modes of the nearest neighbour coupling were calculated and used to estimate the half beat coupling length for the arrays.

3) The previous parameters were used to run a coupled mode analysis[50] of the spatio-temporal behaviour of the waveguide arrays, by expanding equation 2.2 as:

$$\left[ i\frac{\partial}{\partial z} - \frac{D}{2}\frac{\partial^2}{\partial t^2} + i\frac{\alpha_1}{2} + \gamma|E_n|^2 + i\alpha_3|E_n|^4 \right] E_n + C[E_{n+1} + E_{n-1}] = 0, \qquad 2.11$$

where $E_n$ is defined as in Eq. 1.8. We note that the term $\beta E_n$, appearing in Eq. 2.2, was eliminated by way of a simple transformation. Other parameters used were: $\lambda$ = 1.53 μm, third order non-linearity $n_2$ = 1.3*10$^{-13}$ cm$^2$/W, losses = 0.5 dB/cm, *3PA* = 0.07 cm$^3$/GW$^2$, dispersion = -1075 Ps/km nm, FWHM pulse length = 250 fs, sech pulse shape.

4) The coupling lengths of the structures were varied to account for the tolerances of the fabricated devices and, hence, to match the experimental results.

*2.4.2* **Experimental Results.** Initially a 3 mm long array consisting of 9 waveguides was tested.

---

[50] A. A. Hardy, IEEE J. Quant. Elec., **34**, 1109 (1998)

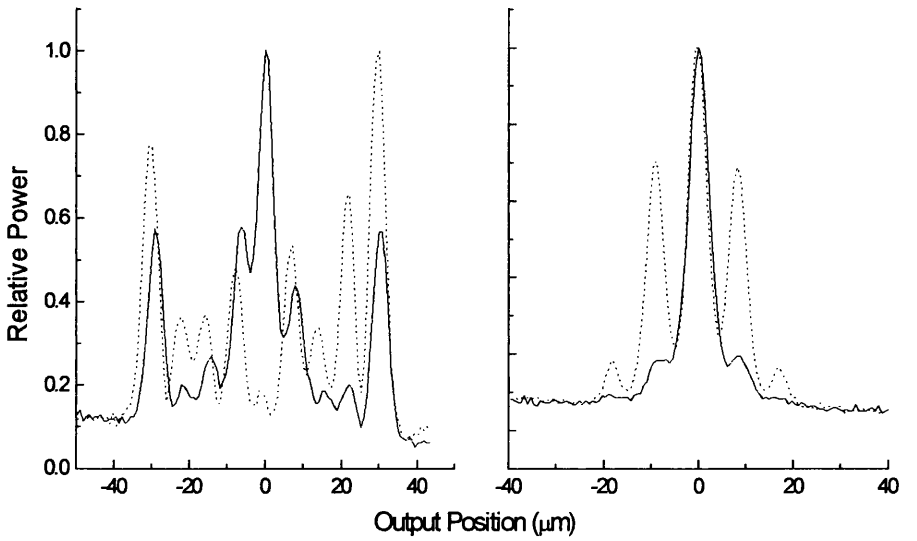


*Fig. 2.8* Power dependent switching characteristic for a strongly (left) and a weakly (right) coupled array, for low (dotted line) and high (solid line) power. The input polarisation was TE.

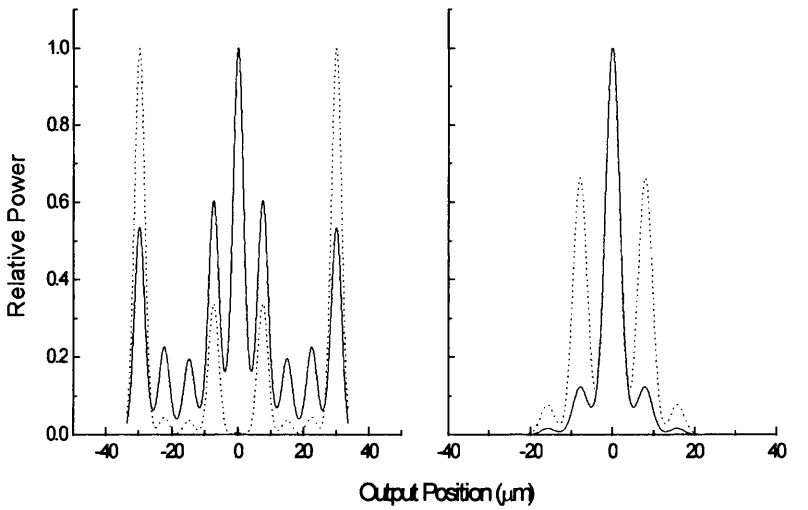


*Fig 2.9* The simulations undertaken using coupled mode theory show an excellent agreement with the experimental data (see Fig. 2.8).

The distance between each waveguide was varied between 3.0 μm and 5.5 μm, in order to vary the degree of coupling in the structure.
The short length of the sample assured low linear loss (around 0.7 dB) and a low dispersion of the pulse. Light was coupled into the central waveguide of the array. The typical switching characteristic of a strongly coupled array (left) and of a weakly coupled array (right) are shown in Fig. 2.8. In order to calculate the power levels, the coupling efficiency η was determined to be 20%. Losses in the optics and reflections at the interfaces further reduce the throughput by a factor 0.4. At low input intensity levels the power distribution at the output spreads to the outer waveguides. As the input intensity is increased there is a localisation of the power to the central waveguide. The length of the weakly coupled sample is less than a half of the coupling length (estimated to be 7.4 mm for the fundamental TE mode and 9.8 mm for the fundamental TM mode). Hence we prefer to use the term "localisation" or "discrete self-focusing" rather than "discrete soliton". In the strongly coupled array, where the coupling length was reduced to 1.675 mm for a $TE_0$ mode, and to 2.248 mm for a $TM_0$ mode, a localisation in the 3 central waveguides was still present. However, as the non-linearity has an instantaneous response time when compared to the temporal width of the pulse, different switching occurs at different points across the pulse envelope. The result is a break-up of the output pulse envelope, with the low intensity wings emerging from the outer waveguides.

The experimental graphs (Fig. 2.7) must be compared with the simulations reported in Fig. 2.9. In the table below, we list the experimental and theoretical power required for switching. Even if the linear loss had been somehow underestimated in the simulation (losses of 0.5 dB/cm against a measured 2.2 dB/cm were assumed), an excellent agreement between the behaviour of the real and the modelled devices is still present . Such statement was verified by simulating the optical behaviour for different values of linear losses. It was shown that the slight difference in the power level required to generate a soliton was less than the variation due to other sources of error, e.g coupling efficiency and fluctuations of the pulse length.

| | Power Level (KW) | | | |
|---|---|---|---|---|
| | *Teo. (TE)* | *Exp. (TE)* | *Teo. (TM)* | *Exp. (TM)* |
| *3 μm Array* | 1.5 | 1.65 | 0.85 | 1.15 |
| *5.5 μm Array* | 0.55 | 0.7 | 0.53 | 0.65 |

***Tab. 2.1*** Theoretical and experimental switching power levels.

A stronger variation of the coupling length between the TE and the TM case was found in the experiments when compared to the calculations. This is probably due to a stress-induced birefringence and it was already observed in similar structures[35].

## 2.5 Second Set of Samples: Observation of Discrete Spatial Solitons

In the second series of experiments we studied 3 sets of arrays composed of 41 waveguides, each 4 μm wide, etched to 0.95 μm in an upper cladding 1.5 μm thick (hence 0.5 μm thicker than the previous structure). Samples with different separation parameters were studied. The separation d affects the coupling coefficient C in Eq. 2.3. In our samples, d was varied between 4, 5 and 7 μm. The mode effective area was about 19 $\mu m^2$ and its ellipticity ratio was about 2.5:1.

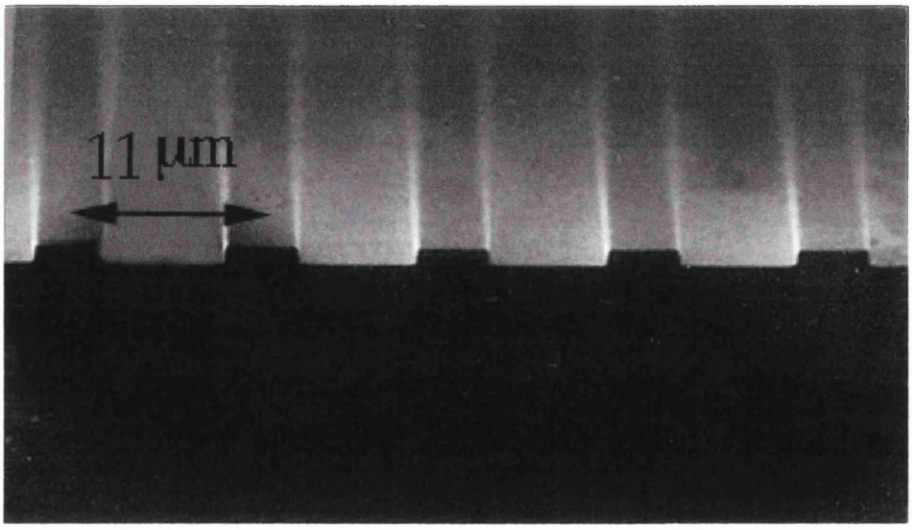


***Fig 2.10*** Micrograph image of a waveguide array.

The input beam was reshaped by a cylindrical telescope into an oval shape in order to match the gaussian beam generated by the laser to the mode of the waveguide. We first present data taken from a 6 mm long array with a waveguide separation of d

[35] J. U. Kang, *"Spatial Solitons in AlGaAs Waveguides"*, Ph.D. Thesis, Orlando, USA (1996)

= 4 μm, which is relatively strongly coupled. The output facet images at various input powers are shown in Fig. 2.11.

At low power, the expected linear behaviour was observed, the light spreads among nearly all the 41 waveguides, and a pattern with two main lobes with secondary peaks between them is formed. From this pattern we conclude that the sample is about four coupling lengths long, as we match it to the distribution in Fig. 2.2. Increasing the power narrows the light distribution in Fig. 2.11.

Numerical simulations using the FEM method described in Sec. 2.4.1 verify that although light was coupled into a single waveguide, light is quickly distributed over a few waveguides in about one coupling length. From there on, the distributions remain confined, with only small width oscillations around the soliton value.

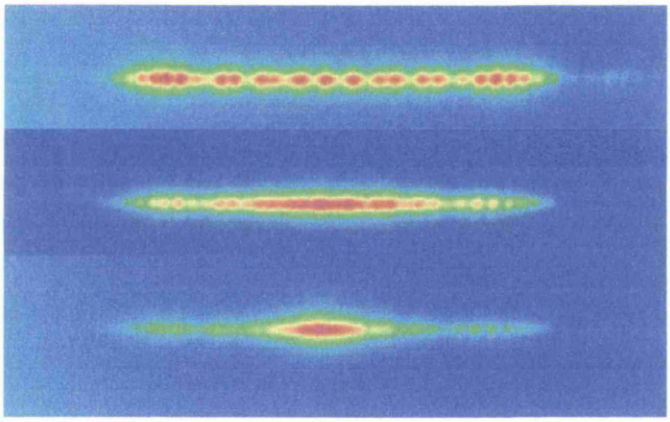

***Fig 2.11*** Generation of a discrete spatial soliton in a 41 waveguide array. At low power (TOP), discrete diffraction is present. When the energy is increased, the beam starts to narrow (MIDDLE) and finally a discrete soliton is formed (BOTTOM)

We also investigated 6 mm long samples with weaker coupling, where the waveguide separation was 5 μm and 7 μm. These samples were measured with TM and TE polarised light, respectively, at low and high powers. The respective high intensity peak powers were estimated to be 960 W and 870 W. The measured output patterns at low and high intensity are shown in Fig. 2.12. Also shown in the figures are numerical predictions for the intensity distribution among the waveguides, depicted as vertical lines in the figures.

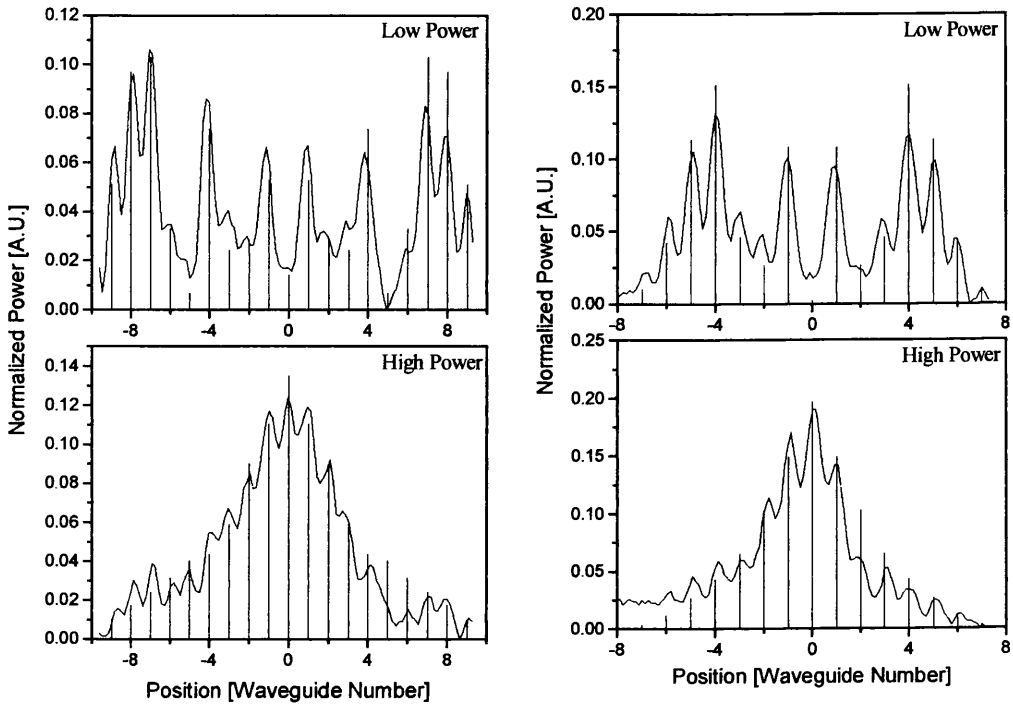


*Fig 2.12* Excellent agreement between experimental and theoretical data (represented by the straight lines) at low and high power (top and bottom of the graph, respectively). The samples were 3.0 (left) and 1.9 coupling lengths (right) long.

These simulations were performed by Hagai Eisenberg (Weizmann Institute of Science), using a fifth-order adaptive step size Runge-Kutta algorithm in order to integrate the DNLSE for the 41 waveguides (the height of the line represents the intensity in the corresponding waveguides). We note again the excellent agreement with the experimental data, in spite of a simplified approach with respect to the detailed coupled mode theory previously adopted. The linear parameters were obtained from the low power measurements. The non-linear coefficients were then adjusted to match the high power results.

We found that the sample lengths, in units of coupling length, were 3.0 and 1.9 for the D=5 μm and D=7μm samples, respectively. The parameter C is calculated to be 0.82 (0.52) $mm^{-1}$ for 5(7) μm separation sample. The value of $\gamma$ that best fits the high power results for 5 (7) μm sample for TM (TE) is 5.4 (6.2) $m^{-1}W^{-1}$.

The agreement between the experimental results and the theory is quite satisfactory, even though Eq. 2.2 assumes CW propagation, while the experiments were performed with a pulsed source. There are two sources of error: the intensity varies along the temporal profile, hence we expect the peak of the pulse to exhibit more confinement than its temporal wings. In addition, dispersion broadens the pulse by almost a factor of 2 as it propagates along the array, thereby reducing the peak power. These differences probably explain why the experimental field distributions are slightly broader than the CW theory prediction. They also explain the side wings emerging at high energy (Fig. 2.8).

One of the main challenges arising in the investigation of the properties of discrete solitons is the possibility to excite more waveguides simultaneously. We modelled and fabricated a device which allowed us to excite the three and five central waveguides with a quasi-gaussian envelope, using a star input junction as shown in Fig. 2.10. The advantage of this configuration over other solutions, like a short, strongly coupled injection array, or selective intermixing to reduce locally the non-linear refractive index $n_2$, is relatively easy fabrication and also a "linear" (power independent) characteristic. To verify that the properties of the junction were effectively the same at different power levels, we tested the junctions on their own.

We found a similar behaviour for the 5 waveguides junctions (b and c), which suggests that the linear losses in the bends are minimal. In the 3 star junction, the light was roughly distributed between the three central waveguides, while a quasi-gaussian distribution was achieved for junctions b) and c). However, in the latter case, only a small non-linear localisation was observed, as a result of two concomitant facts. First, a larger beam (or a larger discrete localisation, involving a few waveguides) diffracts slower and second, splitting the power between five or more waveguides significantly reduces the non-linear effects in the arrays. However, a significant non-linear localisation is present in the sample containing a three-star junction, although the sample was too short to develop a discrete soliton (Fig. 2.11).
In the second part of this chapter the experimental investigation of the novel steering properties of discrete spatial solitons will be discussed.

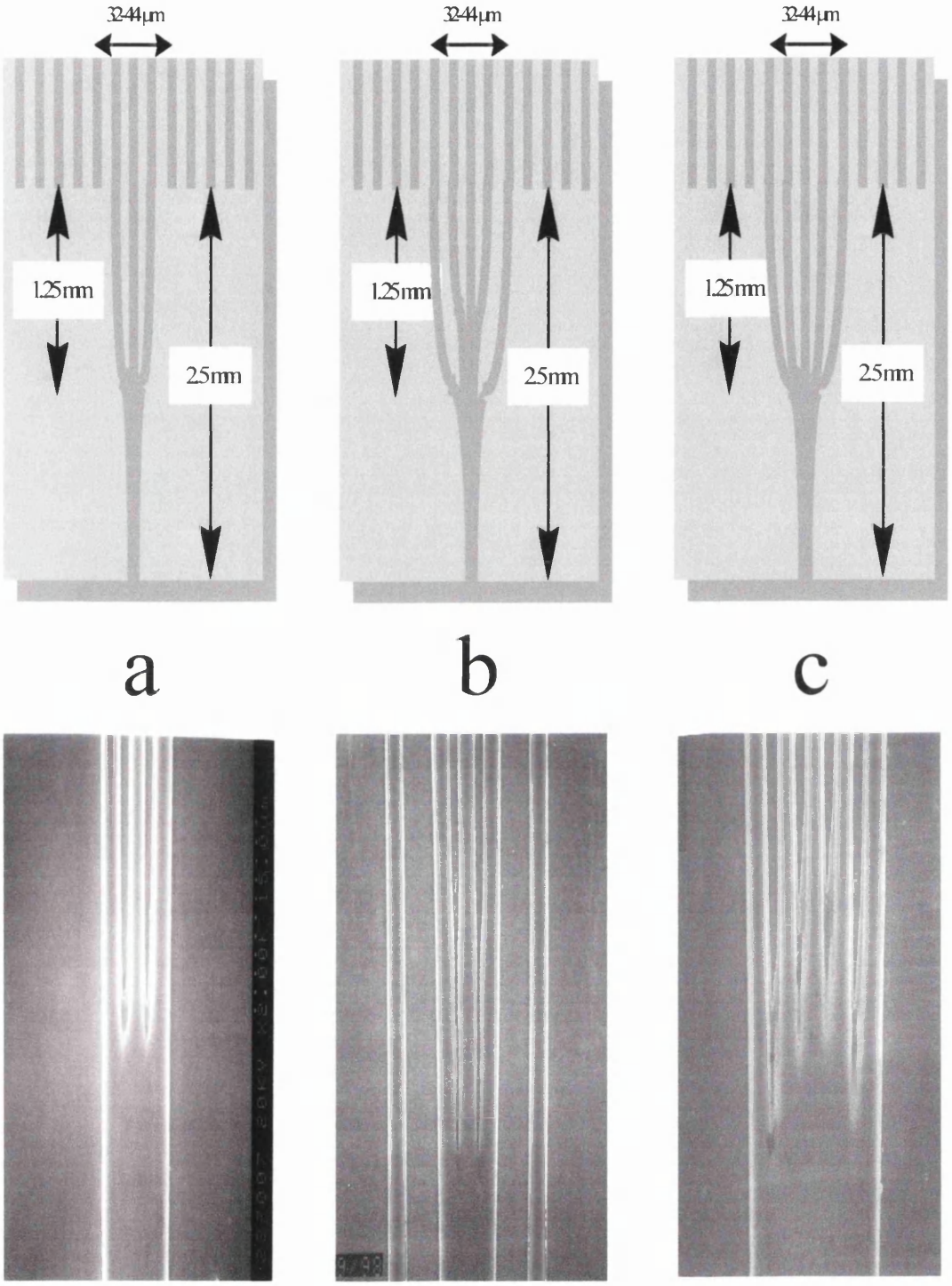


***Fig 2.13*** Can we excite 3 or 5 waveguides at the input of the array (the pictures below are SEM micrographs)?

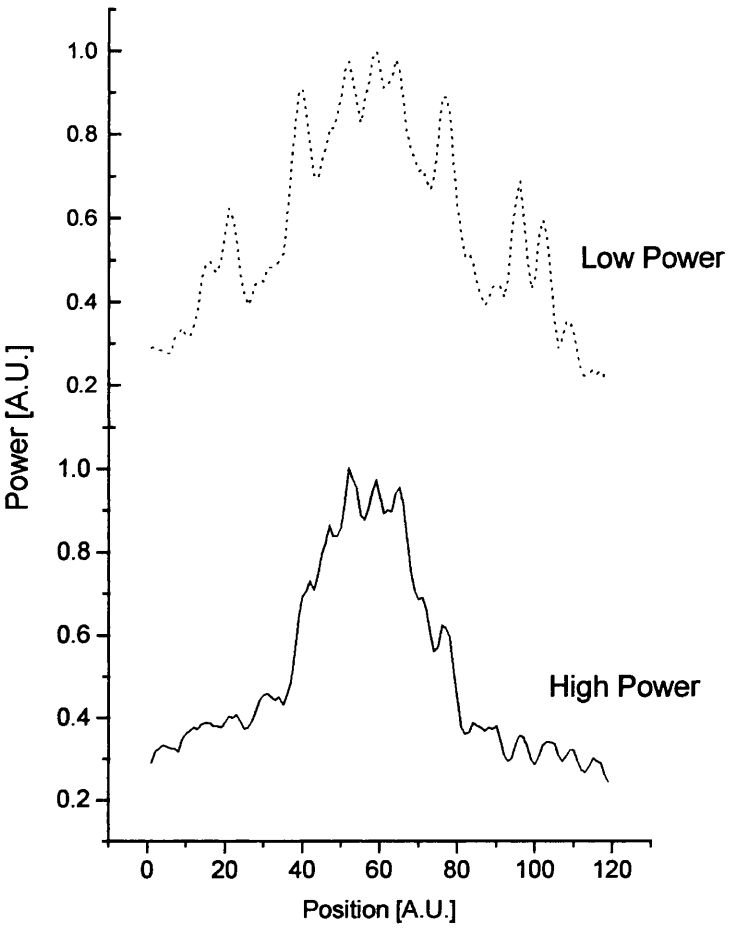


*Fig 2.14* Non-linear localisation in an array excited by a 3 star junction. The separation between each waveguide was 5 μm and the polarisation was TE.

## 2.6 Dynamics of Discrete Solitons in Optical Waveguide Arrays

The differences between continuous and discrete spatial solitons become obvious, if the soliton is forced to move across the array. Because there is no Galileian invariance as in the slab waveguide the discrete soliton prefers to stay localised on a certain waveguide [38].

[38] A. B. Aceves, C. de Angelis, T. Peschel, R. Muschall, F. Lederer, S. Trillo, and S. Wabnitz, Phys. Rev. E **53**, 1172 (1996)

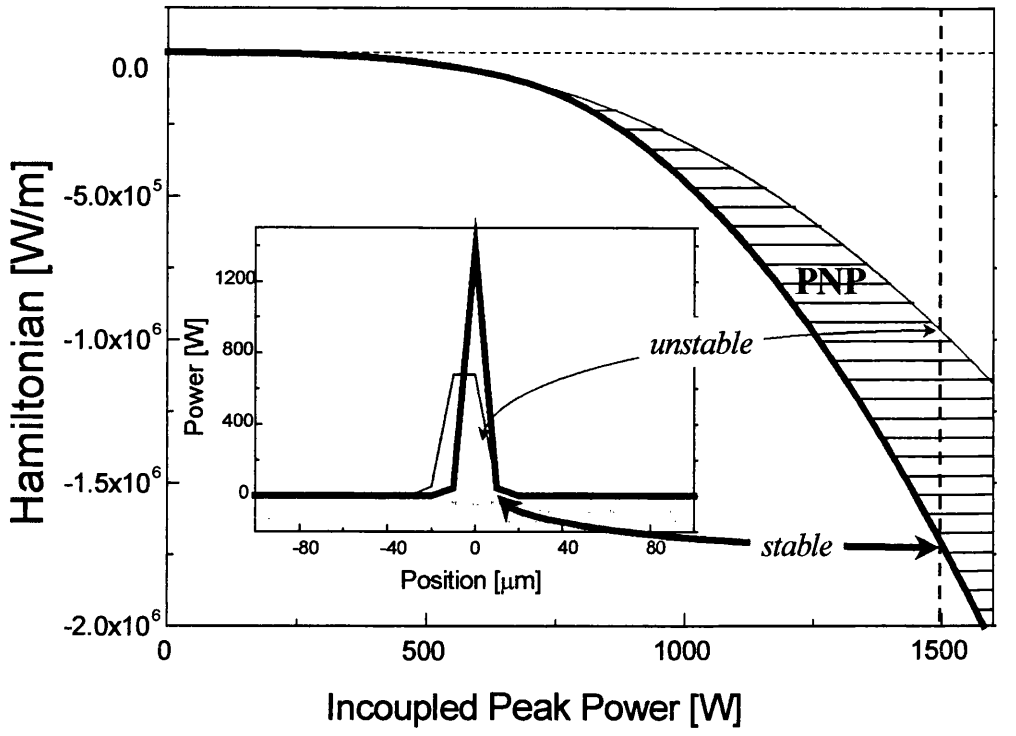


*Fig. 2.15* **Peierls-Nabarro-Potential**: Hamiltonian versus guided power for solitons centred on and in between two waveguides, inset: field shapes of the two types of solitons for a power of 1500W, dashed line: maximum incoupled peak power available in the experiment.

To observe this peculiar dynamical behaviour we mounted the sample on top of a piezo transducer to control the spatial position of the excitation. We note that, due to both the finite width of the incident beam ($W_{FWHM}$=9µm) and of the excited waveguide mode ($W_{FWHM}$=4µm) the effective width of the excitation is rather large (about 1.1 times the array period). Therefore, even if the excitation is not centred on a waveguide, the decrease in the coupling efficiency is less than 5%.

A general view on the physics can be obtained by first neglecting all absorption and transient effects. Under these idealised continuous wave (CW) conditions and by assuming that the array is infinite, the total power $P$ and the Hamiltonian $H$

$$P = \sum_n |E_n|^2 \qquad H = \sum_n C|E_n - E_{n-1}|^2 - \frac{\gamma}{2}|E_n|^4 \qquad 2.12$$

are conserved during propagation [38].

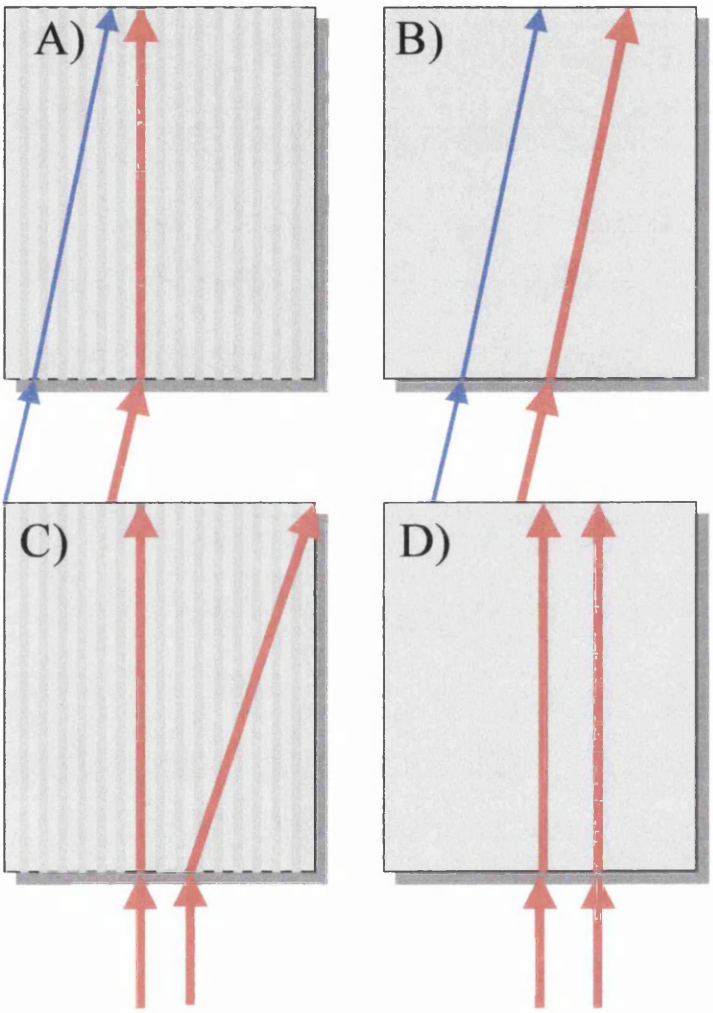


***Fig.2.16*** Differences between a discrete and a continuum system. In the first, a small phase tilt can be corrected by a suitable non-linearity (trapping of a moving soliton, A). This is not allowed for a soliton in a slab waveguide (B). In a discrete system is also possible to achieve a large steering by injecting a beam in between two waveguides, which will acquire an excess of kinetic energy due to the difference in the Hamiltonians between a stable and an unstable soliton (C). This behaviour is also not allowed in a slab waveguide.

[38] A. B. Aceves, C. de Angelis, T. Peschel, R. Muschall, F. Lederer, S. Trillo, and S. Wabnitz, Phys. Rev. E, **53**, 1172 (1996)

It should be noted that in quantum mechanical systems which are described by the same set of evolution equations both quantities have a different meaning. $P$ accounts for the norm of the wavefunction and $H$ denotes the energy containing the kinetic part $C|E_n-E_{n-1}|^2$.

Let us consider stationary solutions localised over a few waveguides. For each power level we find two solutions, one centred on a single waveguide and one centred in between two waveguides (see Fig. 2.15). Only the first case is stable and represents a minimum in the Hamiltonian. If a soliton is forced to move it has to jump from waveguide to waveguide, passing from a stable to an unstable configuration. The difference in Hamiltonians between the two cases - the so called Peierls-Nabarro-potential (PNP) - accounts for the resistance that the soliton has to overcome during propagation [51]. For increasing power levels the PNP increases (see Fig. 2.15) resulting in a stronger localisation of the soliton. As a consequence of the non-linearly induced index difference the excited waveguide is de-coupled from the rest of the array. As proposed recently this might be the basis of a power dependent steering[38]. In the corresponding continuous system - the slab waveguide -every phase gradient imposed onto the initial beam results in a corresponding tilt of the soliton motion[52]. A similar effect occurs in waveguide arrays[38], but the velocity of side ways motion is different and power dependent. In our experiment we used a very small tilt of ca 0.4 degree in the initial beam which corresponds to a phase difference of $0.08*\pi$ between adjacent waveguides. In the low power case we observed the field maximum to be shifted about 8 waveguides away from the central position. This corresponds to an overall distance of 72 μm. In a slab waveguide the same tilt would yield a shift in the output field distribution of only 14 μm. The enhanced sensitivity of the array with respect to initial phase tilts is mainly due to the different nature of discrete diffraction. When a single waveguide is excited, much

[51] Y. S. Kivshar, D. K. Campbell, Phys. Rev. E **48**, 3077 (1993)

[38] A. B. Aceves, C. de Angelis, T. Peschel, R. Muschall, F. Lederer, S. Trillo, and S. Wabnitz, Phys. Rev. E **53**, 1172 (1996)

[52] J. U. Kang, C. J. Hamilton, J. S. Aitchison, G. I. Stegeman, Appl. Phys. Lett. **70**, 1363 (1997)

more power is transferred to the wings of the field distribution compared with the continuous case. As the power is increased a soliton is formed which moves slower and slower and finally stays in the initial guide. This example is a simple and clear demonstration that Galileian invariance present in the continuous system disappears if the diameter of the excitation reaches the order of the waveguide spacing, where the discrete nature of the structure starts to play a role. This feature makes very efficient steering applications based on waveguide arrays possible.

While in the situation described above an initial sidewards motion is damped and finally suppressed completely with increasing soliton power, we are now going to demonstrate that discreteness not only prevents motion, but may also induce an acceleration of the soliton.

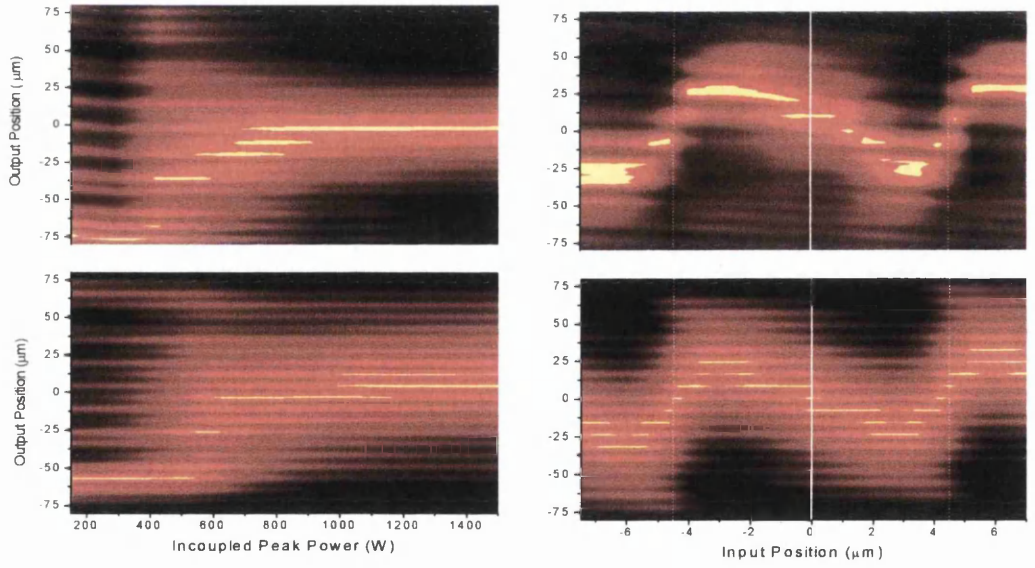


***Fig.2.17*** *Left*: Power dependent soliton steering by an externally induced velocity. Output field distribution as a function of applied power (initial tilt of the beam: ca 0.4 degree, experimental result -top-, and simulation -bottom-).

*Right:* Soliton steering by internally induced velocity. Output field distribution as a function of the input beam position, experimental result (top) and simulation (bottom). The solid line represents a beam centred on a waveguide, while the dashed line shows a beam centred between two waveguides.

For that purpose we make use of the fact that the initial beam is so large that the overall coupling efficiency is practically independent from the spatial position of the excitation. In the following experiment, we fixed the power, scanned 12 equidistant input positions between two neighbouring waveguides and recorded the resulting field pattern at the output facet (see Fig. 2.17, right). It turns out that only a very small change of the input beam position causes an output field displacement by several waveguides.

There is good agreement with the simulations based on Eq. 2.11 suggesting that this behaviour can still be understood using coupled mode theory. But first let us state some interesting facts:

1. In any case the beam width is much smaller than in the linear case and the amount of radiation emitted is negligible. Therefore, we may conclude that the beam always behaves like a soliton.
2. Because the displacement of the field at the output facet is up to ten times larger than the initial shift of the input beam the soliton must have gained a considerable velocity although no initial phase tilt was introduced.
3. For symmetry reasons the field must stay at its initial position if the excitation is either centred exactly on a waveguide (solid line in Fig. 2.17, right) or in between two waveguides (dashed line in Fig. 2.17, right).

In the latter case an unstable soliton is excited. In an experimental situation it is impossible to inject a beam exactly between the two guides. The resulting slight difference between the power levels of the two central waveguides causes a phase difference to evolve due to the action of the Kerr non-linearity. The corresponding phase tilt steers the power towards the high power waveguide while amplifying the initial deviation from the balanced state. Consequently the unstable soliton will evolve during such motion. In our experiment the instability is rather strong. For the peak power levels achieved, the growth rate of the unstable mode of the corresponding cw solution amounts to about 2.1 $mm^{-1}$.

As a consequence we see a rapid flipping of the output field while crossing the middle position with the incident beam. If we move further away from the centre the influence on the soliton dynamics becomes even bigger due to the fact that, in a first order approximation, the induced velocity of the soliton is proportional to the strength of the perturbation. Of course for larger deviations from the centre position this picture, which is based on a linear stability analysis, ceases to hold. In fact the shift of the output beam saturates and later decreases again. Finally, the excitation comes so close to a single waveguide that only a slightly perturbed stable soliton centred on a waveguide is excited, which almost stays at the initial position.

The main source of motion observed is the decay of the unstable soliton into a moving stable one, without emitting much radiation. The reason for this somehow unexpected behaviour resides again in the fact that the soliton has to preserve both its total power and its Hamiltonian.

The non-vanishing PNP prevents the soliton to settle down on the next neighbour waveguide, as its excess Hamiltonian is transferred into kinetic energy causing the soliton to move across the array. A similar mechanism does not exist in continuous systems because momentum conservation does not allow a resting solution to speed up.

From the point of view of applications the latter feature can be interpreted as a power dependent steering, where small power changes around an excitation between two initial waveguides can result in a large displacement of the output field distribution. This property may allow the use of a piezo transducer as a way of switching incoming signals between several output channels.

## 2.7 Non-linearly Induced Escape from Defect States in Waveguide Arrays

An interesting feature of discrete systems includes the possibility of introducing completely new effects. In particular, one can tune the sign of the dispersive effects

to allow a reversal of the effective action of the non-linearity, for example a contraction of the field for a defocusing non-linearity[53]. In what follows we are going to demonstrate that a positive, i.e. in the conventional notation a focusing, non-linearity may cause the field to spread.

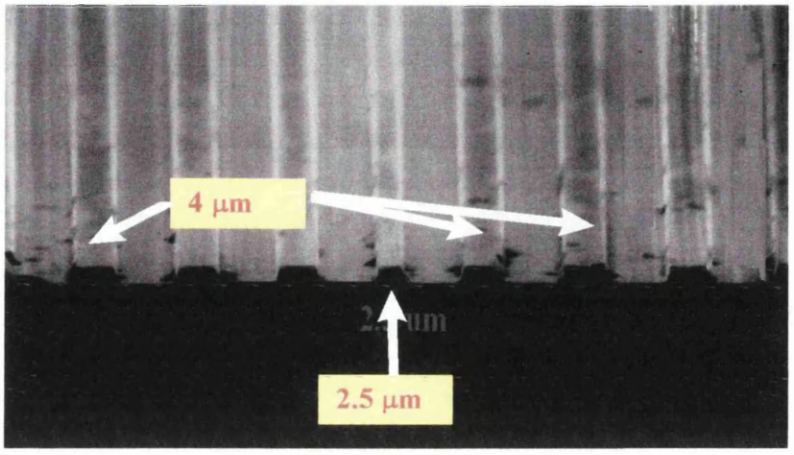


***Fig.2.18*** Micrograph of a non-uniform waveguide array.

In the case of inhomogenous arrays new effects come into play[54]. The optical field may be locally trapped in a single waveguide with a different propagation constant from the rest of the array. In contrast to conventional slab waveguides, guiding occurs on a defect in the array for both signs of the induced index change. Here we consider an array, in which the defect consists of a narrower waveguide with a lower effective index than the rest of the array. When an optical field is injected in such a defect, no phase matching occurs with the modes propagating in the nearest guides and the field is effectively trapped. However, as the intensity increases, the effective index of the confined mode grows due to the Kerr non-linearity and finally the field spreads out to neighbouring waveguides. In fact, the linear index differences in the array can be kept so low, that the non-linearity may compete with e.g. linear waveguiding allowing strong non-linear effects to be accessible.

---

[53] Y. S. Kivshar, Opt. Lett., **18**, 7 (1993).

[54] W. Krolikowski and Y. S. Kivshar, J. Opt. Soc. Am. B, **13,** 876 (1996).

The sample used in these experiments was a 3mm long array consisting of 41 rib waveguides with 5μm spacings. The central waveguide (n=0), which also represents the defect, was 2.5 μm wide, while the remaining 40 guides (n = -20, ...,-1, +1,..., +20) had a width of 4μm. This array was etched to 1.3 μm on top of the AlGaAs slab waveguide described in Sec. 2.5. To model the homogenous array ($S_n$=0) as well as the action of the defect ($S_n \neq 0$) we used coupled mode theory (Sec. 2.4.1) modifying Eq. 2.11 as[54]:

$$\left[ i\frac{\partial}{\partial z} - \frac{D}{2}\frac{\partial^2}{\partial t^2} + i\frac{\alpha_1}{2} + \gamma|E_n|^2 + i\alpha_3|E_n|^4 \right] E_n + C[E_{n+1} + E_{n-1}] + S_n = 0$$

$$S_n = \delta_{n,0}\left[\Delta k + \Delta\gamma|E_n|^2\right]a_n + \Delta C\left[(\delta_{n,0} + \delta_{n,1})E_{n-1} + (\delta_{n,0} + \delta_{n,-1})E_{n+1}\right] \qquad 2.13$$

The parameters reported in Sec. 2.4.1 were used, while the coupling constant used in Eq. 1 was about C=0.62 $mm^{-1}$.

The defect appears mainly as a reduction of the effective index of the corresponding guide ($\Delta k$=-1.5 * C). Note that the available peak power levels allow for an index increase which is about 6 times higher than this effective index difference. In addition, the effective non-linearity is slightly increased because of the reduced mode diameter ($\Delta\gamma$=0.2* $\gamma$). The coupling of the defect guide to its neighborhood appears to be stronger than in the homogenous array, because the corresponding guided mode is bound less to the defect guide ($\Delta C = 0.3 * C$ ).

Let us start with the experimental results for the low power case first (see Fig. 2.19 a)). Obviously there is a central field distribution and some minor radiation is shed to adjacent waveguides.

[54] W. Krolikowski and Y. S. Kivshar, J. Opt. Soc. Am. B, **13**, 876 (1996).

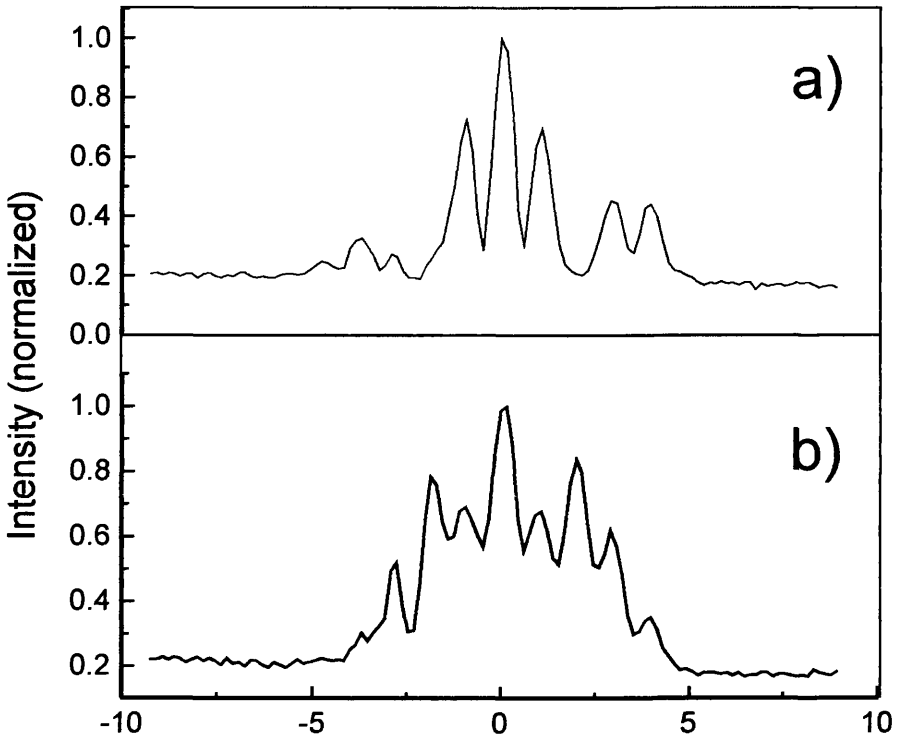


*Fig. 2.19* Experimental results - field profiles at the output facet for TE polarisation for an array with a defect at guide 0, a) low power, b) high power (1000W incoupled power)

A numerical comparison with the field propagation in an array without a defect reveals that a guided mode was excited (see Fig.2.20 a) and b)). For the parameters given above the defect is monomode. The shape of the guided mode is given by the following analytical expression:

$$a_n = \frac{1+\frac{\Delta C}{C}}{\xi^{|n|}} E_0 \exp(i\beta z), \qquad 2.14$$

where the transversal decay rate $\xi$ and the propagation constant $\beta$ are given by :

$$\beta = \left(\xi + \frac{1}{\xi}\right) C \qquad \text{and} \qquad \xi = \frac{\Delta k}{2C} - \sqrt{\left(\frac{\Delta k}{2C}\right)^2 + 2\left(1 + \frac{\Delta C}{C}\right)^2 - 1}\,.$$

Such solution was deduced by imposing a stationary propagation of the mode along the defect, toghether with the condition that its profile decays exponentially in the homogenous part of the array. As a result, $\xi$=-2.5 (see expression above on the right) and consequently the field amplitude decays while oscillating in phase. The $\pi$ phase jump between adjacent guides causes an inverted diffraction allowing for a bound state at a guide with reduced effective index. Although we could not detect the phase of the fields in the guides around the defect experimentally we find pronounced intensity dips between guide 0 and its neighbours, where the field of other guides futher away from the defect tend to merge (see Fig. 2.19 a)). This is a sign of destructive interference due to opposite phases of the field in the central guides. The oscillating field distribution of the guided mode makes a perfect excitation virtually impossible. Consequently radiation is shed away. The simulations reveal that the complete absence of power in the second waveguide (n=±2) is mainly a result of the destructive interference between guided and radiated power.

According to Eq. 2.13 the propagation constant of the guided mode ($\beta$=-2.9*C) is below the continuous spectrum of the array extending from -2C to +2C. Therefore, the non-linearity will increase the propagation constant until it is phase matched with the continuous spectrum and the optical field is released from the defect state.

In fact we observe a considerable broadening of the field distribution for increased power levels (see Fig. 2.19 b). In particular, the transmission of the second guide has increased enormously. Further, the deep dips between the field profiles of the individual guides observed in the low power case disappear indicating that the strict anti-phase relation of the guided mode has vanished.

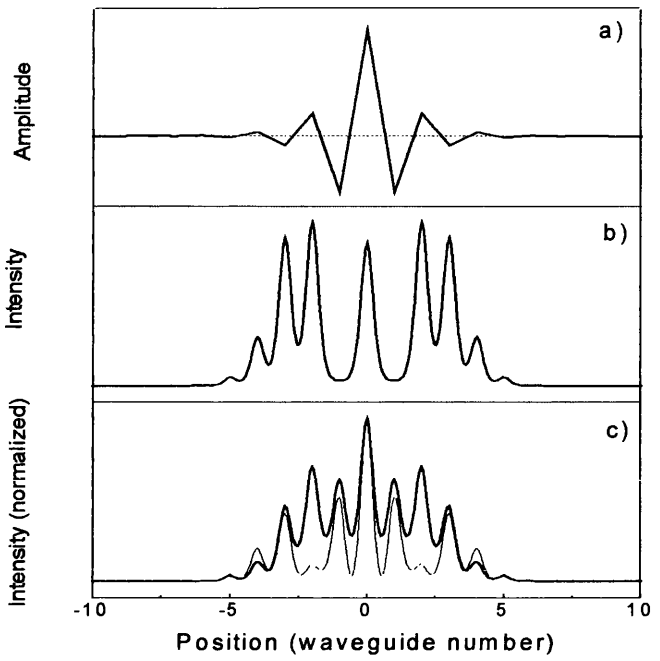


*Fig. 2.20* Numerical simulations, a) amplitude distribution of the guided mode, b) low power field distribution at the output facet of an array without a defect, c) low (thin line) and high power (1000 W, bold line) field profiles for an array with a defect at guide 0.

All these features can be understood in terms of coupled mode theory as revealed by the good agreement between experimental results and simulations (compare Fig. 2.19 and Fig. 2.20 c). There is still a maximum pulse energy concentrated at the defect due to two effects: first we always observe a time average over all power levels in the pulse. The predicted escape from the defect state appears in the pulse centre but the experimental results account for the low power parts of the pulse as well. Second, even a complete neutralisation of the defect would not result in an abrupt spreading of the field. Just as in case of a homogenous array (see Fig. 2.20 b)) a significant amount of power would have remained in the centre waveguide. Numerical simulations, which are not restricted to a finite sample length, show that although in our experimental situation the field just started to spread, considerably more

propagation distance would have been required to allow for a complete escape.
In the last experiment, we observed a bound state in a waveguide array localised on a guide with reduced effective index. We designed the array in such a way that the optical non-linearity may compete with the linear guiding mechanism, allowing for strongly non-linear effects. We demonstrate that considerable portions of the guided power can escape from the defect state due to the action of the non-linearity. We found a power-dependent high contrast switching in one of the waveguides, which could be the basis for a highly efficient saturable absorber. This is a remarkable achievement in a real device, which presents both dispersion as well as linear and non-linear losses.

## 2.8 Conclusions

In conclusion, we have studied and demonstrated, for the first time, the formation of discrete spatial solitons in non-linear waveguide arrays made of AlGaAs, operating at photon energies below the half band gap.

We have shown a power dependent localisation in such a system, whose dynamical properties differ from those of a continuous system considerably.
We have experimentally demonstrated that initially moving solitons can be finally captured by the initial waveguide if a certain power level is reached.

On the contrary the decay of unstable solitons centred between two waveguides may result in a considerable sidewards motion across the array. We found that the original displacements of the input beam can be amplified at the output facet up to a factor of ten. All these dynamical properties are very much power-dependent and may therefore be employed for all-optical switching and routing applications.

Subsequently, we investigated the optical properties of non-uniform waveguide arrays, where defects are intentionally introduced by modifying the linear coupling coefficient of selected waveguides. This is achieved either by varying the distance

between the single waveguides or by changing the linear index difference, e.g. the width of one or more waveguides.
Changes, either in the effective index of individual waveguides and / or the coupling between neighbouring guides may result in a bound state of linear waves.
It can also be possible, with a proper design, to revert the linear action with an appropriate non-linearity and consequently induce an escape of the confined state from the defect.

Our work was stimulated by the great amount of interest in non-linear discrete systems raised in the last few years. This is due to the fact that matter itself is discrete, i.e. it consists of many single elementary units. When the spatial scale of the excitation approaches the size of its individual constituents, a continuous approach fails to give an accurate picture and the discrete nature of the system must be taken into account. Recent theoretical efforts have been directed to the investigation of the properties of vectorial modes in non-linear waveguide arrays[55] and to the study of novel array configurations[56,57].

[55] S. Darmanyan, A. Kobyakov, E. Shmidt, and F. Lederer, Phys. Rew. E, **57**, 3520 (1998)

[56] U. Peschel, T. Pertsch, and F. Lederer , Opt. Lett., **23**, 1701 (1998)

[57] A. Komiyama, Opt. Comm., **151**, 25 (1998)

# Chapter 3

# *Intermixing as a way of Tailoring the Non-linear Optical Coefficients*

Non-resonant non-linearities in AlGaAs, at half the bandgap, have been proposed as a mechanism for realising all optical switches, modulators, and for the generation of optical solitons. However, to fully realise the potential of such non-linear devices, it is necessary to integrate them with passive linear waveguides and ideally with high power semiconductor lasers. Recently, disordering of Multiple Quantum Well (MQW) structures has been used to produce a range of integrated devices[58,59] and has been suggested as a possible technique for integrating linear and non-linear devices onto the same chip.[60]

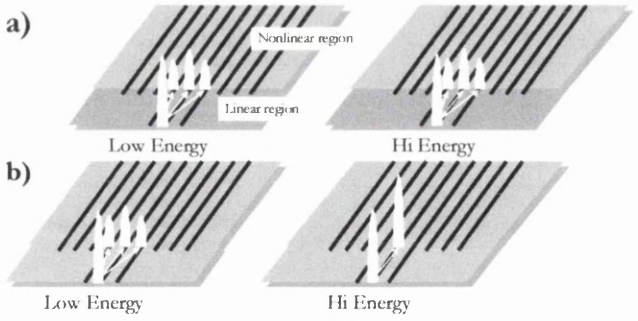


***Fig. 3.1*** MQW Intermixing as a way to fabricate regions with different non-linearities. In principle, intermixing suppresses the non-linear effects, and no switching is observed in the input Three-core Coupler (part a) of the figure).* In a normal wafer (part b)) switching occurs at the input for high energy, hence is not possible to excite 3 waveguides contemporaneously.

---

[58] D. G. Deppe and N. Holonyak, Jr., J. Appl. Phys, **64**, R93 (1988)

[59] B. S. Ooi, K. McIlvaney, M. W. Street, A. S. Helmy, S. G. Ayling, A. C. Bryce, J. H. Marsh, J. S. Roberts, IEEE J. Quant. Electron., **33**, 1784 (1997)

[60] P. Dumais, A. Villeneuve, A. S. Helmy, C. J. Hamilton, J. S. Aitchison, *"Soliton Emission from an AlGaAs Waveguide"*, Conference on Quantum Electronics and Laser Science (QELS), Technical Digest series, **12**, 166 (1997)

* Multi Core Couplers are discussed in Sec. 2.1

The possibility of fabricating regions with low non-linearities was considered an attractive way to excite several waveguides with a power independent characteristic (Fig 3.1). In theory, we thought to use this scheme by intermixing the initial part of an AlGaAs MQW chip. In practice, we found such an approach quite complex and scarcely effective, mainly because of the higher linear losses generated by this process. First, we will review briefly the main features of MQW heterostructure and then describe the different steps carried out to perform the experiments.

## 3.1 Comparison between Bulk AlGaAs and MQW Heterostructure

In Chapter 1 we showed that AlGaAs is an attractive optical material for several reasons (Sec. 1.5). However, the non-linear optical properties of this material can be further improved in order to achieve monolithic integration. The MQW samples used in this work were produced by sandwiching a thin layer of AlGaAs (Well) with a low Al content (i.e. a narrower band gap) between two relatively thick layers of AlGaAs (Barriers). If the well is thin enough and the lattice constants are well matched, the band discontinuity at the junctions will be sharp enough for the well to be modelled by a finite square well. Quantum wells allow electrons and holes to move freely in the plane of the well, but constrain movement normal to the well. This confinement gives rise both to quantised energy levels and hole electron bound states which are referred to as "excitons". Introducing the exciton binding energy B (between 10 and 20 meV), the absorption energy required to generate a exciton pair, $E_{cc}(n)$, can be written as:

$$E_{cc}(n) = E_g + \varepsilon_n^e + \varepsilon_n^{hh,lh} - B \quad (n=0, 1, ...) \qquad 3.1$$

where $\varepsilon_n^e$ and $\varepsilon_n^{hh,lh}$ are the discrete levels obtained by solving the square well for electrons, heavy holes and light holes respectively[61]. Recent theory has used a Kane

[61] C. Weisbuch and B. Winter "*Quantum Semiconductor Structures*", Academic Press, New York, USA (1991)

band-structure model based on a seven levels description[62] to determinate the ultra-fast non-linear refraction ($n_2$) of semiconductors. The magnitude of the real part of $\chi^{(3)}$ was shown to be inversely proportional to $E_g^4$. This relationship is also reflected in the value of $n_2$, which consequently is different in the case of a bulk and a MQW structure. This fact is extremely important because control over the band gap can be achieved by using MQW structures and disordering techniques. More precisely, MQW structures can be disordered to induce a blue shift through the reshaping of the band edge. The disordered structure acquires hybrid properties between the bulk material and the original structure.

A number of different techniques can be used to intermix GaAs based systems. In general, disordering occurs through the interdiffusion of various elements of the semiconductor crystal matrix.

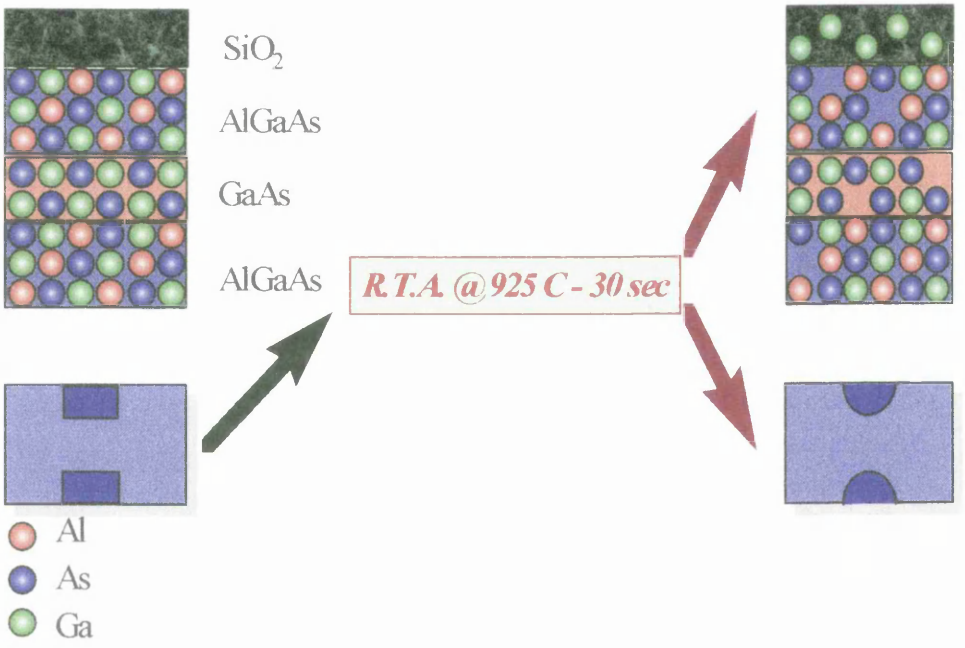


***Fig. 3.2*** Schematic diagram of an intermixing process using IFVD techniques.

[62] D. C. Hutchings and B. S. Wherret, Phys. Rev. B., **52**, 8150 (1995)

This process relies on the existence of native crystal defects, through which the matrix elements can move.

The samples used in this project were annealed using Impurity Free Vacancy Diffusion (IFVD) where Rapid Thermal Annealing (RTA) was used to promote intermixing through the diffusion of induced surface vacancies (Fig 3.2).

## 3.2 Design of the MQW Waveguide Structure

In designing a MQW structure suitable for non-linear experiments, we focused on the following four aspects:

1) The waveguide must have a fundamental bandgap below 750 nm, in order to minimise TPA for wavelengths longer than 1.5 μm and maximise the effectiveness of the non-linearity.

2) Disordered waveguides must possess a reasonable shift (a few percent) from the fundamental band gap, if a significant change in non-linearity is required.

3) Waveguides must be low loss and provide strong light confinement, to ensure observation of non-linear effects.

4) The wafer must be easily grown and possibly the influence of growth errors (e.g. local changes in barrier and well thickness) on the physical properties of the structure should be minimised.

Keeping this in mind, two different configurations were modelled. Both were single mode slab waveguides, in order to maintain high optical intensities over long interaction distances and also to reduce the variables present in the non-linear experiments.

The two designs differed in the geometry of the multiple quantum well structure.

Simulations have shown that growth errors can be reduced by increasing the thickness of the wells (Fig. 3.3), which must contain Al in order to have a fundamental band gap below 750 nm. However, this design proved to be somewhat difficult to grow, since it required two independent aluminium fractions for both the quantum well and the barriers. In Fig 3.4 we show a picture of an MBE grown AlGaAs/AlGaAs wafer taken with a high resolution scanning electronic microscope (SEM 900).

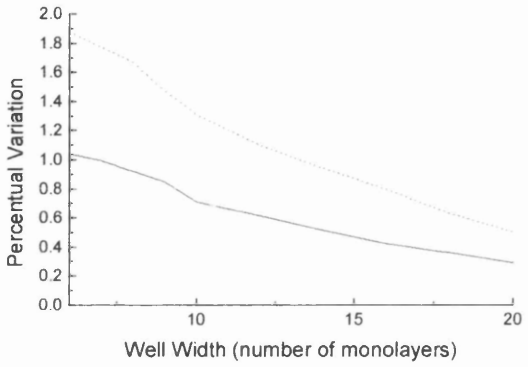


***Fig. 3.3*** Effect of variations in the width of the well on the fundamental band edge for a MQW heterostructure. Numerical simulation for the case of one monolayer (continuous line) and two monolayers (dotted line) are reported.

The sample, consisting of a waveguide 2 mm long, was previously exposed to a selective wet etch solution (5% Ammonia and 95 % Peroxide) for an average time of 5 mins.

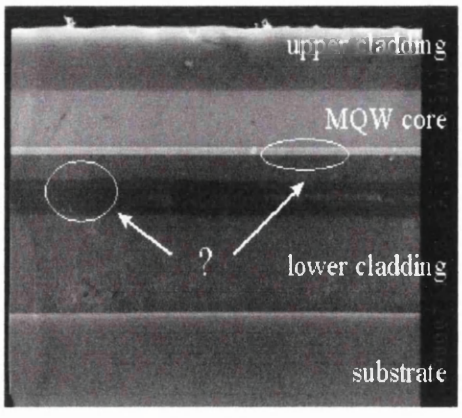


***Fig. 3.4*** SEM picture of an AlGaAs/AlGaAs MQW waveguide. Selective etching reveals a degree of non-uniformity in the layer compositions.

This solution interacts more slowly with layers containing higher percentages of aluminium (more precisely, at 0 C° bulk GaAs is etched at a rate of 1 μm/min, 100 times faster than a typical AlGaAs alloy), creating a three-dimensional profile which can be resolved by an electronic microscope. Though it was not possible to identify each of the MQW layers in the core, it is clear that the composition of the lower cladding is not uniform, resulting in poor optical properties.

For this reason, the alternative design was preferred. It used a GaAs quantum well sandwiched between $Al_{0.40}$ $Ga_{0.60}$ As barriers. The 40% aluminium ensured that the material had still a direct band gap, but since GaAs was used in the wells, it was necessary to make the wells relatively thin (<3 nm) to ensure that the band gap was below 750 nm. The sample was grown by the EPSRC MOVPE Facility at Sheffield University.

### 3.3 Fabrication of the Waveguides

Two different sets of samples were prepared. In the first group, strip loaded guides were etched to 0.7 μm into the upper cladding using a combination of standard photo-lithography and reactive ion etching. In the second group, the same operation was preceded by processing of the sample using Impurity-Free Vacancy Disordering (IFVD).

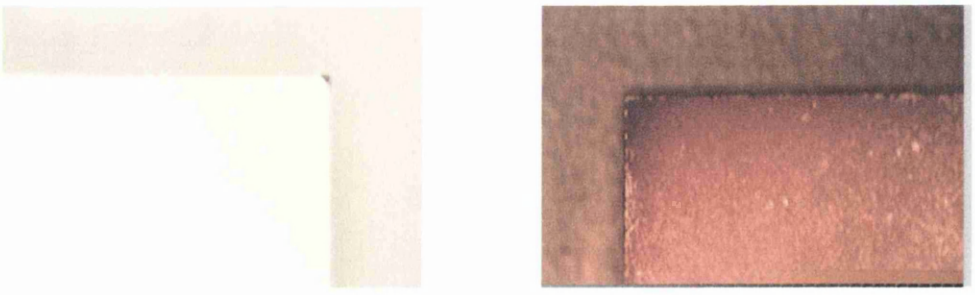

*Fig. 3.5* Morphology for two samples intermixed at 925 C° (left) and at 960 C° (right). We observe how, in the latter case, the quality is strongly deteriorated due to the many defects present over the surface.

To achieve intermixing, a 200 nm capping layer of $SiO_2$ was initially deposited across the whole sample using plasma-enhanced chemical-vapour deposition (PECVD), and then the sample was thermally processed in a Rapid Thermal Annealer (RTA). A good compromise between the morphology of surfaces and significant band gap shifts was achieved placing the sample face down on a piece of fresh GaAs whilst another piece of GaAs was placed over the back to provide an As over pressure during annealing. The sample was subsequently heated within 10 s to a temperature of 925 C°, which was then held for 30 s. The whole operation was performed under an atmosphere of $N_2$ in order to prevent contamination. The high temperature preferential absorption of Ga atoms into a $SiO_2$ cap results in a production of surface vacancies which tend to migrate into the MQW core to promote intermixing. Subsequently, the sample was wet etched with buffered HF to remove the $SiO_2$ cap.

Low temperature PL (77 K°) based on the 514.5 nm line of an argon-ion laser was used to study the fundamental (e-hh) exciton transition and hence to characterise the band gap shifts in the MQW core (Fig. 3.6). To get information about the exact position of the band edge, it was also necessary to record the room temperature absorption spectrum.

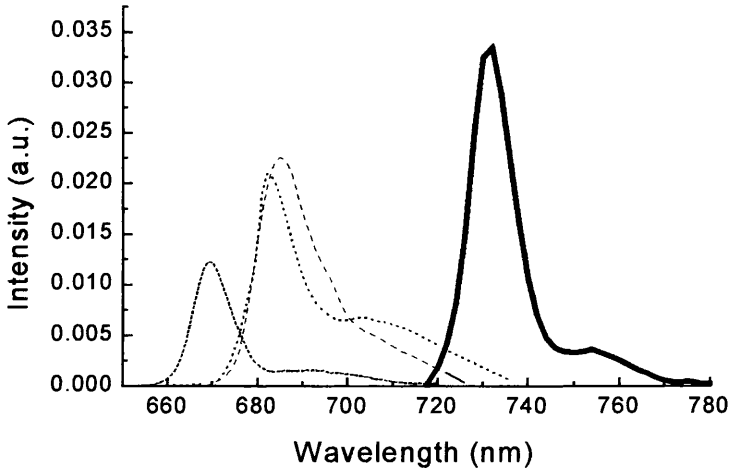


*Fig. 3.6* Photoluminescence transitions of intermixed samples, for 3 different annealing temperatures, are compared. We have, from right to left, the following spectra: as grown, intermixed at 925 °C, intermixed at 940 °C and intermixed at 960 °C.

However, when such measurement is performed in a transmission regime, it is necessary to remove the GaAs substrate, a process which is both time consuming and destructive. We firstly thinned the sample to a thickness of approximately 150 μm before mounting side down on a clean glass microscope using an index matching glue. The GaAs/AlGaAs selective etching described in this section was used to remove the remaining portion of substrate.

To ensure that the process was complete, the chip was examined under a microscope while illuminated with a white source from below. When the substrate was totally removed, it was possible to observe red light transmitted by the sample.

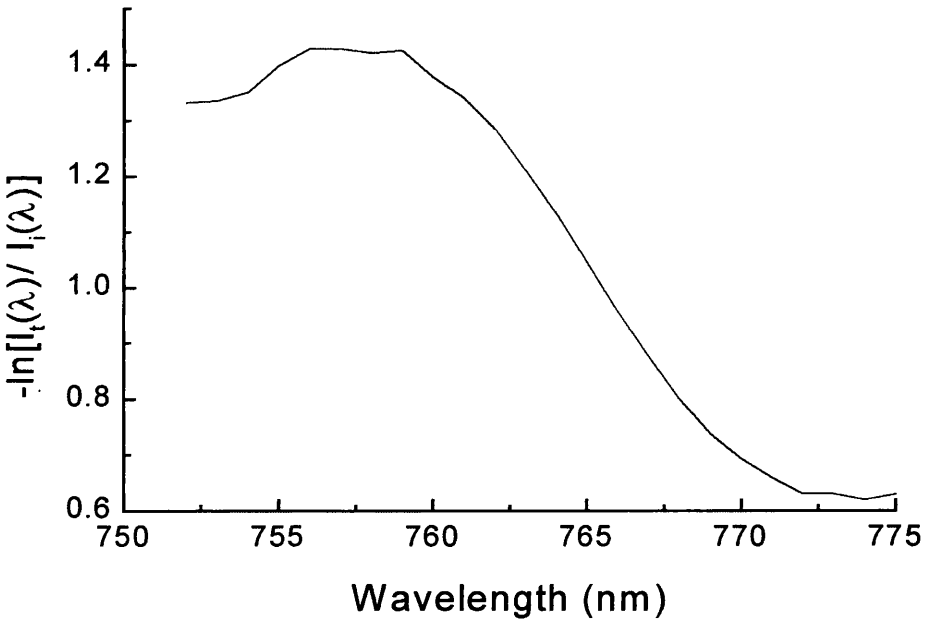


*Fig. 3.7* Transmission spectrum as recorded in a MQW sample.

To determinate the transmission spectrum, $I_t(\lambda)$, white light was focused onto the entrance slit of a monochromator, to generate a continuous range of wavelengths[63]. The light scanned from the monochromator was focused into the sample to monitor the intensity transmitted as a function of wavelength. Subsequently, the sample was removed and the spectrum of the white light source, $I_i(\lambda)$, was recorded over the

removed and the spectrum of the white light source, $I_i(\lambda)$, was recorded over the same wavelength range, but with the sample removed. The normalised transmission spectrum can then be expressed by the quantity

$$T = -\ln[I_t(\lambda)/I_i(\lambda)], \qquad 3.2$$

as a function of the wavelength $(\lambda)$ (Fig.3.7). Simulations (based on a code developed by C. J. Hamilton at University of Glasgow) have shown that the fundamental light hole and heavy hole transitions should occur at a wavelength of 746.8 nm and 762.3 nm respectively. However, such fundamental excitons could not be resolved, probably due to a poor quality of the wafer. After the strip-loaded waveguides were fabricated, both set of samples were cleaved to a length of 6 mm and the linear losses were measured using a standard Fabry-Perot technique[49] performed with a narrow line 1.55 μm DFB laser. The resulting waveguides had an average loss of 5 and 7 dB for the undisordered and disordered material respectively, which resembles the values recently obtained in similar MQW MOVPE samples[60]. This value can be compared with a similar structure grown by molecular beam epitaxy (MBE) at University of Glasgow [64]. The quality of an MBE sample is generally higher with respect to a MOVPE grown material: losses equal to 1 dB/cm were reported in a sample "as grown". Waveguides with selective non-linearities were subsequently intermixed using hydrogen plasma processing,[65] a technique which enables local suppression of band gap shifts in GaAs/AlGaAs MQWs. After intermixing, the losses in this MBE material increased to 3 dB/cm and 6 dB/cm in the undisordered and disordered section of the sample, respectively.

---

[48] See, for example, P. Millar, *"Non-linear Propagation Effects in Periodic Microstructures"*, PhD Thesis, University of Glasgow, Glasgow, UK (1997)

[59] B. S. Ooi, K. McIlvaney, M. W. Street, A. S. Helmy, S. G. Ayling, A. C. Bryce, J. H .Marsh, J. S. Roberts, IEEE J. Quant. Electr., **33**, 1784 (1997)

[64] C. J. Hamilton, J. H. Marsh, D. C. Hutchings, J. S. Aitchison, G. T. Kennedy, W. Sibbett, Appl. Phys. Lett., **68**, 3078 (1996)

[65] C. J. Hamilton, S. E. Hicks, B. Vogele, J. H. Marsh, J. S. Aitchison, Elec. Lett., **16**, 1393 (1996)

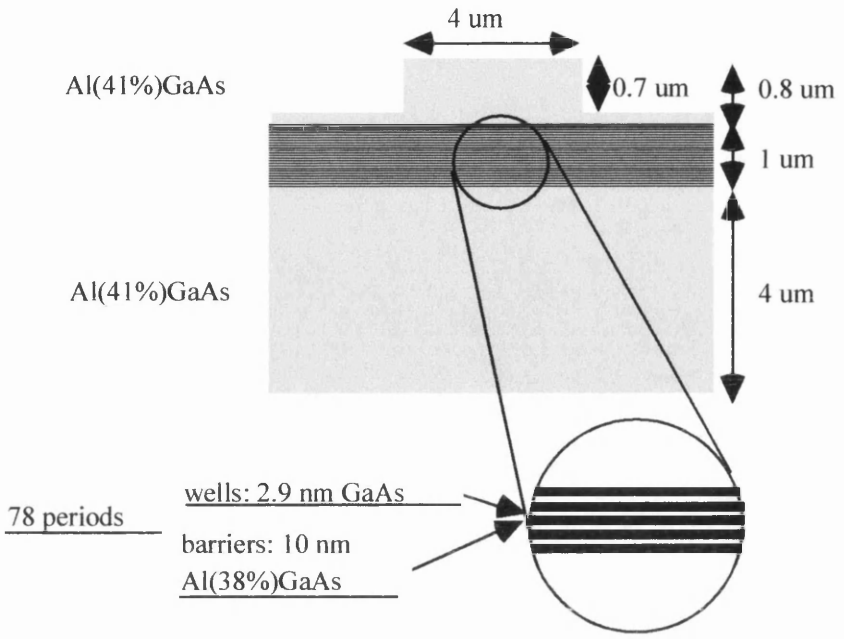


***Fig. 3.8*** The MQW waveguide structure.

## 3.4 Experimental Results

It has been recently proposed[66] that, near the half band gap, the non-linear properties of MQW are mainly due to the two-photon (TPA) resonances, and different selection rules apply to optical transitions associated with TE and TM modes. This approach suggests that, when a TE polarisation is applied, the TPA results in a final 2P-exciton state which is largely broadened and difficult to observe. For a TM mode clear resonance peaks for the 1S-exciton final state have been predicted and experimentally demonstrated[67] in a high quality sample. However, the observation of exciton features is generally quite difficult at room temperature, nevertheless different values are measured for different polarisations. An alternative approach suggests that the anisotropy of the main non-linear properties of MQW structures, such as non-linear refractive index ($n_2$), two and three photon absorption and Ratio A between cross and self- phase modulation is mainly due to the presence

[66] A. Obeidat and J. Khurgin, J. Opt. Soc. Am. B, **12**, 1222, (1995)

[67] J. U. Kang, J. Khurgin, C. C. Yang, H. H. Lin, G. I.Stegeman, European Quantum Electronics Conference, Technical Digest, 241 (1998)

of higher conduction bands, which induce anisotropy through an "allowed-forbidden" transition scheme. [68] (Fig. 3.9)

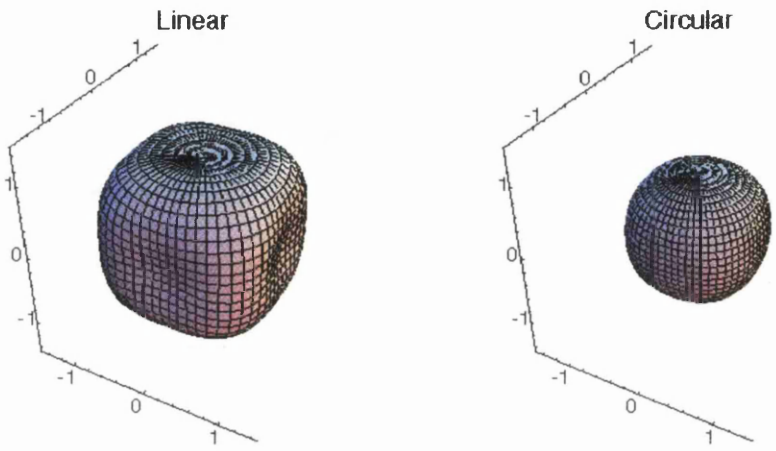


*Fig. 3.9* Typical anisotropy of $n_2$ and TPA coefficients of GaAs: for linear and circular polarised light. The origin of the polarisation vector is at the centre of the figure. The axes correspond to the crystallographic-axis directions.

*3.4.1* **Determination of the TPA Coefficient.** The differential equation which describes the change in the intensity, $I$, as a function of propagation distance z through a sample with one- and two-photon absorption occurring can be written as:

$$\frac{dI}{dz} = -\alpha_0 I - \alpha_2 I^2 \quad , \qquad 3.2$$

Where $\alpha_0$ and $\alpha_2$ are the linear loss (expressed in $cm^{-1}$) and the two-photon absorption coefficients (expressed in cm/W), respectively. This equation can be solved analytically, and expressed in terms of the inverse transmission as[11]:

[68] D. C. Hutchings and B. S. Wherret, Phys. Rev. B, **49**, 2418 (1994)

$$\frac{1}{T} = \frac{I_{in}}{I_{out}} = \frac{1}{(1-R)^2 \eta e^{-\alpha_0 L}} + \alpha_2 \frac{\left(1-e^{-\alpha_0 L}\right)}{\alpha_0 (1-R) e^{-\alpha_0 L}} I_{in} \qquad 3.3$$

In the expressions above, $I_{in}$ and $I_{out}$ are the input and output intensities, respectively, $R$ is the portion of light reflected at the interface (30% in our case), $\eta$ is the coupling efficiency. Thus, for the two-photon process, the inverse transmission as a function of input intensity is linear and the slope of the line is directly proportional to the two-photon absorption coefficient. Additionally, the intercept with the y-axis is related to the linear loss of the waveguide (Fig. 3.10). The equation above is strictly valid for energy above half the band gap, where the contribution due to 3 Photon absorption is negligible. At longer wavelengths Eq. 3.3 is no longer appropriate as the different contributions must be separated.

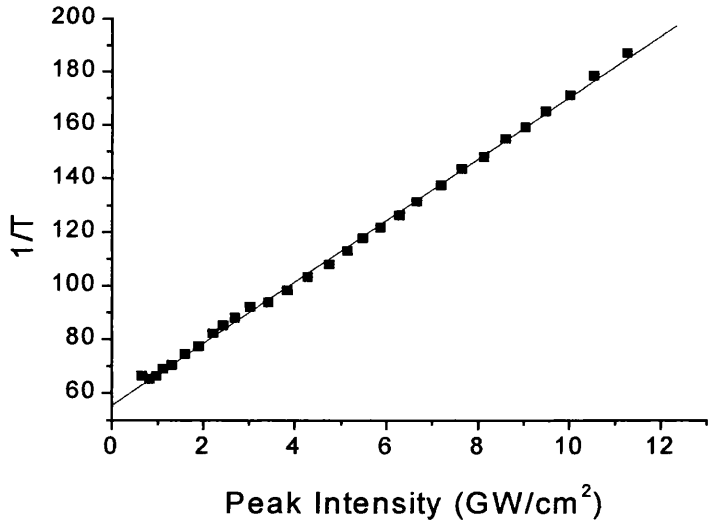


***Fig. 3.10*** Typical plot of the inverse transmission as a function of the input intensity.

[11] J. S. Aitchison, D. C. Hutchings, J. U. Kang, G. I. Stegeman, and A. Villeneuve, IEEE J. Quant. Electron., **33**, 341 (1997)

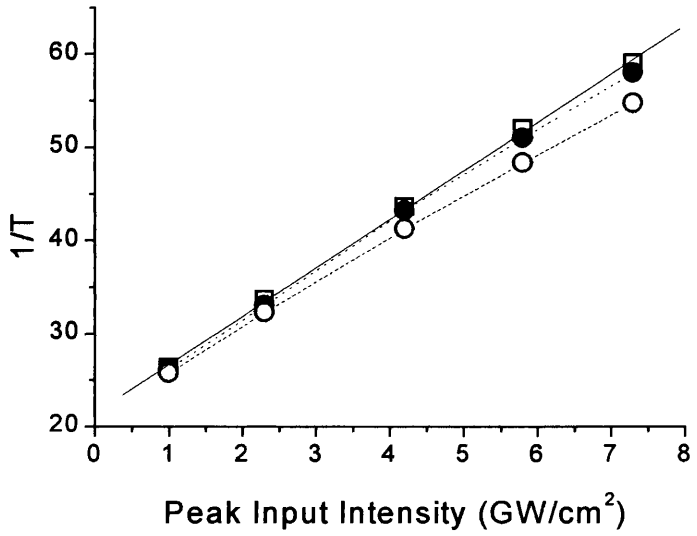


*Fig. 3.11* Effect of Two photon absorption, dispersion and self phase modulation on the transmission of a pulse with a sech-like shape in AlGaAs at the half band gap. Typical values of the inverse transmission as a function of the input power are shown in a CW regime (empty squares), and for pulses 200 fs and 100 fs long (solid and empty circles, respectively).

Numerical simulations employing a Fast-Fourier Transform Beam Propagation code[14], (adapted from a program written by D. Hutchings at University of Glasgow) were also used to fit the experimental data and to refine the results previously obtained. In particular, as sub picosecond pulses were employed, it was necessary to correct for the effect of chromatic dispersion. Very short pulses tend to broaden quickly with a sharp decrease of the intensity occuring along the temporal profile, hence reducing the non-linear pulse. The effect of dispersion and self-phase modulation on the transmission have been evaluated for two different configurations (Fig. 3.11).

As previously stated, the experimental anisotropy in the two photon absorption with respect to the two orthogonal TE and TM polarisations can be described in zinc-blende semiconductors (e.g. bulk AlGaAs) by including higher conduction bands. The resulting state mixing (e. g. due to the $k \cdot p$ perturbation) generates

[14] G. P. Agrawal, *"Nonlinear fiber optics"*, Academic Press, New York, USA (1995)

some non-zero off-diagonal elements, to which non-linear refraction and two-photon absorption are related[9].

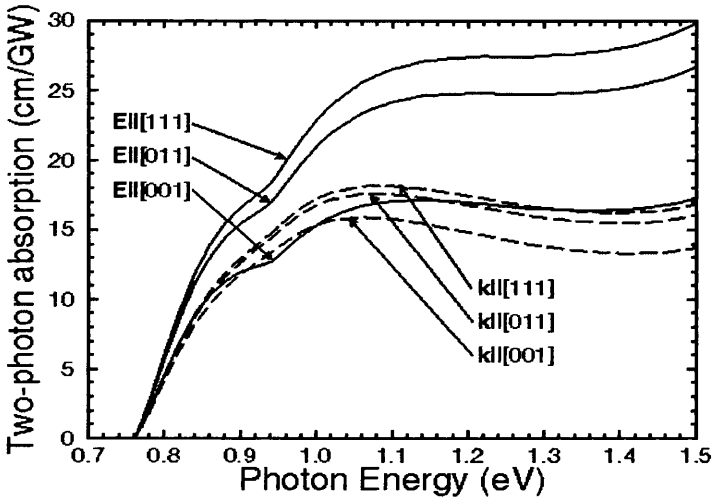


*Fig. 3.12* The spectra of two-photon-absorption coefficients of GaAs, demonstrating both anisotropy and linear-circular dichroism.

The spectra of two-photon absorption calculated using the seven band model are shown in Fig. 3.12. However, if we neglect the anisotropy between different polarisation components, we can use a simple model based on scaling laws to describe the two-photon absorption[69] below the half band:

$$\alpha_2(\omega)=\frac{2^9\pi e^4\sqrt{E_p}}{5\sqrt{m_0c^2}n_0^2E_g^3}\frac{\left(2\frac{\hbar\omega}{E_g}-1\right)^{\frac{3}{2}}}{\left(2\frac{\hbar\omega}{E_g}\right)^5}=C\frac{\left(2\frac{\hbar\omega}{E_g}-1\right)^{\frac{3}{2}}}{\left(2\frac{\hbar\omega}{E_g}\right)^5} \qquad 3.4$$

Here $E_g$ is the band gap energy, $E_p$ is the Kane energy (25.7 eV for GaAs), $m_0$ is the free electron mass, and $e$ is the charge of the electron. Due to the limitations of this approach, $C$ is not an exact value but rather an indication of

[9] P. N. Butcher and D. Cotter, *"The Elements of Nonlinear Optics"*, Cambridge Studies in Modern Optics, Cambridge University Press, Cambridge, U.K. (1990)

[69] M. Sheik-Bahae, D. J. Hagan and E. Van Stryland, Phys. Rev. Lett., **65**, 96 (1990)

the magnitude of the TPA coefficient. This model has been compared with the experimental data in Fig. 3.13.

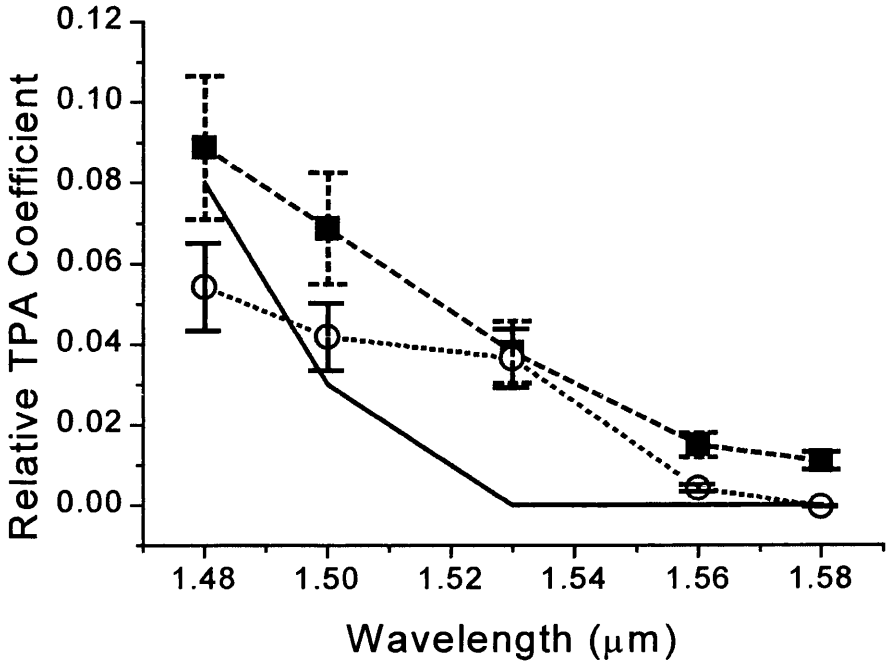


*Fig 3.13* Experimental values for $\alpha_2$ as a function of wavelength in a disorderd sample: TE, solid square. TM, empty circle. Scalar model, continuos line.

In principle, electrons do not have sufficient energy to make a transition to the conduction band by absorbing two photons for energies below half the band gap, which implies an absence of 2PA in such limit. However, an effective two-photon absorption can also arise from single photon absorption of the unphase-matched second-harmonic, which is present for a TE polarisation. Furthermore, because of defects in a real material, the equivalent of the Urbach tail occurs, as discussed in Sec. 1.3.1, and residual two-photon absorption is still present below half the band gap at 1.53 μm. In Fig. 3.13 we plot the relative value of the two photon absorption coefficient, $\Delta\alpha_2 = \dfrac{\alpha_2(\lambda)}{\alpha_2\left(E = \frac{2}{3}E_G\right)}$, as

function of the wavelength. Here $\alpha_2\left(E=\frac{2}{3}E_G\right)$ = 13 cm/GW, has been calculated using formula 3.4. We first note that the band gap shifts below 1.43 μm following intermixing resulted in the strong reduction of TPA in the disordered sample, which in fact was zero within the experimental error. The expected clear excitonic peak could not be observed in the sample "as grown" due to the large bandwidth of the pulses generated by the OPO (a few tens of nanometers) and also to the poor quality of the MOVPE wafer, as confirmed by the high values of linear loss. Nevertheless, the results show a degree of consistency with the values reported in Ref. 67, if we assume a Half Band edge of 1.53 μm. Furthermore, the general agreement between theory and experiment is satisfactory, even though the error bars are quite large due to a degree of uncertainty in linear loss within the waveguide and in the input coupling.

*3.4.2* **Three-photon Absorption.** Increasing the input intensity, the third order term becomes important and the differential equation which describes the change in the intensity I as a function of the propagation distance z through a sample in presence of one, Two- and Three-photon absorption must be written as:

$$\frac{dI}{dz}=-\alpha_0 I-\alpha_2 I^2-\alpha_3 I^3 \qquad 3.5$$

In order to measure accurately and unambiguously the 3PA coefficients (expressed in $cm^3/W^2$), the operating wavelength should be longer than the half band gap, where the TPA coefficient is effectively zero. In that case the TPA term can be neglected, and equation 3.4 is written in terms of an inverse transmission as:

$$\frac{1}{T^2}=\left(\frac{I_{in}}{I_{out}}\right)^2=\frac{1}{(1-R)^4\eta^2 e^{(-2\alpha_0 L)}}+\alpha_3\frac{\left(1-e^{(-2\alpha_0 L)}\right)}{\alpha_0(1-R)^2 e^{(-2\alpha_0 L)}}I_{in}^2 \qquad 3.6$$

From equation 3.6, it is shown that plotting the inverse transmission squared as a function of input intensity squared should lead to a straight line whose slope is proportional to $\alpha_3$ (the Three photon absorption coefficient).

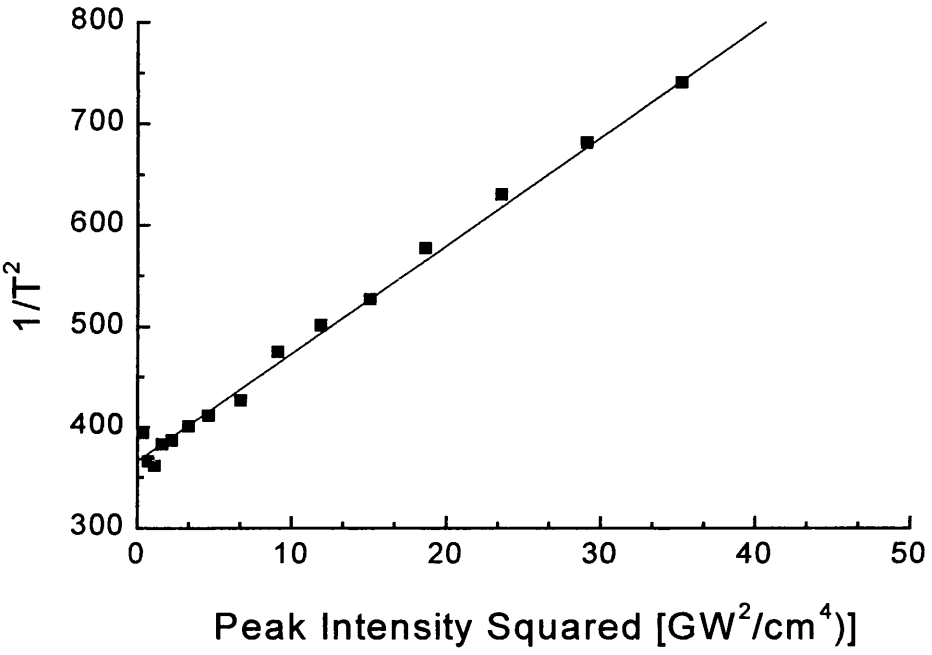


*Fig. 3.14* Plot of the inverse transmission squared as a function of the input intensity squared.

Typical results are shown in Fig. 3.14. There are a number of additional complications when short pulses are used to measure the 2PA and 3PA coefficients in waveguides. The non-linear absorption varies across the temporal envelope of the pulse. When detectors are slow compared to the pulse widths which are used, the scaling between pulse energy transmission and peak incident intensity depends on the pulse width and profile.

Similarly, to express the peak intensity within the waveguide, an average value of the transverse spatial distribution is determined in terms of an effective area for the non-linear interaction.

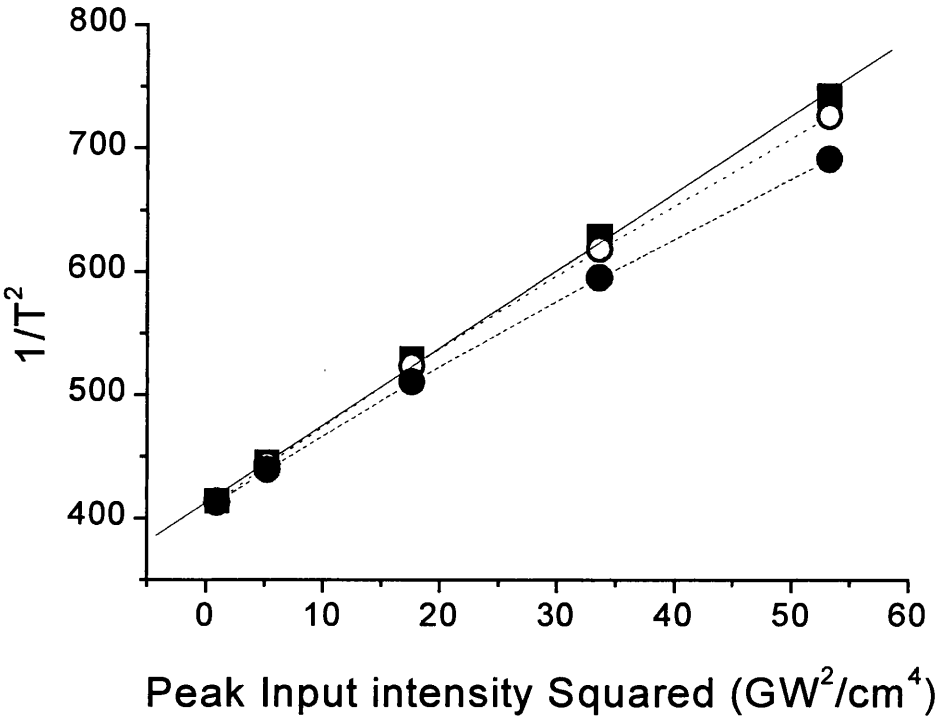


*Fig. 3.15* Effect of Three photon absorption, dispersion and self phase modulation on the transmission of a pulse with a sech-like shape in AlGaAs at the half band gap. Typical values of the inverse transmission as a function of the input power are shown in a CW regime (empty squares), and for pulses 100 fs and 200 fs long (solid and empty circles, respectively).

However, these two effects are well-known and were included in the calculation. The effect of Group Velocity Dispersion (GVD)(see Fig. 3.15) was also included. The effective area $A_{eff}^{(3)}$ and $A_{eff}^{(5)}$ were practically constant in the considered range and were, respectively, 8 and 6 $\mu m^2$.

Due to the presence of the single photon absorption of the unphase-matched second-harmonic and of defects in the material, Two and Three photon absorption can coexist. Fortunately, as the different contributes are energy-dependent, they can also be easily separated. At low intensities, the main

absorption process is linear absorption, whilst, as intensity is increased, 2PA and 3PA become the dominant loss mechanism. The values of energy characterising these regimes at a wavelength of 1.55 μm have been estimated from Ref. 11. In particular, $E_{\alpha_2}$ = 5 GW/cm$^2$ suggests an upper limit for the range of energies in which the fit of inverse transmission in function of input intensity is linear. Once the TPA contribution was known, it could be subtracted and the Three-photon absorption coefficient determined by plotting the inverse transmission squared as a function of the input intensity squared.

In Tab. 3.1 we report the intensity values which define the different regimes for AlGaAs near the Half Band Gap (the wavelength was 1.54 μm, as based on the recent experimental data reported in Ref. 11).

| **SPA regime** | **SPA+TPA regime** | **MPA regime** |
|---|---|---|
| $I << 0.5\ GW/cm^2$ | $0.5\ GW/cm^2 < I < 5\ GW/cm^2$ | $I > 5\ GW/cm^2$ |

***Tab 3.1*** The different linear and non-linear loss regimes.

The resulting 3PA coefficients as a function of wavelength are plotted in Fig. 3.16. In the same graph we also plotted the dispersion of the 3PA coefficient calculated using a parabolic band scaling law[70], which expresses the dispersion of the Three photon absorption coefficient as:

$$\alpha_3 = \frac{3^{10}\sqrt{2}}{8}\pi^2\left(\frac{e^2}{\hbar c}\right)\frac{\hbar^2 P^3}{n_0^3 E_g^7}\frac{\left(3\frac{\hbar\omega}{E_g}-1\right)^{\frac{1}{2}}}{\left(3\frac{\hbar\omega}{E_g}\right)^9} = D\frac{\left(3\frac{\hbar\omega}{E_g}-1\right)^{\frac{1}{2}}}{\left(3\frac{\hbar\omega}{E_g}\right)^9} \qquad 3.7$$

[70] B. S. Wherrett, J. Opt. Soc. Am. B, **1**, 67 (1984)

Here $P$ is the Kane parameter, related to the Kane energy[70]. The data plotted were normalised to the value of the Three photon absorption calculated for $Al_{0.18}Ga_{0.82}As$ at 2.15 μm, which is around 0.3 $cm^3/GW^2$ (from formula 3.8). Again, $D$ must be interpreted as a magnitude indicator rather than an exact value. The relative coefficient was defined as:

$$\Delta\alpha_3 = \frac{\alpha_3}{\alpha_3^{Al0.18Ga0.82As}(2.15\mu m)} \qquad 3.8$$

From the graph we can infer that the shift in the bandgap following intermixing is not large enough to produce significant changes in the 3PA coefficient, in agreement with the simple model described above. This is not surprising as the region investigated sits on the tail of the 3PA absorption spectrum.

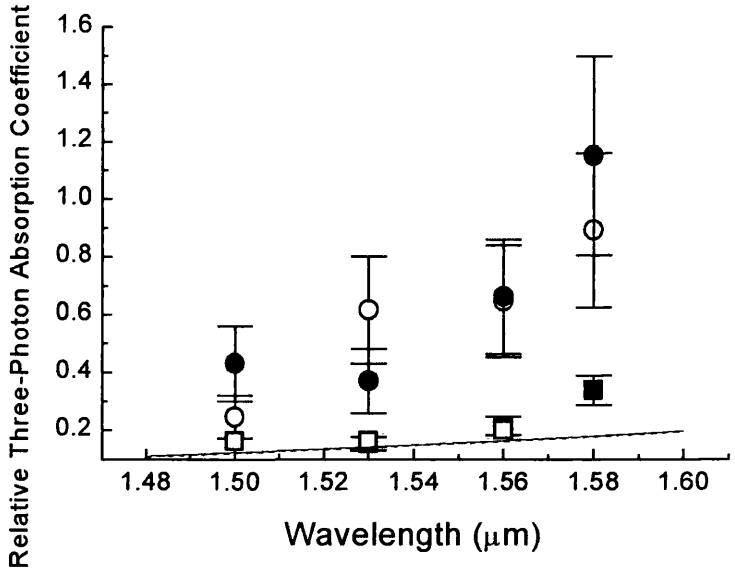


***Fig 3.16*** Experimental values for $\alpha_3$ as a function of wavelength. The data (disordered, TE, solid circle; disordered, TM, solid square; undisordered, TE, empty circle, undisordered, TM, empty square) are compared with the calculated dispersion of $\alpha_3$. The model predicts a scarce influence of intermixing on the value of 3PA, represented by a continuum line.

[69] M. Sheik-Bahae, D. J. Hagan and E. Van Stryland, Phys. Rev. Lett., **65**, 96 (1990)

*3.4.3* **Non-linear Refractive Index and Ratio XPM/SPM.** To determinate the value of $n_2$ we measured the spectral broadening due to Self Phase Modulation (SPM) generated by a sech-shaped pulse. In previous works[20] the experimental data were fitted using the following equation describing the evolution of the pulse:

$$\frac{dE}{dx} = -\frac{\alpha_0}{2} - \frac{\alpha_2}{2}|E|^2 E + ik_0 n_2 |E|^2 E \qquad 3.9$$

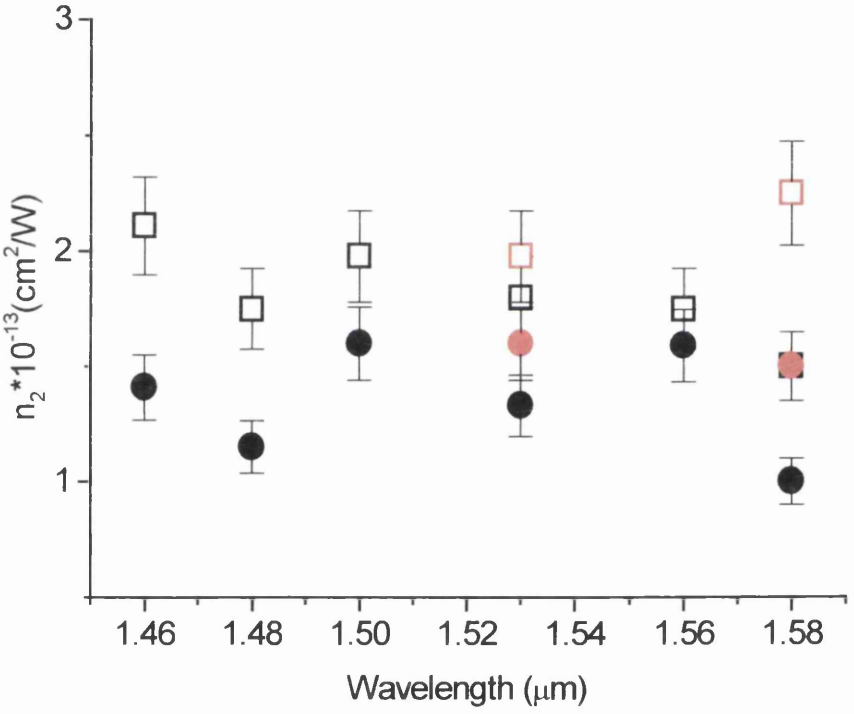


***Fig 3.17*** The measured dispersion of $n_2$. Disordered, TE, black empty squares. Disordered, TM, black solid circles. Undisordered, TE, red empty squares. Undisordered, TM, red solid circles.

Here $E$ is the electric field, and $\alpha_0$ and $\alpha_2$ are the linear and two-photon absorption, respectively.

[20] A. Villeneuve, J. U. Kang, J. S. Aitchison G. I. Stegeman, Appl. Phys. Lett., **67**, 760 (1995)

At lower intensities, (where $\Phi_{nl} < \pi/2$) the influence of Two-photon absorption is negligible, and SPM simply causes the broadening of the spectrum, which is fitted by the expression[14]:

$$\frac{(\Delta\omega)_{rms}}{(\Delta\omega)_0} = \left(1 + \frac{4}{3\sqrt{3}}\Phi^2_{max}\right)^{1/2} \qquad 3.10$$

Where $(\Delta\omega)_o$ and $(\Delta\omega)_{rms}$ are the initial and final rms spectral widths respectively. The values of $\Phi_{max}$ determined using the expression above, can be substituted in eq. 1.6 to calculate $n_2$.

We performed the measurement exciting both the fundamental TE and TM modes. To avoid the need of correcting for different coupling efficiencies, the output rather than the input powers were recorded and corrected for the linear losses. However, in the sample "as grown" high Two photon absorption above the half band gap and a large bandwidth resulted in a distorted spectrum, difficult to interpret. The values obtained for $n_2$ in function of the wavelength for the disordered sample are plotted in Fig. 3.17. The non-linear refractive index values for the undisordered samples, measured at 1.53 μm and 1.58 μm, respectively were also added to the same graph.

At low frequencies the shift in $n_2$ is dominated by the $E_g^{-4}$ scaling, but close to the half band gap the contribution to the shift from the dispersion of $n_2$ would have been of a similar magnitude. Previously reported results[65] on a similar structure have shown that intermixing can cause a 50% - 60% decrease in the value of $n_2$ just below the half band gap.

Using a similar technique the cross-phase modulation generated by a strong pump on a weak probe was recorded in the intermixed samples, to determinate the ratios XPM (TE pump)/ SPM ( TE ) and XPM (TM pump)/ SPM ( TM ).

---

[14] G. P. Agrawal, *"Nonlinear Fiber Optics"*, Academic Press, New York, USA (1995)

[64] C. J. Hamilton, J. H. Marsh, D. C. Hutchings, J. S. Aitchison, G. T. Kennedy, W. Sibbett, Appl. Phys. Lett., **68**, 3078 (1996)

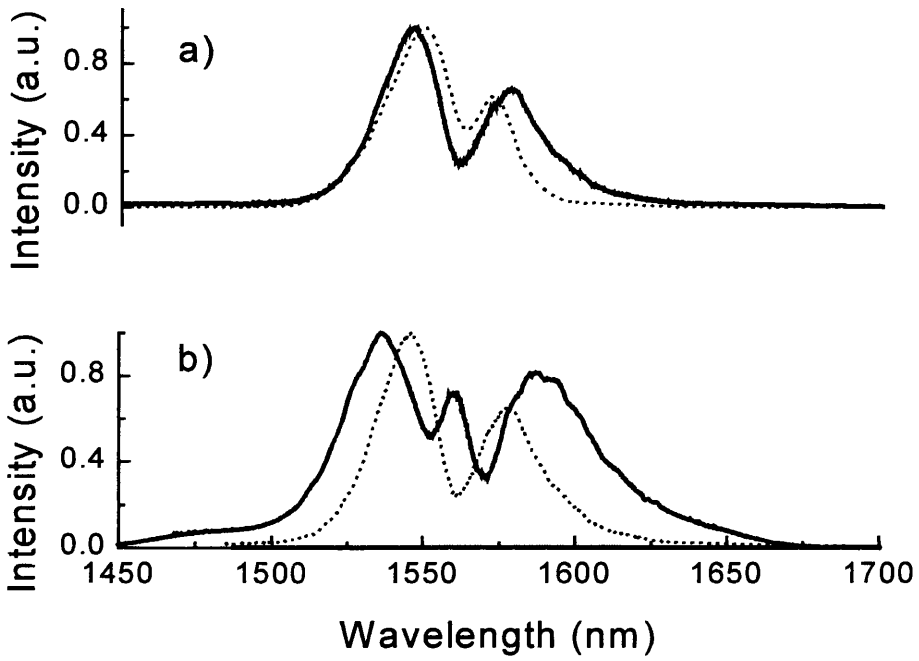


*Fig 3.18* a) SPM (continuum line) and XPM (dotted line) for a TM pump polarisation. b) SPM (continuum line) and XPM (dotted line) for a TE pump polarisation.

The TE beam generated by the OPO was rotated with an half wave plate to achieve the desired pump-probe configuration. Care was taken to assure that more than 90% of the total power was carried by the pump, thus the SPM of the probe was negligible.[11] From the theory follows that, in first approximation, A, the ratio between cross- and self-phase modulation can be experimentally measured by equalising the spectral broadening of the pump and the probe, individually selected using a polariser at the output of the waveguide, and recording the ratio between the powers transmitted.

[11] J. S. Aitchison, D. C. Hutchings, J. U. Kang, G. I. Stegeman, and A. Villeneuve, IEEE J. Quant. Electron., **33**, 341 (1997)

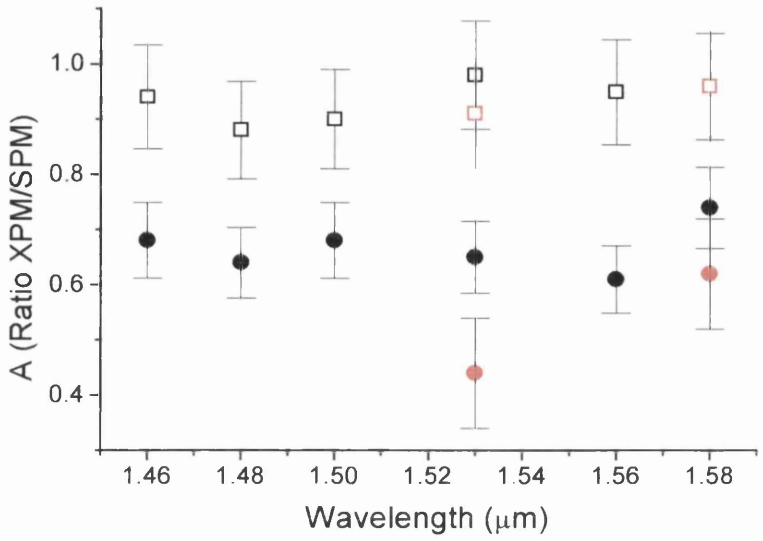


***Fig. 3.19*** The experimental dispersion of the ratio *XPM (TE pump)/ SPM ( TE )* (black solid circles) and of the ratio *XPM (TM pump)/ SPM ( TM )* (black empty squares) are shown for a disordered sample. We performed the same measures at 1.53 μm and at 1.58 μm in a sample "as grown" (red solid circles and red empty squares, respectively).

The conclusion that can be drawn from these measurements is that the ratio XPM (TE pump)/ SPM ( TE ) is rather wavelength insensitive in the tested range and has an average value of 0.94 ± 0.04 , while XPM (TM pump)/ SPM(TM) has an average value of 0.67 ± 0.01. However, if we observe that the average birefringence in the non-linear refractive index, defined as $\left\langle \frac{n_2(TM)}{n_2(TE)} \right\rangle$, is equal to 0.76 ± 0.1, we deduce that the ratio XPM (TM pump)/ SPM(TE) is equal to 0.9 ± 0.1, very near to an unity value. These numbers are different from the one obtained for isotropic materials presenting a Kleinmann symmetry (e. g. silica), while they resemble the values obtained in cubic semiconductors (bulk AlGaAs in particular). Such features make possible, for example, the generation of Manakov solitons in intermixed AlGaAs material[19]. The same measurements were repeated for the

[19] J. U. Kang, G. I. Stegeman, J. S. Aitchison and N. Akhmediev, Phys. Rev. Lett., **76,** 3699 (1996)

undisordered sample at two different wavelengths, 1.53 μm and 1.58 μm, hence below the half band gap. While the ratio ratio XPM (TM pump)/ SPM(TM) did not change significantly, we found that the values XPM (TE pump)/ SPM (TE) were reduced to 0.48 and 0.67, respectively. Hence, by correcting for the anisotropy of the Kerr coefficient, we could finally estimate the ratio XPM (TM pump)/ SPM (TE) in the two cases. The correspondent values obtained were 0.72 and 0.83.

## 3.5 Conclusions

In the experiment performed we have measured the dispersion of some important non-linear optical constants for an MQW AlGaAs waveguide at the half band gap, after intermixing with an IFVD technique. In particular, the non-linear absorption coefficient were compared with a sample "as grown".

Significant changes in the non-linear optical properties were introduced by intermixing. As compared to the original sample, the TPA was strongly reduced in the range investigated while Three photon absorption, plotted in Fig. 3.16, was scarcely affected. This fact is in good agreement with a two parabolic band scaling law which predicts higher scaling and detuning of the coefficient $\alpha_3$ around one third of the bandgap, but scarce sensitivity to small band gap changes in the range investigated. A strong anisotropy between the two main polarisations, TE and TM was recorded. In particular, higher values than expected were obtained for the TE polarisation. This can be due to the presence of Cross Multi photon absorption terms and to a residual non-linear exchange of energy between the two polarisations. The ratios XPM (TE pump)/ SPM (TE) and XPM (TM pump)/ SPM (TE), $A$, were measured to be circa unitary in the disordered sample (Fig. 3.19). It was previously reported[20] that the cross-phase modulation (XPM) for cross-polarised beams is equal to the self-phase modulation (SPM) in bulk AlGaAs semiconductor waveguides at photon energies lower than the half band gap. Therefore the intermixed sample

[20] A. Villeneuve, J. U. Kang, J. S. Aitchison G. I. Stegeman, Appl. Phys. Lett., **67**, 760 (1995)

resembles the bulk AlGaAs material concerning this particular aspect. Such homogeneity is not present in multiple quantum well (MQW) waveguide, where the ratio A of the cross-phase modulation coefficient to the self-phase modulation coefficient was measured to be approximately 1 for the pump polarised perpendicular to the well plane (TM) and between 0.5 and 0.8 for the pump beam parallel to the wells (TE)[20, 35]. Such numbers are in good agreement with the values we measured in the undisordered MOVPE sample (see Fig. 3.19).

[35] J. U. Kang, *"Spatial solitons in AlGaAs waveguides"*, Ph.D. Thesis, Orlando, USA (1996)

# Chapter 4

# *Summary*

The work described in this thesis has mainly focused on demonstrating the possibility of generating discrete optical solitons in non-linear AlGaAs waveguide arrays, in a non-resonant regime. Our main achievement was to verify how the dynamical properties of discrete solitons differ significantly from the continuous counterpart.

Briefly, due to a lack of momentum conservation in discrete systems, small displacements of the input beam from a symmetric position can be considerably amplified at the output facet, a promising property for all-optical switching and routing applications. The same considerations hold for discrete solitons that propagate at a small angle along to the array.

Optical engineers continuously argue about the feasibility of a soliton-based all optical network. However, we have to recognise that the recent progresses in this field have been somehow surprising. In 1990 (less than 10 years ago), Stewart Aitchison observed the first spatial soliton in glass, at a wavelength of 800 nm, probably after a good deal of work and prayers devoted to the dye laser source available at the time. Today, good materials and good laser systems allow generating spatial soliton in AlGaAs quite easily. In summer 1999, thanks to a new Optical Parametric Amplifier system, we were able to observe experimentally the first spatio-temporal soliton in a glass waveguide (or shall we call it "light bullet" instead?), something which looked extremely complicated only a couple of years ago.

Which such progress in the basic physics, I believe that the most important task for our community is now the full integration of the different components present in an optical network: if this goal will be also achieved, all-optical networks could become soon a reality.

# *List of References*


**1** K. C. Kao and G. A. Hockham, Proc. IEE, **113,** 1151 (1966)

**2** A. Werts, L' Onde Electrique, **46**, 967 (1966)

**3** L. F. Mollenauer, B. M. Nyman, M. J. Neubelt , G. Raybon , S. G. Evangelides, Elec. Lett., **27**, 178 (1991)

**4** A. U. Snyder and A. P. Sheppard, Optics Letters, **18**, 482 (1993)

**5** A. B. Aceves, C. De Angelis, S. Trillo, S. Wabnitz, **19**, 332 (1994)

**6** See, for example, J. M. Jacob, E. A. Golovchenko, A. N. Pilipetskii, G. M. Carter, C. R. Menyuk, IEEE Photonics Technology Letters, **9**, 130 (1997)

**7** J. P. Gordon, in XV International Conference on Quantum Electronics, Digest of Technical Papers, 98 (1987)

**8** Y. Kodama and S. Wabnitz, Optics Letters, **18**, 1311 (1993)

**9** P. N. Butcher and D. Cotter, *"The Elements of Non-linear Optics and Electronic Properties of Semiconductors"*, Cambridge Studies In Modern Optics, Cambridge, UK (1990)

**10** R. K. Chang and N. Bloembergen, Phys. Rev., **144**, 775 (1962)

**11** J. S Aitchison, D. C. Hutchings, J. U. Kang, G. I. Stegeman and A. Villeneuve, IEEE J. Quant.Electron., **33**, 341 (1997)

**12** D. C. Hutchings and B. S. Wherrett, Optical Materials, **3**, 53 (1994)

**13** M. Sheik Bahae, D. C. Hutchings, D. J. Hagan, E. W Van Stryland, IEEE J. Quant. Electron., **27**, 1296 (1991)

**14** For a detailed discussion see G. P. Agrawal "*Nonlinear Fiber Optics*" , Academic Press, New York, USA (1995)

**15** F. Urbach, Phys. Rev., **92**, 1324 (1953) and:

**16** H. Haug and S. W. Koch, *"Quantum Theory of the Optical and Electronic Properties of Semiconductors"*, World Scientific, Singapore (1990)

**17** J. U. Kang, A. Villeneuve, M. Sheik Bahae, G. I Stegeman, K. Al hemyari, J. S.Aitchison, C. N Ironside, Appl. Phys. Lett., **65**, 147 (1994)

**18** C. J. Hamilton, *"Novel Structure and fabrication Techniques for the Observation of Solitons in AlGaAs"*, Ph.D. Thesis, University of Glasgow, Glasgow, UK (1995)

**19** J. U. Kang, G. I. Stegeman, J. S. Aitchison and N. N. Akhmediev, Phys. Rev. Lett., **76**, 3699 (1996)

**20** A. Villeneuve, J. U. Kang, J. S. Aitchison and G. I. Stageman, Appl. Phys. Lett., **67**, 760 (1995)

**21** J. S. Aitchison, J. U. Kang, G. I. Stageman, App. Phys. Lett., **67**, 2456 (1995)

**22** J. S. Aitchison, K. Al-Hemyari, C. N. Ironside, R. S. Grant, and W. Sibbett, Electron. Lett., **28**, 1879 (1990)

**23** J. S .Aitchison, A. M. Weiner, Y. Silberberg, D. E. Leaird, M. K. Oliver, J. L. Jackel, D. E. Leaird, M. K. Oliver, E. M. Vogel and P. W. E. Smith, Opt. Lett., **15**, 471 (1990)

**24** R. W. Boyd, "*Non-linear Optics*", Academic Press, (1992)

**25** H. A. Haus and W. S. Wong, "Solitons in optical communications", Rev. of Mod. Phys., **68**, 423 (1996)

**26** D. N. Christodoulides and R. I. Joseph, Opt. Lett., **13**, 53 (1988)

**27** J. U. Kang, G. I. Stegeman, A. Villeneuve, J. S. Aitchison, J. Europ. Opt. Soc. A, **5**, 583 (1996)

**28** D. E. Edmundson, R.. H. Enns, Opt. Lett., **18**, 1609 (1993)

**29** P. M. Goorjian and Y. Silberberg, Opt. Soc. Am. B, **14**, 3253 (1997)

**30** P. Millar, J. S. Aitchison, J. U. Kang, G. I. Stegeman, G. T. Kennedy, W. Sibbett and A. Villeneuve, J. Opt. Soc. Am. B, **14**, 3224 (1998)

**31** S. Adachi, J. Appl. Phys., **58**, R1 (1985)

**32** H. P. Zappe, *"Introduction to semiconductor integrated optics"*, Artech House, London, UK (1995)

**33** See, for example, D. Yevick, Opt. and Quant. Elec., **26**, S185 (1994)

**34** Hadley, G. R. , Opt. Lett., **17**, 1426, (1992)

**35** J. U. Kang, "Spatial solitons in AlGaAs waveguides", *Ph.D. Thesis*, Orlando, USA (1996)

**36** J. S. Aitchison, Y. Silberberg, A. M. Weiner, D. E. Leaird, M. K. Oliver, J. L. Jackel, E. M. Vogel and P. W. E. Smith, J. Opt. Soc. Am. B, **8**, 1290 (1990)

**37** D. N. Christodoulides and R. I. Joseph, Opt. Lett., **13**, 794 (1988)

**38** A. B. Aceves, C. de Angelis, T. Peschel, R. Muschall, F. Lederer, S. Trillo, and S. Wabnitz, Phys. Rev. E, **53**, 1172 (1996)

**39** A. S. Davydov and N. I. Kislukha, Phys. Status Solidi, B **59**, 465 (1995)

**40** T. Holstein, Ann. Phys., **8**, 325 (1959)

**41** P. Marquie, J. M. Bilbault, and M. Remoissenet, Phys. Rev. , E **51**, 6127 (1995)

**42** P. Denardo, B. Galvin, A. Greenfield, A. Larranza, S. Putterman and W. Wright, Phys. Rev. Lett., **68**, 1730 (1992)

**43** S. Flach and C. R. Willis, Phys. Rep. **295**, 182 (1998)

**44** S. M. Jensen, IEEE J. Quant. Electron., **18**, 1580 (1982)

**45** See, for example, M.C. Gabriel and N. A. Whitaker, Jr., J. Light. Wave Tech., **7**, 1343 (1989)

**46** V. E. Zakharov and A. B. Shabat, Sov. Phys. JEPT, **34**, 62 (1972)

**47** A. C. Scott and L. Mac Neil, Phys. Lett. A, **98**, 87 (1983)

**48** P. Millar, " *Non-linear Propagation Effects in Periodic Microstructures*", Ph.D. Thesis, University of Glasgow, Glasgow (1997). The method described here uses an effective index approach.

**49** Y. Chen, A. W. Snyder and D. L. Mitchell, Electron. Lett., **26**, 77 (1990)

**50** A. A. Hardy, IEEE J. Quant. Elec., **34**, 1109 (1998)

**51** Y. S. Kivshar, D. K. Campbell, Phys. Rev. E **48**, 3077 (1993)

**52** J. U .Kang, C. J. Hamilton, J. S. Aitchison, G. I. Stegeman, Appl. Phys. Lett. **70**, 1363 (1997)

**53** Y. S. Kivshar, Opt. Lett., **18**, 7 (1993).

**54** W. Krolikowski and Y. S. Kivshar, J. Opt. Soc. Am. B, **13,** 876 (1996).

**55** S. Darmanyan, A. Kobyakov, E. Shmidt, and F. Lederer, Phys. Rew. E, **57**, 3520 (1998)

**56** U. Peschel, T. Pertsch, and F. Lederer , Opt. Lett.,.**23**, 1701 (1998)

**57** A. Komiyama, Opt. Comm., **151**, 25 (1998)

**58** D. G. Deppe and N. Holonyak, Jr., J. Appl. Phys, **64**, R93 (1988)

**59** B. S. Ooi, K. McIlvaney, M. W. Street, A. S. Helmy, S. G. Ayling, A. C. Bryce, J. H. Marsh, J. S. Roberts, IEEE J. Quant. Electron., **33**, 1784 (1997)

**60** P. Dumais, A. Villeneuve, A. S. Helmy, C. J. Hamilton, J. S. Aitchison, *"Soliton Emission from an AlGaAs Waveguide"*, Conference on Quantum Electronics and Laser Science (QELS), Technical Digest series, **12**, 166 (1997)

**61** C. Weisbuch and B. Winter *"Quantum Semiconductor Structures"*, Academic Press, New York, USA (1991)

**62** D. C. Hutchings and B. S. Wherret, Phys. Rev. B., **52**, 8150 (1995)

**63** M. W. Street, *"Quantum Well Intermixing for the Control of Second Order Non-linear Effects in GaAs/AlGaAs Asymmetric Quantum Well Waveguides"*, PhD Thesis, University of Glasgow, UK (1997)

**64** C. J. Hamilton, J. H. Marsh, D. C. Hutchings, J. S. Aitchison, G. T. Kennedy, W. Sibbett, Appl. Phys. Lett., **68**, 3078 (1996)

**65** C. J. Hamilton, S. E. Hicks, B. Vogele, J. H. Marsh, J. S. Aitchison, Elec. Lett., **16**, 1393 (1996)

**66** A. Obeidat and J. Khurgin, J. Opt. Soc. Am. B., **12**, 1222, (1995)

**67** J. U. Kang, J. Khurgin, C. C. Yang, H. H. Lin, G. I Stegeman, European Quantum Electronics Conference, Technical Digest, 241 (1998)

**68** D. C. Hutchings and B. S. Wherret, Phys. Rev. B, **49**, 2418 (1994)

**69** M. Sheik-Bahae, D. J. Hagan and E. Van Stryland, Phys. Rev. Lett., **65**, 96 (1990)

**70** B. S. Wherrett, J. Opt. Soc. Am. B, **1**, 67 (1984)